Thesis

Theoretical studies for proving the Universe with cosmological 21cm surveys: "from dark ages up to the present time"

Yoshitaka Takeuchi

Department of Physics,

Nagoya University

A dissertation submitted to Nagoya University in a partial fulfillment of requirements for the degree of Doctor of Philosophy in Science

March 25, 2014

Abstract

The spectrum line due to the hyperfine transition of neutral hydrogen atom is well known as the 21cm line whose wave length corresponds to the energy split of electron's two spin states. Although the time scale of this transition is too long to observe in the Earth's laboratory, the interstellar medium contains so much of neutral hydrogens that we can observe this transition by the radio telescope. Therefore the 21cm line is one of the most famous spectrum line in astronomy and powerful tool to study the Universe.

Recently, various radio survey projects which will probe the Universe from the dark ages to the epoch of reionization (EoR) via the 21cm line from neutral hydrogen in the intergalactic medium (IGM) are planning or on going. It is particularly worth noting that the observation via the 21cm line can explore the distribution of baryons directly. Therefore, it allows us to observe the dark ages, in which any shine object has not formed yet, through the distribution of neutral hydrogen and it might be the only way to explore the dark ages. The observations with the 21cm line from the IGM will provide us the new sight of the Universe we have not seen before and lead us to the era of more precision cosmology.

In this thesis, we present the applications of the 21cm survey for probing the cosmological model in more detail with future huge radio telescopes or interferometers. We estimate various effects to the signal by using both theoretical aspects and numerical results. Then we discuss the detectability and the accuracy of determination of cosmological parameters from future observations. We here focus on the two topics; probes for the missing baryon problem and the initial density fluctuations with non-vanishing isocurvature fluctuations.

The abundance of each component constituting the Universe is well determined from the observation of the cosmic microwave background (CMB). On the other hand, abundance of baryons can determined from the observation of the late time Universe through the shining objects such as galaxies and galaxy clusters. However the abundance of baryons is less than the prediction from CMB. This contrariety is called missing baryon problem and it is said that most of baryons probably remain in the IGM as cold/hot baryons. We here focus on the hyperfine transition of not only neutral hydrogen but also isotope helium-3 in the filamentary structures in the IGM, which may contain the high-density of them. Such signals are the direct probe of baryons in the IGM. We carefully estimate such signals and discuss the detectability of them by future radio surveys.

Next, we investigate the effects of the initial density fluctuations with non-vanishing isocurvature fluctuations to the structure formations through the 21cm line from the minihaloes (MHs)

at high-redshifts. Such a halo can not drive the star formation and it must constrain the high-density of neutral hydrogen without being ionized. Additionally, the observation of the 21cm line from the IGM has possibility for differentiating the fluctuations between CDM and baryon, which can not be realized by the observation of CMB. If isocurvature fluctuations between CDM and baryon can be distinguished, it opens the new window to the mechanism for the generation of matters and leads to the deeper understanding about the physics in the early Universe.

From these analyses, we found that the signals due to the hyperfine transition of both hydrogen and isotope helium-3 from the filamentary structure have enough amplitude to detect the signal by future radio surveys. In addition, the observed signal of the 21cm line from minihaloes is affected by non-vanishing isocurvature fluctuations and imprinted characteristic signature, which is caused by the incorporation processes from minihaloes into a larger halo.

Acknowledgement

First, I should express my sincere gratitude to my supervisor Takahiko Matsubara for comprehensive discussions and a great tutelage over the past five years. I wish to thank Naoshi Sugiyama and Saleem Zaroubi at Kapteyn Astronomical Institute, Netherlands, for providing me a wonderful chance to study abroad and for successive and stimulative discussions about radio astronomy. Similarly, I am so grateful for my collaborators; Sirichai Chongchitnan, Kiyotomo Ichiki, Kenji Kadota, Yoshiki Matsuoka, Tomo Takahashi, Masahide Yamaguchi, Shuichiro Yokoyama, and Joseph Silk, for a lot of valuable discussions and comments. Without encounters with you and your supports, I could not have studied among various field and completed this thesis.

I deeply thank for all of members in the Cosmology Group, Ω and TA laboratories in Nagoya University for a lot of laughs. Especially, I thank a lot for the members from At laboratory who shared a lot of time over my PhD life in Nagoya University and gave a grate hospitality. I also thank for office administrator, Hitomi Tanaka, for not only supporting our office works, but aldo being willing to offer consultation. I acknowledge the hospitality of the members of Astrophysics Group in University of Oxford and Kapteyn Astronomical Institute in University of Groningen.

Finally, I would like to pay special tribute to my family for constant supports over my life. The life studying cosmology for my major in PhD course led to incredible encounters with a lots of people and fruitful experiments. I convey to all of you I have met over my PhD life my appreciation again, thank you.

I have been supported by Grants-in-Aid for Japan Society for the Promotion of Science (JSPS) Fellows for three years, and it has provided fruitful research life. This work is also supported in part by the JSPS Strategic Young Researcher Overseas Visits Program for Accelerating Brain Circulation, and by Grants-in-Aid for Scientific Research on Priority Areas No. 467 “Probing the Dark Energy through an Extremely Wide and Deep Survey with Subaru Telescope”, and for Nagoya University Global COE Program “Quest for Fundamental Principles in the Universe: from Particles to the Solar System and the Cosmos”, from the Ministry of Education, Cluster, Sports, Science, and Technology (MEXT); Kobayashi-Maskawa Institute for the Origin of Particles and the Universe; Nagoya University for providing computing resources useful in conducting the research reported in this thesis.

Contents

Chapter 1

Introduction

1.1 History of Radio Astronomy

The birth of radio astronomy is around the end of the 19th century. In 1888, Heinrich R. Hertz discovered the radio wave from the discharge experiment. From 1894 to 1900, Oliver Lodge tried detecting the radio wave from the sun with the antenna of centimeter wave. In 1890, Arthur Kennely made the concept for detecting the radio wave from solar corona with the receiver of long-wave. However this concept was understood as impossible because it was found that such radio wave can not reach to the surface of the Earth, after he had discovered Earth's ionosphere. After that, the observation of radio wave was outside of astronomers behind the great success and rise of the large optical telescopes. Therefore, the discovery of the cosmic radio wave and the pioneering works for the radio astronomy were developed by radio engineers.

The first discovery of the astronomical radio source was consummated by Karl Jansky at Bell Telephone Laboratories in 1931, while identifying the atmospheric disturbance phenomena which might interfere with radio telephone service by using an array of dipoles and reflectors designed to receive short wave radio signals at a frequency of 20.5 MHz and at a wave length of 14.6 m. From the discovery of signals repeated on a cycle of around 24 hours, he figured out that it must be extraterrestrial radio wave. In 1933, he found that the signal comes from around the center of our galaxy, but the mechanism of such radio wave was still unknown. Fred L. Whipple discussed the prospects of getting the signal from the thermal radiation from the interstellar medium.

A communication engineer, Grote Reber, built the first parabolic dish radio telescope with 9 m in diameter in his back yard in 1940. He conducted the first sky survey at very high frequencies, 3300 MHz, 900 MHz and 160 MHz, and succeeded the detection of Junsky's cosmic radio wave at frequency of 162 MHz. In 1946, the radio interferometer was developed by Joseph L. Pawsey and Martin Ryle. The radio interferometer can overcome the weak point of radio telescopes whose resolution is far inferior to that of optical telescopes.

The discoveries of the radio wave from the sun were operated during the World War II. J.S. Hey picked up the interference from the direction of the sun and he confirmed that the large sunspot group crossed the front side even in the solar minimum (Hey, 1946). In addition to Hey's

work, G.C. Southworth tried observing the thermal radiation from the sun directly and detected it with the wave length of 3.2 cm in 1942. Then, Reber also detected the radio wave from the sun in 1943.

In 1964, Arno Allan Penzias and Robert Woodrow Wilson at Bell Laboratory found the existence of the homogeneous radio wave corresponding to $\sim$ 3 K by using the horn reflector antenna with very low noise level (Wilson and Penzias, 1967). This signal is a trace of the large expansion of the Universe after the Big Bong and well known as the Cosmic Microwave background (CMB) radiation. The development of the CMB satellite observations for these a few decades such as COBE (Smoot et al., 1992), WMAP (Spergel et al., 2003) and Planck (Planck Collaboration et al., 2013a) makes a remarkable improvement. COBE showed that the spectrum of CMB is complete black body with temperature of 2.725 ± 0.002 K and discovered the temperature anisotropies at the first time. WMAP measured the temperature anisotropies more precisely and determined the cosmological parameters accurately. It's the dawn of the precision cosmology and the Planck satellite provided the more accurate CMB map. The comparison of the observed last scattering surface images by these CMB missions are shown in Figure 1.1.

In 1960s, A. Hewish had observed the scintillation due to the solar window by the dipole antennas, which had very shot time resolution to measure the time-varying fluctuations. One of his students, J. Bell, incidentally found the signals repeating with around 1s interval in such data. It opened up the discovery of pulsar and the existence of neutron stars were also established, simultaneously. J.H. Taylor and R.A. Hulse found a pulsar whose pulse period irregularly varies, while observing the pulsars by Arecibo[1] telescope. It was not only a discovery of binary pulsar but also the indirect tribute for the gravitational wave.

Inspired by the River's work about cosmic radio waves in 1940, H.H. Oort has been considering to apply the cosmic radio waves for the fields of astronomy. Then, one of his students, H. van de Hulst, found that neutral hydrogen can emit the radio wave with wave length of 21cm due to the hyperfine transition in 1944. After the war, a competition for detecting the signal from neutral hydrogen started among some countries, though it was unknown how much neutral hydrogen is hosted in the interstellar medium and whether the signal can be detected. First detection of the 21cm line was reported by H.I. Ewen and E.M. Purcell in the USA. After that it is also reported by the groups in Netherlands and Austraia, and the results of these three groups are published simultaneously in 1951 (Pawsey, 1951; Muller and Oort, 1951; Ewen and Purcell, 1951). Neutral hydrogen is the major component in the interstellar medium and has strong transmissivity due to the long wave length. These advantages led to the understanding of the spiral structure in Milky Way System at the first time via the 21cm line.

1.2 The 21cm line of neutral hydrogen

The 21cm line is the spectrum line related to the hyperfine transition of neutral hydrogen atom. A proton and an electron in a hydrogen atom interact each other due to the magnetic

[1] http://www.naic.edu

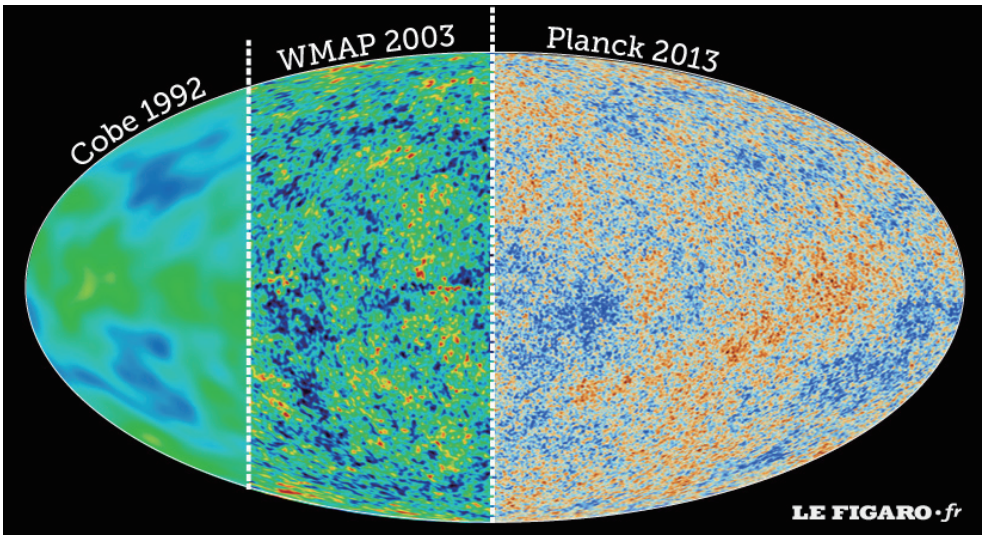

Figure 1.1: The comparison of the temperature maps in the last scttering surface observed by the CMB missions of recent year, COBE, WMAP and Planck, increasing the resolution from left to right. Credit: Le Figaro[2].

dipole moment and can have the hyperfine structure. The energy difference of the hyperfine transition corresponds to the frequency of $\nu \simeq 1420$ MHz and the wave length of $\lambda \sim 21$ cm. The transition probability of this hyperfine transition is so low, $A_{10} \sim 2.9 \times 10^{-15}$ s^{-1}, and known as the forbidden transition. The time scale of this transition is so long, i.e., $t \sim 10^7$ years, and it is hopeless to observe such transition in the laboratory.

However hydrogen constitutes a considerable fraction of elements in the Universe and it is enough to get the observable signal. Therefore the observation of hydrogen is the most fundamental and powerful tool to understand the distribution and movement of matters in the Universe. Under the favor of the high transmissivity, the emission from broadly distributing rarefied hydrogen gas with low temperature and so on, the spectrum line of the neutral hydrogen has an unshakable status as a way to observe the inter stellar medium in the radio astronomy.

1.3 From Dark ages up to the EoR

After recombination of a proton and an electron, the Universe is so cold and there are no sources to shine by themselves until the first structure is formed. Therefore, such epoch is called as the dark ages in the Universe and we have no way to observe with optical telescopes. However the observation of the neutral hydrogen gas via the 21cm line has possibility to explore even in the dark ages and it must be the only way to reveal the dark ages. Then, after the first objects are formed, the Universe starts to be heated by the UV/X-rays emitted from stars and galaxies and neutral hydrogens also begin to be ionized. Such an event is called as the reionization in the

[2]L'enfance de l'Univers vue par le satellite européen Planck, Le Figaro, 21 March 2013;
http://www.lefigaro.fr/sciences/2013/03/21/01008-20130321ARTFIG00444-l-enfance-de-l-univers-vue-par-le-satellite-planck.php

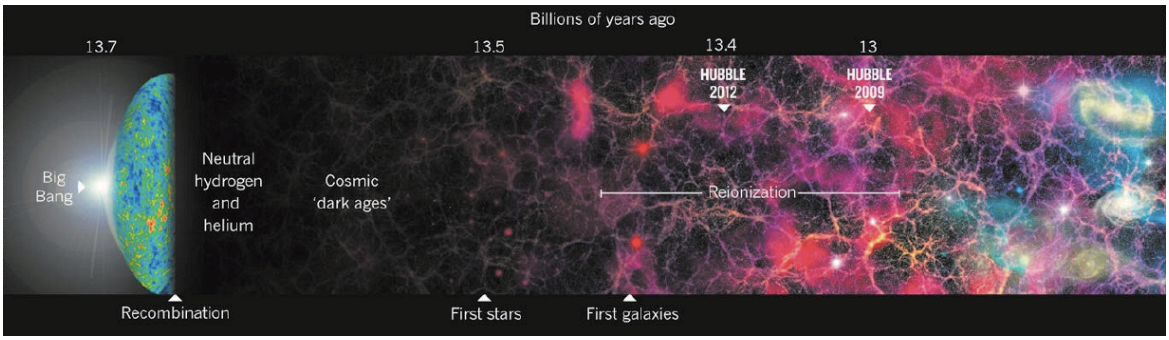

Figure 1.2: The schematic picture of the Universe after recombination to the end of the EoR. The epoch when the Universe had no stars to bright is called "dark ages". The slight density fluctuations are magnified through gravity and the clumpy regions gradually form the first stars and galaxies. Then, the UV light from such stars and galaxies ionizes the neutral gas and it moves into the epoch of "reionization". Credit: Nature[3].

Universe. From the various kind of observations such as the CMB observation and the survey of galaxies at high-redshifts, it is predicated that the epoch of reionization (EoR) may finish at redshift $z \sim 7$. After the EoR, the Universe is almost ionized and there are less neutral hydrogen in the intergalactic medium (IGM). Therefore, the 21cm line from IGM is less significant and strenuous efforts will be required to observe the IGM at low-redshifts via the 21cm line. We show the schematic picture of the Universe after recombination to the end of EoR in Figure 1.2.

Hence, the first generation radio surveys to observe the 21cm line from IGM are targeting the redshifts around EoR. Recently, the observations of the intergalactic medium are performed actively by various long-baseline radio interferometry surveys such as the Murchion Widefield Array (MWA[4]), the Low-Frequency Array (LOFAR[5]) (van Haarlem et al., 2013b), the Precision Array for Probing the Epoch of Reionization (PAPER[6]) and the Giant Metrewave Radio Telescope (GMRT[7]). Alternatively various surveys have planed and they are under the construction; e.g., MeerKAT[8], Australian Square Kilometre Array Pathfinder (ASKAP[9]) and Five-hundred-meter Aperture Spherical Telescope (FAST) (Nan et al., 2011). One of the goals for these generation radio surveys is to reveal the epoch of reionization (EoR) via the 21cm line of neutral hydrogen in the IGM.

In the left panel of Figure 1.3, we show the LOFAR central stations. Thousands of small antennas are placed in the LOFAR central station, and about eighteen smaller antenna fields spread over the North of the Netherlands. Furthermore, several international stations are constructed or planned around European countries, c.f., the right panel of Figure 1.3.

[3]Galaxy formation: Cosmic dawn, Nature, 29 May 2013;
http://www.nature.com/news/galaxy-formation-cosmic-dawn-1.13076

[4]http://www.mwatelescope.org
[5]http://www.lofar.org
[6]http://eor.berkeley.edu
[7]http://gmrt.ncra.tifr.res.in
[8]http://www.ska.ac.za/meerkat/index.php
[9]http://www.atnf.csiro.au/projects/askap/index.html

Figure 1.3: The overhead view of the antenna configuration of the LOFAR mission. (Left) The LOFAR central stations on a specially engineered field. (Right) Locations of the International LOFAR Telescope (ILT). Credits: Aerophoto Eelde[10] and ASTRON[11].

The targets of the next generation radio surveys are the observation of the dark ages and the understanding of the first structure in the Universe, and the Square Kilometre Array (SKA[12]) will achieves such demands. In addition, a more ambitious survey such as the Fast Fourier Transform Telescope (FFTT) is suggested by Tegmark and Zaldarriaga (2009), which is specialized for the probe of cosmological aspects.

The observation of the 21cm line of neutral hydrogen in the IGM has just started but there are still a lot of uncertainties on the theoretical side. To fully utilize the vast amounts of information from the observation, we now have to promote the understanding the history of reionization more and consider the more applications for the probe of cosmological aspects. The observation via the 21cm line is one of the few ways to study the distribution of baryons directly but CDM and the only way to reveal the dark ages. We are just about opening the new window for the Universe we have never seen.

1.4 Current status for the EoR from observations

The EoR experiments using radio telescopes are already underway. The forefront of such experiments is LOFAR. Similar experiments have announced the upper limits on $\Delta^2_{21\mathrm{cm}}(k)$ the power spectrum of the 21cm line at EoR in a stream recently. For instance, GMRT has obtained the upper limit of $\Delta^2_{21\mathrm{cm}}(k) \leq (248\mathrm{mK})^2$ for $k = 0.5\,h/\mathrm{Mpc}$ at $z = 8.6$ (Paciga et al., 2013) and MWA has also obtained almost same constraint such as $\leq (300\mathrm{mK})^2$ for $k = 0.5\,h/\mathrm{Mpc}$ at $z = 9.5$ (Dillon et al., 2013). The tightest constraint has been put on by PAPER, which is $\leq (52\mathrm{mK})^2$ for $k = 0.11\,h/\mathrm{Mpc}$ at $z = 7.7$ (Parsons et al., 2013).

[10] http://www.aerophotoeelde.nl
[11] http://www.astron.nl
[12] http://www.skatelescope.org

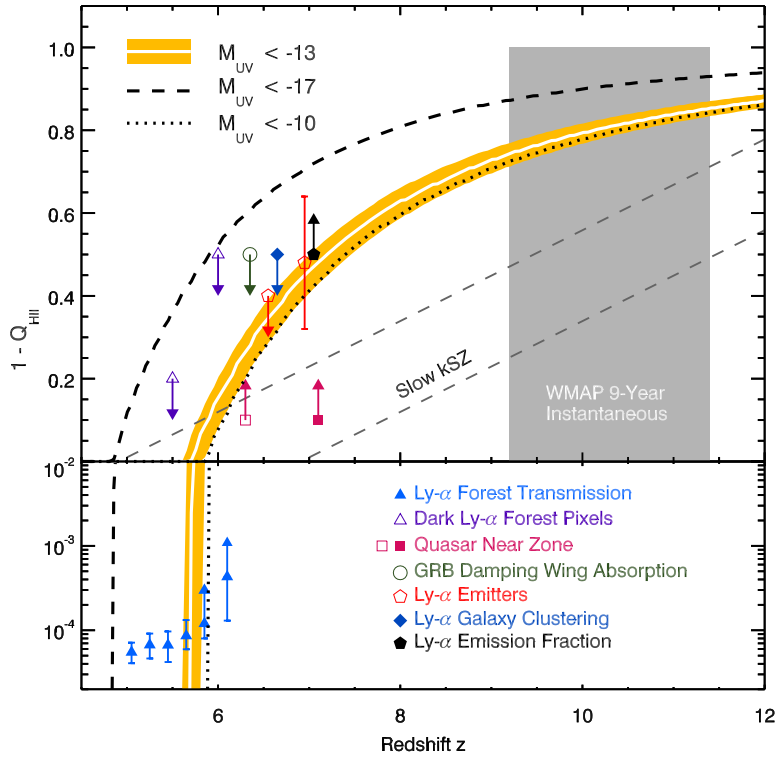

Figure 1.4: The reionization history obtained from the UDF12 survey and constraints on the neutral fraction $1 - Q_{\rm HII}$ claimed by the other observations; this figure is taken from Robertson et al. (2013). The different curves represent the models that take into account for the faint galaxies with $M_{\rm UV} < -13$ (white/solid) with 68% credibility (orange), $M_{\rm UV} < -17$ (dashed) and $M_{\rm UV} < -10$ (dotted).

On the other hand, the constraints on the EoR have been obtained from the other kind of observations in roundabout ways. For instance, observations of the Gunn-Peterson test (Gunn and Peterson, 1965) trough in quasar spectra indicate that intergalactic gas has become almost fully reionized by redshift $z \sim 5$ (e.g., (Djorgovski et al., 2001; Fan et al., 2006)).

From the electron scattering optical depth inferred from CMB observations, the reionization would have to occur as early as redshift $z \simeq 10$ if the universe was instantaneously reionized (Hinshaw et al., 2013; Planck Collaboration et al., 2013a). On the other hand, the small-scale temperature measurements, such as the Atacama Cosmology Telescope (ACT) and the South Pole Telescope (SPT), have begun to constrain on the EoR from the contribution of patchy reionization to the kinetic Syunyaev-Zel'dovich (kSZ) effect (Dunkley et al., 2013; Zahn et al., 2012). For instance, the SPT data suggests an upper limit on the transition from neutral fraction 0.99 to 0.20 with redshift interval of $\Delta z < 4.4$.

Robertson et al. (2013) has provided new constraints on the role that galaxies play in cosmic reionization and the duration of the process from the 2012 Hubble Ultra Deep Field (UDF12) campaign results. Their constraints on the ionization fraction in the EoR from the UDF12 survey and the other observations are summarized in Figure 1.4. They urge that the population of star-

forming galaxies at redshifts $z \sim 7-9$ must likely extend in the luminosity below the UDF12 limits to absolute UV magnitudes of $M_{\rm UV} \sim -13$ or fainter to fully reionize the Universe by redshift $z \sim 6$.

What elucidated and indicated in this thesis

In this thesis, we study the cosmological observation of IGM by future radio surveys, whose signals are related to the hyperfine transition. The 21cm line due to the hyperfine transition of neutral hydrogen is the most known target for the observation of IGM and one of the main topics in this thesis. The observation of the 21cm line from IGM leads to the direct search of baryon components. What's more remarkable is that it can reveal the history of reionization of the Universe and open a new window for the dark ages. The observation of the 21cm line has a lot of possibility for the better understanding about our Universe and must provide us fruitful information.

Fascinated by above aspects, we apply the observation of the 21cm line for various cosmological aspects and investigate how well it can probe the Universe more accurately. Thereby, we put forward suggestions on the application of the 21cm line survey for the next generation radio survey missions such as SKA and FFTT.

Firstly, we estimate the signal from filamentary structures at low-redshifts to approach the missing baryon problem. At low-redshifts, the reionization of the Universe has almost completed and less neutral hydrogens may remain. Therefore, we focus on the other materials which can have hyperfine structure, such as singly-ionized isotope helium (^{3}He II), too. Thus, we calculate the signal related to the hyperfine transition of H I and ^{3}He II in the filamentary structures at low-redshifts and discuss the prospects for detecting these signals by on-going or future radio telescopes (Takeuchi et al., 2014).

Secondly, we calculate the signal from MHs at high-redshifts and investigate how much the non-vanishing isocurvature fluctuations affect the 21cm signal from MHs (Takeuchi and Chongchitnan, 2014). The very blue-tilted isocurvature fluctuations can generate the density fluctuations in small-scales and it affects the structure formation of MHs. In addition, we investigate how well the observation of the fluctuations in the 21cm line form MHs can constrain isocurvature fluctuations by using the Fisher matrix analysis. Such studies lead to the understanding about the initial density fluctuations and the physics in the early Universe.

Outline of this thesis

This thesis is organized as follows. In Chapter 2, we review the cosmological background. We drive the Friedmann equation and introduce cosmological parameters to describe the constitution and the geometry of the Universe. Then, We introduce the statistical quantities and briefly summarize the structure formation.

In Chapter 3, we briefly review the fundamental physics of the 21cm line and the evolution of spin temperature. Then, we drive the expected signal of the 21cm line from IGM. We here

obtain the observed brightness temperature and explain the evolution of ionization states and the gas temperature in the IGM.

Our main work is presented in Chapters 4 and 5. In Chapter 4, we estimate the signal due to the hyperfine transition for not only neutral hydrogen (H I) but also singly-ionized helium-3 (^{3}He II) in the filamentary structures at low-redshifts. The we discuss the prospects for detecting such signals by on-going radio survey or future radio telescopes.

In Chapter 5, we calculate the 21cm emission signal from MHs at high-redshifts and estimate the effect of isocurvature modes for the structure formation and the 21cm emission signal from MHs. Furthermore we investigate how well isocurvature modes can be constrained by the future observation of the fluctuations in the 21cm emission from MHs.

Finally, we state the conclusion and the future prospects in Chapter 6.

Chapter 2

Cosmological Background

We here review the basic cosmological background as a preparation step in this thesis. First we derive the Friedman equation and introduce cosmological parameters to describe the constitution and the geometry of the Universe. Then we give a description for the growth of density fluctuations and define the statistical values such as power spectrum ans two point correlation function. Finally, we briefly get onto the structure formation in the Universe and summarize the halo mass function and bias. More detailed treatment can be found in e.g., (Dodelson, 2003; Weinberg, 2008).

2.1 Friedman Universe

The basic cosmological model relies most heavily on "the cosmological principle", which leads to that our earth or our galaxy is not located in the special point and there is no particular point in the Universe. Alternatively, our Universe bristles with lots of rich structures such as stars, galaxies and clusters and it is observationally well known to be significantly inhomogeneous. However, observing in the larger scale than the typical size of large-scale structures ($\gtrsim 100$ h^{-1}Mpc), the distribution of matters is almost homogeneous.

Such a isotropic and homogeneous universe can be described with the Robertson-Walker (RW) metric;

$$ds^2 = g_{\mu\nu}dx^\mu dx^\nu = -c^2dt^2 + a^2(t)\left[\frac{dr^2}{1-Kr^2} + r^2(d\theta^2 + \sin^2\theta d\phi^2)\right], \tag{2.1}$$

where $g_{\mu\nu}$ is the metric tensor, $a(t)$ denotes the scale factor and K denotes the curvature. Then we define χ on the radial coordinate as

$$r \equiv S_K(\chi) = \begin{cases} \dfrac{1}{\sqrt{K}}\sin\sqrt{K}\chi & (K>0) \\ \chi & (K=0) \\ \dfrac{1}{\sqrt{-K}}\sinh\sqrt{-K}\chi & (K<0) \end{cases}, \tag{2.2}$$

and Eq. (2.1) can be rewritten as

$$ds^2 = -c^2dt^2 + a^2(t)\left[d\chi^2 + S_K^2(\chi)(d\theta^2 + \sin^2\theta d\phi^2)\right] . \tag{2.3}$$

The scale factor $a(t)$ represents the relative spacial size at each time and we here normalize it as $a_0 = 1$ at present time t_0. r is the comoving coordinates which are at rest in the coordinate system in the Universe, whereas $a(t)r$ is equivalent with the coordinate system which evolves with the expansion of the Universe or $a(t)$ and called proper coordinates.

We next evaluate the time evolution of the scale factor $a(t)$ which describes the expansion of the Universe. The Einstein equation relates the fabric of space-time to the energy;

$$G^\mu_\nu = \frac{8\pi G}{c^4}T^\mu_\nu \,, \tag{2.4}$$

where the Einstein tensor G^μ_ν in l.h.s describe the fabric of space-time and the energy momentum tensor T^μ_ν in r.h.s describe the distribution of the energy, momentum and pressure in the Universe. The Einstein tensor is composed of the Ricci tensor $R_{\mu\nu}$ and Ricci scalar R, which are from the Riemann tensor describing the curvature of space-time. Then the Einstein equation with cosmological constant Λ is given by

$$R_{\mu\nu} - \frac{1}{2}Rg_{\mu\nu} + \Lambda g_{\mu\nu} = \frac{8\pi G}{c^4}T^\mu_\nu \,, \tag{2.5}$$

and under the assumption of the spacial isotropy and homogeneity, the energy momentum tensor can be given in the form of the perfect fluid;

$$T_{\mu\nu} = (\rho + p)u_\mu u_\nu + pg_{\mu\nu}, \tag{2.6}$$

where u_μ is the four-velocity of fluid, ρ and p represent the mass density and pressure of fluid at the rest frame. Substituting above equation into Eq. (2.5), we get the following two independent equations;

$$\left(\frac{\dot{a}}{a}\right)^2 = \frac{8\pi G}{3c^2}\rho - \frac{c^2K}{a^2} + \frac{c^2\Lambda}{3} \,, \tag{2.7}$$

$$\frac{\ddot{a}}{a} + \frac{1}{2}\left[\left(\frac{\dot{a}}{a}\right)^2 + \frac{Kc^2}{a^2}\right] = -\frac{4\pi G}{c^2}p \,. \tag{2.8}$$

Eq. (2.7) represents the time components and show the time evolution of the scale factor for the given matter density. This equation is called *the Friedmann equation*. Alternatively, Eq. (2.8) represents the spacial components and it can be rewritten with Eq. (2.7) as

$$\dot{\rho} + 3\frac{\dot{a}}{a}\left(\rho + \frac{p}{c^2}\right) = 0 \,. \tag{2.9}$$

This equation describes the energy conservation low in the Universe. Although we have gotten the two independent equations such as Eqs. (2.7) and (2.9) which describe the time evolution

of the scale factor in the isotropic and homogeneous universe, the functions depending on the time are three, a, ρ and p. Therefore we need another independent equation and we focus on the equation of state $p = p(\rho)$ which relates the pressure to the density.

The equation of state depends on the behavior of matter which governs the Universe. The typical components constituting the Universe are categorized into following four components; (i) non-relativistic matter $p_{\rm m} \ll \rho_{\rm m}$, (ii) relativistic matter $p_{\rm r} = \rho_{\rm r}/3$, (iii) cosmological constant $p_\Lambda = -\rho_\Lambda$, (iv) dark energy $p_{\rm de} = w\rho_{\rm de}$. The equation of state of cosmological constant is expressed on that of dark energy as $w = -1$. Furthermore, these equation of states and the energy conservation low given in Eq. (2.9) lead to the following relation between the density and scale factor for each component; (i) $\rho_{\rm m} \propto a(t)^{-3}$, (ii) $\rho_{\rm r} \propto a(t)^{-4}$, (iii) $\rho_\Lambda = $ const., (iv) $\rho_{\rm de} \propto a(t)^{-3(1+w)}$. The density of the universe is represented as the summation of each component. If we assume a universe consisting of matter, radiation and dark energy, the density of the universe is given by

$$\begin{aligned} \rho(t) &= \rho_{\rm m} + \rho_{\rm r} + \rho_{\rm de}, \\ &= \rho_{\rm m0} a(t)^{-3} + \rho_{\rm r0} a(t)^{-4} + \rho_{\rm de0} a(t)^{-3(1+w)}\,, \end{aligned} \tag{2.10}$$

where the subscript of 0 represents the value at present time.

We here consider the flat and matter dominated universe without cosmological constant;

$$K = 0,\ \Lambda = 0,\ \text{and}\ \rho(t) \propto a(t)^{-3}. \tag{2.11}$$

This cosmological model is called *the Einstein-de Sitter model*. Under this cosmological model, Eq. (2.7) can be rewritten as

$$\dot{a}^2 = \frac{8\pi G}{3c^2}\frac{\rho_0}{a}\,. \tag{2.12}$$

From above equation, the critical energy density $\rho_{\rm cr0}$ and the critical mass density $\varrho_{\rm cr0}$ at present time are defined by

$$\varrho_{\rm cr0} = \frac{\rho_{\rm cr0}}{c^2} \equiv \frac{3H_0^2}{8\pi G} \approx 2.78 \times 10^{11}\, h^2\, M_\odot\, {\rm Mpc}^{-3}\,, \tag{2.13}$$

where H_0 is the Hubble constant, which describe the expansion rate of the Universe at present time, and given with scale factor by

$$H_0 = \left[\frac{1}{a}\frac{da}{dt}\right]_{t=t_0} = 100h\ {\rm km\,s^{-1}\,Mpc^{-1}}\,, \tag{2.14}$$

where h is the normalized dimension less Hubble constant.

We here define parameters as follows;

$$H(a) \equiv \frac{1}{a}\frac{da}{dt} \quad : \text{ Hubble parameter} \tag{2.15}$$

$$\Omega_i \equiv \frac{\rho_i}{\rho_{\rm cr0}} = \frac{8\pi G\rho_i}{3H_0^2c^2} \quad : \text{ density parameter of each component } (i = \mathrm{m, r, c, b}, \nu, ...) \tag{2.16}$$

$$\Omega_\Lambda \equiv \frac{c^2\Lambda}{3H_0^2} \quad : \text{ density parameter of cosmological constant} \tag{2.17}$$

$$\Omega_{\rm K} \equiv \frac{c^2K}{H_0^2} \quad : \text{ density parameter of curvature} \tag{2.18}$$

Then the Friedmann equation given in Eq. (2.7) can be rewritten with the parameters as

$$\Omega_{\rm m}(t) + \Omega_{\rm r}(t) + \Omega_\Lambda(t) = 1 + \Omega_{\rm K}(t)\,, \tag{2.19}$$

As a more realistic cosmological model, we consider a universe with non-relativistic and relativistic matters, curvature and cosmological constant. Rewriting Eq. (2.7) with present values as performed in Eq. (2.10) and adopting cosmological parameters defined in Eq. (2.18), we get the the following equation;

$$\begin{aligned} H^2(a) &= \frac{8\pi G}{3c^2}\frac{\rho_{\rm m0}}{a^3} + \frac{8\pi G}{3c^2}\frac{\rho_{\rm r0}}{a^3} + \frac{c^2\Lambda}{3} - \frac{c^2K}{a^2}, \\ &= H_0^2\left(\frac{\Omega_{\rm m0}}{a^3} + \frac{\Omega_{\rm r0}}{a^4} + \Omega_{\Lambda 0} - \frac{\Omega_{\rm K0}}{a^2}\right). \end{aligned} \tag{2.20}$$

Furthermore, in the matter dominated era in which non-relativistic matter governs the universe, this equation can transcribed as

$$H^2(a) = H_0^2\left(\frac{\Omega_{\rm m0}}{a^3} + \Omega_{\Lambda 0} - \frac{\Omega_{\rm K0}}{a^2}\right). \tag{2.21}$$

This cosmological model is called *the Friedmann-Lemaitre universe.*

2.2 Distance

Generally, the distance we usually use means the proper distance which is interval between two points measured at the same time. However we have to take account of the definition of distance in the cosmology. This is because that the observed light from distant objects was emitted in the past time and we can not define the same time at these two points. We therefore have to define the distance related to the observations and the typical ones are the angular diameter distance and the luminosity distance.

2.2.1 Comoving distance

The distance measured on the comoving coordinate is called the comoving distance. The distance light could have traveled in a time dt corresponds to a comoving distance $dx = c\,dt/a$ and given by

$$c\,\eta \equiv \int_0^t \frac{c\,dt'}{a(t')} \ . \tag{2.22}$$

It should be noted that regions separated by distance greater than $c\,\eta$ are not causally connected because no information could have propagated further than $c\,\eta$. η is monotonically increasing and can be used as a time variable. Hence, it is called *the conformal time*, whereas t is called *the cosmic time*. For instance, η can be expressed analytically as a function of a;

$$\eta \propto \begin{cases} a & \text{for radiation-dominated (RD)} \\ a^{1/2} & \text{for matter-dominated (MD)} \end{cases} \tag{2.23}$$

Then, the comoving distance out to an object at scale factor a is given by

$$\chi(a) = c\,(\eta_0 - \eta) = \int_{t(a)}^{t_0} \frac{c\,dt'}{a(t')} = \int_a^1 \frac{da'}{a'^2 H(a')} \ , \tag{2.24}$$

where η_0 and η represent the conformal time from $t = 0$ to the present time ($t = t_0$) and to the time at $t = t(a)$, respectively.

2.2.2 Angular diameter distance

Considering a object at the distance of $d_{\rm A}$, a observer see the object with angular separation of θ. If the proper diameter l of that object is known and the angular separation is enough small, the distance to that object can be defined as

$$d_{\rm A} = \frac{l}{\theta} \, . \tag{2.25}$$

This distance $d_{\rm A}$ is defined as the angular diameter distance. To accommodate the expanding universe, we first focus on the flat universe. Taking the diameter of a object with comoving coordinates as l/a and rewriting the distance to the object with the comoving distance given in Eq. (2.2), the angular separation is given by $\theta = (l/a)/\chi(a)$. Substituting this relation into Eq. (2.25), we get

$$d_{\rm A}^{\rm flat} = a\chi(a) = \frac{\chi(a)}{1+z} \, . \tag{2.26}$$

In addition, for the open or closed universe, the angular diameter distance is given by

$$d_{\rm A} = \frac{c}{H_0} \frac{a}{\sqrt{|\Omega_K|}} \times \begin{cases} \sinh[\sqrt{\Omega_K} H_0 \chi], & \Omega_K > 0 \\ \\ \sin[\sqrt{-\Omega_K} H_0 \chi], & \Omega_K < 0 \end{cases} \tag{2.27}$$

where both cases reduce to the result of flat universe in the limit of $\Omega_K = 0$.

2.2.3 Luminosity distance

As the other method, we consider the flax of the object whose absolute luminosity is known. For a object at the distance d_L with the luminosity L, the observed flax F is given in the isotropic and homogeneous universe without cosmic expansion by

$$F = \frac{L}{4\pi d_L^2} \,. \tag{2.28}$$

Therefore we can determine the distance by observing the flax of that object and the distance determined from above treatment is defined as the luminosity distance d_L.

Then, to accommodate the expanding universe, we first take the comoving coordinates whose origin is at the center of source object and define the luminosity passing the surface of spherical shell with the comoving radius of $S_K(\chi)$ as $L(\chi)$. The luminosity should be proportional to the the number and energy of photons passing the spherical surface per unit time. The number of photons passing the spherical surface is reduced by a factor of a because the physical distance is shorter in the past time. On the other hand, the energy of a photon is reduce by a factor of a due to the cosmic expansion. Compared to the luminosity at the past time, the luminosity is therefore reduced by a factor of a^2, i.e., $L = L(\chi)/a^2$. Then, the observed flax is given by

$$F = \frac{L(\chi)}{4\pi S_K^2(\chi)} = \frac{La^2}{4\pi S_K^2(\chi)} \,. \tag{2.29}$$

Substituting above equation into the definition of the luminosity distance given in Eq. (2.28), we obtain the luminosity distance in the expanding universe;

$$d_L = \frac{S_K(\chi)}{a} = (1+z) S_K(\chi) \,. \tag{2.30}$$

2.3 Linear perturbation

We have considered the completely isotropic and homogeneous universe so far, however any structures can not be formed without any inhomogeneity. Although the early universe is extremely homogeneous and only slight inhomogeneity is present, the slight inhomogeneity is amplified through the gravitational interaction.

We here consider the evolution of the inhomogeneity through the gravitational instability. The equations which govern the evolution of fluctuations are following three equations; the Euilar equation which is the equation of motion for the fluid relating the velocity field $\vec{v}$ and pressure field p, continuity equation which represents the conservation low, and the Poisson equation which describes the relation between the density field ρ and the gravitational potential ϕ generated by ρ.

We here define the deviations from the isotropic and homogeneous components for the density $\bar{\rho}(t)$ and the pressure $\bar{p}(t)$ as the density perturbation δ and the pressure perturbation δp in the

following forms;

$$\delta(\vec{r},t) = \frac{\rho(\vec{r},t) - \bar{\rho}(t)}{\bar{\rho}(t)}\,, \tag{2.31}$$

$$\delta p(\vec{r},t) = p(\vec{r},t) - \bar{p}(t)\,. \tag{2.32}$$

Then the evolution equation for the perturbations in the expanding universe can be written as follows;

$$\frac{\partial \vec{u}}{\partial t} + 2H\vec{u} + (\vec{u}\cdot\vec{\nabla})\vec{u} = -\frac{\vec{\nabla}(\delta p)}{a^2\bar{\rho}(1+\delta)} - \frac{1}{a^2}\vec{\nabla}\Phi \quad : \text{Euler equation}\,, \tag{2.33}$$

$$\frac{\partial \delta}{\partial t} + \vec{\nabla}\cdot[(1+\delta)\vec{u})] = 0 \quad : \text{Continuity equation}\,, \tag{2.34}$$

$$\nabla^2\Phi = 4\pi G a^2(\rho - \bar{\rho}\delta) \quad : \text{Poisson equation}\,, \tag{2.35}$$

where Φ corresponds to the Newton potential in the comoving coordinates and defined by

$$\Phi = \phi + \frac{1}{2}a\ddot{a}r^2\,. \tag{2.36}$$

These three equations describe the evolution of the density field and show the history of the structure formation in the expanding universe. However these equations are the non-linear system of partial differential equation and there is no analytic general solution. Therefore we require some assumptions to understand the behavior of solutions.

If the quantities describing the deviation from the background quantities such as δ, δp and $\vec{u}$ are sufficiently small, the terms with second- or higher-order of these quantities can be ignored. This process leads to the linear approximation and Eqs. (2.33) and (2.34) can be rewritten as

$$\frac{\partial \vec{u}}{\partial t} + 2H\vec{u} + \frac{\vec{\nabla}(\delta p)}{a^2\bar{\rho}} + \frac{1}{a^2}\vec{\nabla}\Phi = 0\,, \tag{2.37}$$

$$\frac{\partial \delta}{\partial t} + \vec{\nabla}\cdot\vec{u} = 0\,. \tag{2.38}$$

Eliminating the velocity term with above two equations and replacing Φ into δ with Eq. (2.35), we can obtain the differential equation for the density fluctuations δ as follow;

$$\frac{\partial^2\delta}{\partial t^2} + 2H\frac{\partial\delta}{\partial t} - 4\pi G\bar{\rho}\delta - \frac{\vec{\nabla}^2(\delta p)}{a^2\bar{\rho}} = 0\,. \tag{2.39}$$

Then, to obtain the relation between the pressure and the density perturbations, we assume the equation of state given by $p = p(\rho, S)$, where S represents the entropy of fluid in a uni mass. For the linear approximation, the pressure perturbation is given by

$$\delta p = \left(\frac{\partial p}{\partial \rho}\right)_S \bar{\rho}\delta + \left(\frac{\partial p}{\partial S}\right)_{\bar{\rho}} \delta S\,. \tag{2.40}$$

We here define the sound speed $c_{\rm s}$ as the rate of change when the entropy is kept constant,

$$c_{\rm s}^2 = \left(\frac{\partial p}{\partial \rho}\right)_S . \tag{2.41}$$

If the entropy perturbation can be ignored, the evolution equation for the density perturbation given in Eq. (2.39) can be rewritten as

$$\frac{\partial^2 \delta}{\partial t^2} + 2H\frac{\partial \delta}{\partial t} - 4\pi G\bar{\rho}\delta - \frac{c_{\rm s}^2 \vec{\nabla}^2 \delta}{a^2} = 0 . \tag{2.42}$$

We here consider the Fourier decomposition for the spacial components of perturbation. The Fourier transform and its inverse transform for the density perturbation is defined by

$$\delta_{\mathbf{k}}(\vec{k}, t) = \int d^3 r e^{-i\vec{k}\cdot\vec{r}} \delta(\vec{r}, t) , \tag{2.43}$$

$$\delta(\vec{r}, t) = \int \frac{d^3 k}{(2\pi)^3} r e^{i\vec{k}\cdot\vec{r}} \delta_{\mathbf{k}}(\vec{k}, t) , \tag{2.44}$$

and the equation for $\delta_{\mathbf{k}}(\vec{k}, t)$ is given by

$$\frac{\partial^2 \delta_{\mathbf{k}}}{\partial t^2} + 2H\frac{\partial \delta_{\mathbf{k}}}{\partial t} - \left(4\pi G\bar{\rho} + \frac{c_{\rm s}^2 k^2}{a^2}\delta_{\mathbf{k}}\right) = 0 . \tag{2.45}$$

Each Fourier mode is independent each other and it does not affect the other modes in the linear regime.

We then evaluate the behavior for the solution of Eq. (2.45). The first term denotes the acceleration of particles, the second term represents the viscous term due to the cosmic expansion and the third term corresponds to the force due to the potential. Therefore the sign of a coefficient in the third term, $4\pi G\bar{\rho} - c_{\rm s}^2 k^2/a^2$, governs the behavior of its solution. If the sign is negative, the density fluctuations δ decays by oscillating and can not grow. On the other hand, if the sign is positive, the density fluctuations can grow with feeling the friction due to the cosmic expansion.

We define the wave number which corresponds to that the coefficient is zero as $k_{\rm J}$, then it can be written as a distance;

$$\lambda_{\rm J} \equiv \frac{2\pi a}{k_{\rm J}} = c_{\rm s}\sqrt{\frac{\pi}{G\bar{\rho}}} . \tag{2.46}$$

This critical length $\lambda_{\rm J}$ is called the Jeans length, which gives indication whether the perturbation grows through the gravitational instability and collapses to a object.

We first consider the growth for the fluctuations in the sufficiently larger scale than the Jeans length or the fluctuations of non-relativistic matters. In both cases, the term pressure can be ignored, then the evolution equation for the density fluctuations in the wave number space can be given by

$$\frac{\partial^2 \delta_{\mathbf{k}}}{\partial t^2} + 2H\frac{\partial \delta_{\mathbf{k}}}{\partial t} - 4\pi G\bar{\rho}\delta = 0 . \tag{2.47}$$

The fluctuations of dark matter entering in the matter dominated era is equivalent to this case. A special solution for this equation is $\delta \propto H(a)$. The other solution can be obtained by putting the solution as $\delta \propto C(a)H(a)$ and substituting it into Eq. (2.47), then we solve the equation for $C(a)$. The independent two solutions are given by

$$D_+ \propto H(a)\int_0^a \frac{da'}{(a'H(a'))^3} \tag{2.48}$$

$$D_- \propto H(a) \tag{2.49}$$

These quantities describe the time evolution for the linear growth solution of density fluctuations in the matter dominated ear and D_+ and D_- correspond to the growing and decaying modes, respectively. The decaying mode is such solution getting smaller rapidly and it can be ignored after a long time. We therefore take into account only the growing mode hereafter. We here define the normalization of D_+ as D_+ is equivalent to a in the matter dominated era. In that time, the Hubble parameter can be given by $H(a) = H_0\Omega_{\rm m0}^{1/2}a^{-3/2}$ and D_+ is defined as

$$D_+(a) = \frac{5\Omega_{\rm m0}}{2}\frac{H(a)}{H_0}\int_0^a \frac{da'}{(a'H(a')/H_0)^3}\,. \tag{2.50}$$

$D_+(a)$ is called the linear growth factor and we hereafter denotes it as $D(a)$. Instead of $D(a)$, the quantity defined by $ag(a) = D(a)$ is also used and $g(a)$ is called the linear growth function.

2.4 Power spectrum and Correlation function

We here consider the statistical values for the density fluctuations. It is assumed that the density fluctuations in the Universe are generated through the stochastic processes, therefore the behavior of fluctuations in a certain point can not be expected theoretically. What the theory can predict is only the statistical values, which represent the global nature of density fluctuations.

Generally, the density fluctuations in the early universe are described by the Gaussian random field, then the statistical property leads to the two points correlation function for the density fluctuations by following form;

$$\xi(\mathbf{x}-\mathbf{y}) \equiv \langle \delta(\mathbf{x})\delta^*(\mathbf{y})\rangle\,. \tag{2.51}$$

We next consider the Fourier transform of the density perturbation;

$$\delta(\mathbf{x}) = \int \frac{d^3k}{(2\pi)^3}\delta_{\mathbf{k}}(\mathbf{k})\; e^{-i\mathbf{k}\cdot\mathbf{x}}. \tag{2.52}$$

The two points correlation function in the Fourier space is defined by

$$\langle \delta_{\mathbf{k}}(\mathbf{k})\delta^*_{\mathbf{k}}(\mathbf{k}')\rangle = \int d^3x e^{-i\mathbf{k}\cdot\mathbf{x}}\int d^3x' e^{i\mathbf{k}'\cdot\mathbf{x}'}\langle \delta(\mathbf{x})\delta^*(\mathbf{x}')\rangle\,. \tag{2.53}$$

Then, rewriting as $\mathbf{x}' = \mathbf{x} + \mathbf{y}$, we get the following equation;

$$\begin{aligned}\langle \delta_{\mathbf{k}}(\mathbf{k}) \delta^*_{\mathbf{k}}(\mathbf{k}') \rangle &= \int d^3x e^{-i\mathbf{k}\cdot\mathbf{x}} \int d^3y e^{i\mathbf{k}'\cdot(\mathbf{x}+\mathbf{y})} \xi(|\mathbf{y}|), \\ &= (2\pi)^3 \delta_{\rm D}(\mathbf{k}-\mathbf{k}') \int d^3y \; e^{i\mathbf{k}\cdot\mathbf{y}} \xi(|\mathbf{y}|), \\ &= (2\pi)^3 \delta_{\rm D}(\mathbf{k}-\mathbf{k}') P(k) \,. \end{aligned} \tag{2.54}$$

In the last line, we defined $P(k)$ as follow;

$$P(k) \equiv \int d^3y \; e^{i\mathbf{k}\cdot\mathbf{x}} \xi(|\mathbf{x}|) \,. \tag{2.55}$$

$P(k)$ is called the power spectrum, which corresponds to the inverse Fourier transform of the correlation function. By assuming the isotropy, $P(k)$ does not depend on the direction of $\mathbf{k}$.

The shape of the initial power spectrum depends on the generation mechanism of density fluctuations. Although the inflation theory does not uniquely predict the properties of density fluctuations, it predicts the shape of the power spectrum to be the power low of wave number k;

$$P(k) = A k^{n_{\rm s}} \,, \tag{2.56}$$

where A is the amplitude of power spectrum and $n_{\rm s}$ is the spectrum index. Most of inflation model predicts the spectrum index to be close to $n_{\rm s} \sim 1$ and such a spectrum with $n_{\rm s} = 1$ is called the Harrison-Zel'dovich spectrum. The deviation from the Harrison-Zel'dovich spectrum contains the information of the slow-roll parameters and it leads to the investigation of inflation models.

As shown so far, the fluctuations in all scales grow following the linear growth factor $D(a)$ until the non-linear regime. However the shape of the power spectrum depends on whether the scale of fluctuations is larger or smaller than the horizon scale. In the larger scale than the horizon scale, the shape of the initial power spectrum is retained, whereas fluctuations in smaller scale are affected by various physical processes and the shape of power spectrum is changed. In the linear theory, the evolution equation for the density fluctuations is independent of wave number k. Therefore such effects can be considered as the independent effects for each wave number, the power spectrum at the time t can be defined as

$$P(k,t) = \frac{T^2(k,t) D^2(t)}{D^2(t_{\rm ini})} P_{\rm (ini)}(k) \,, \tag{2.57}$$

where $T(k,t)$ is the transfer function, which describes the modification of initial power spectrum for each wave number and governs the evolution of fluctuations due to various physical effects inside the horizon scale.

We next consider the amplitude for the power spectrum of density fluctuations, which corresponds to the normalization of the power spectrum and there are two kind of manners. One is

the way to determine from the temperature anisotropies of CMB. By observing fluctuations in the larger scale than the horizon scale in that time, we can measure the initial power spectrum directly.

Another way is to normalize it by using the amplitude of density fluctuations at present time. The density fluctuations averaged over a certain scale R is given by

$$\begin{aligned} \delta_M(\vec{r},t) &= \int \delta(\vec{r}',t) W_R(|\vec{r}-\vec{r}'|) d^3r, \\ &= \frac{1}{(2\pi)^3}\int \delta_k(\vec{k},t)\tilde{W}_R(k)\exp(-i\vec{k}\cdot\vec{r})d^3k\,, \end{aligned} \tag{2.58}$$

where δ_M represents density fluctuations at a mass scale of M, which is equivalent to the mass contained within the sphere with smoothing scale R, $M = \frac{4\pi}{3}\bar{\rho}R^3$. $W_R(r)$ and $\tilde{W}_R(k)$ represent the window functions in the real space and the Fourier space, respectively. We here adopt the top-hot window function given by

$$W_R(r) = \begin{cases} \dfrac{3}{4\pi R^3} & r < R, \\ 0 & r > R, \end{cases} \tag{2.59}$$

$$\tilde{W}_R(k) = \frac{3}{(kR)^3}\left[\sin(kR) - kR\cos(kR)\right]\,. \tag{2.60}$$

Then, the variance of density fluctuations averaged over mass scale M is given by

$$\sigma_M^2(M,t) \equiv \langle|\delta_M(\vec{r},t)|^2\rangle = \frac{1}{(2\pi)^3}\int P(k,t)\tilde{W}_R^2(k)d^3k\,. \tag{2.61}$$

For the normalization of the power spectrum, σ_8 is used, which is the variance within the sphere with radius of $R = 8h^{-1}$Mpc at present time. When the power spectrum is given by following form;

$$P(k) = Ak^{n_s}T^2(k)D^2(a), \tag{2.62}$$

σ_8^2 is evaluated by substituting above equation into Eq. (2.61) and taking the value at $R = 8h^{-1}$Mpc;

$$\sigma_8^2 = A\int \frac{d^3k}{(2\pi)^3}k^{n_s}T(k)^2D^2(a_0)|\tilde{W}_8(k)|^2\,. \tag{2.63}$$

By determining the value of σ_8 from observations, the amplitude of the initial power spectrum A can be also determined.

2.5 Structure Formation and Dark Matter Halo

We here briefly summarize the theories characterizing the structure formation of large-scale structures in the Universe. We first derive the halo mass function following the Press-Schechter prescription. Alternatively, we review the halo bias which relates the distribution of matters to that of haloes.

2.5.1 Halo Mass Function

The objects can be formed more easily in the high density region and the number of objects also increases. The objects such as galaxies and clusters are encompassed with spherical regions called halo. The halo model explains that the dark matter particles distribute in the spherical halo. Therefore the understanding of the statistical property of haloes is essential when we study that of large-scale structures in the Universe. The number density of objects in a universe is represented with the halo mass function, which describes how much haloes with certain mass exist in a universe.

The theory of the Press-Schechter (Press and Schechter, 1974) is widely used in the theory of the cosmological structure formation. This theory describe the model to estimate the abundance of objects formed in the certain epoch. The mass function $n(M, z)$ can be derived analytically as the comoving number density of haloes collapsed at redshift z with mass range of $M \sim M + dM$.

Press-Schechter Formalism

To describe the structure formation analytically, we first consider to extrapolate the linear solution for the growth rate of density fluctuations into the non-linear scale by the spherical collapse model. We consider a sphere with radius of R around the certain point. If the density fluctuations are small, the total mass M comprised in that sphere is expected with the average density of the Universe $\bar{\rho} = \Omega_{\rm m}\rho_{\rm crit}$ as $M = 4\pi R^3\bar{\rho}/3$. Then we can relate the radius to the mass, and the averaged density fluctuations within that sphere can be defined as the fluctuations for the mass scale of M, δ_M. If the fluctuations before the averaging process follow the Gaussian statistics, the averaged quantities also follow the Gaussian statistics. Therefore the probability density function can be given by

$$P(\delta_{\rm M})d\delta_{\rm M} = \frac{1}{\sqrt{2\pi\sigma_M^2}} \exp\left(-\frac{\delta_{\rm M}^2}{2\sigma_M^2}\right) , \tag{2.64}$$

where σ_M^2 is the variance of the averaged density fluctuations δ_M, which is given in Eq. (2.61) and the radius of the sphere R corresponds to the smoothing scale of the window function. In the Press-Schcheter's prescription, when the density fluctuations for the mass scale M, δ_M, which is estimated from the linear solution of the density fluctuations, exceed the critical value $\delta_{\rm c}$, the gravitational instability will be driven and the object with mass of M will be formed. This critical value $\delta_{\rm c}$ corresponds to the value of the linear density fluctuations at the point of collapse in the spherical collapse model and $\delta_{\rm c} \approx 1.686$ is often used. The fraction of regions where exceed the critical value, $\delta_M > \delta_{\rm c}$, can be given with mass scale M as a cumulative probability;

$$f_{\rm c}(M) = P(> \delta_{\rm c}, M) = \int_{\delta_{\rm c}}^{\infty} P(\delta_M)d\delta_M = \frac{1}{\sqrt{2\pi}} \int_{\delta_{\rm c}/\sigma_M}^{\infty} e^{-x^2/2}dx \, . \tag{2.65}$$

In other words, above equation means the fraction which the objects with larger mass than M are formed in a unit volume.

We next consider the correspondence between this cumulative probability and the mass function. The fraction which the objects with mass scale of $M \sim M + dM$ is formed in a unit volume is given with Eq. (2.64) as $|f_{\rm c}(M + dM) - f_{\rm c}(M)|$. On the other hand, the abundance of objects with mass scale of $M \sim M + dM$ is given with the mass function $n(M)$ as $n(M + dM) - n(M)$. Consequently, these two quantities can be related as follow;

$$|f_{\rm c}(M + dM) - f_{\rm c}(M)| = [n(M + dM) - n(M)]\frac{M}{\bar{\rho}} \,. \tag{2.66}$$

Furthermore, considering that $dn(M)dM$ represents the number density of haloes with mass scale of $M \sim M + dM$, the mass function is given with Eq. (2.64) by

$$\frac{dn(M)}{dM} = \frac{1}{\sqrt{2\pi}}\frac{\bar{\rho}}{M}\left|\frac{d}{dM}\left[\int_{\delta_{\rm c}/\sigma_M}^{\infty} dx e^{-x^2/2}\right]\right|, \tag{2.67}$$

$$= \frac{1}{\sqrt{2\pi}}\frac{\bar{\rho}}{M}\left|\frac{d\ln\sigma_M}{dM}\right|\frac{\delta_{\rm c}}{\sigma_M}\exp\left(-\frac{\delta_{\rm c}^2}{2\sigma_M^2}\right) . \tag{2.68}$$

However the discussions so far have a little bit improper. First, the process which the objects once collapsed incorporate into a larger object is not taken into account (cloud-ini-cloud problem)Secondly, the density fluctuations with negative value, whose density is less than the average value, are never incorporated into objects. If we assume that the structure formation becomes advanced sufficiently, taking the limit of $\sigma_M \to \infty$ ($M \to 0$) leads to $f_{\rm c}(0) = \frac{1}{2}$ from Eq. (2.64). $f_{\rm c}(0)$ represents the fraction which all mass is contained within objects, and the fact that this value results in $\frac{1}{2}$ means that only half mass in a universe contributes to the structure formation. In the Press-Shcechter's prescription, this problem is avoided just by multiplying a factor of 2 to double the mass which contributes to the structure formation. Taking account this fact and expressing the label of redshift z clearly, the Press-Shcechter's mass function can be given by

$$\frac{dn(M,z)}{dM} = \sqrt{\frac{2}{\pi}}\frac{\bar{\rho}}{M}\left|\frac{d\ln\sigma_M}{dM}\right|\frac{\delta_{\rm c}(z)}{\sigma_M}\exp\left(-\frac{\delta_{\rm c}^2(z)}{2\sigma_M^2}\right) , \tag{2.69}$$

where $\delta_{\rm c}(z)$ denotes the critical density at redshift z; $\delta_{\rm c}(z) = \delta_{\rm c}D(z=0)/D(z)$, and $D(z)$ represents the linear growth rate.

Other mass functions

The Press-Shcechter's formalism is broadly used to describe the theory of cosmological structure formations. However, the discrepancy between the Press-Shcechter's prediction and the result of numerical simulations is well known; the Press-Shcechter's prescription overestimates in small-mass scales, whereas underestimates in large-mass scales. We show some the other mass functions, which are based on the numerical simulation as follows.

We, first, express the halo mass function with following universal form;

$$n(M,z)dM = \frac{\bar{\rho}}{M}f_{\rm MF}(\nu)\frac{d\nu}{\nu} \,, \tag{2.70}$$

with $\nu \equiv \delta_{\rm c}(z)/\sigma_{\rm M}$. The different model of the mass function can be expressed in $f_{\rm MF}(\nu)$. For instance, the Press-Shcechter's mass function, which is based on the spherical collapse model, is given by

$$f_{\rm PS}(\nu) = 2\sqrt{\frac{\nu^2}{2\pi}}\exp(-\nu^2/2) \ . \tag{2.71}$$

Just as an example, the other models of mass function (Sheth and Tormen, 1999; Sheth et al., 2001), which are based on the non-spherical (elliptical) collapse model, are given by

- **Sheth & Tormen** (Sheth and Tormen, 1999)

$$f_{\rm ST}(\nu) = 2A\left(1+\frac{1}{(\nu^2)^p}\right)\sqrt{\frac{\nu^2}{2\pi}}\exp(-\nu^2/2) \ , \tag{2.72}$$

  with $A \simeq 0.3222,\ p \simeq 0.3$.

- **Sheth, Mo & Tormen** (Sheth et al., 2001)

$$f_{\rm SMT}(\nu) = 2A\left(1+\frac{1}{(q\nu^2)^p}\right)\sqrt{\frac{q\nu^2}{2\pi}}\exp(-q\nu^2/2) \ , \tag{2.73}$$

  with $A \simeq 0.3222,\ p \simeq 0.3\ q \simeq 0.707$.

- **Warren et. al.** (Warren et al., 2006)

$$f_{\rm Warren}(\nu) = A\left(b+\frac{1}{\sigma_M^a(\nu)}\right)\exp(-c/\sigma_M^2(\nu)) \ , \tag{2.74}$$

  with $A = 0.7234,\ a = 1.625,\ b = 0.2538,\ c = 1.1982$.

2.5.2 Halo Bias

What we can expect from theory precisely is the statistical properties of the density fluctuations and the distributions of the cold dark matter. However the dark matter can not be observed directly because it never give off a light. What we can observe is the shining objects such galaxies, but the distribution of galaxies does not reflect that of the matter faithfully. The difference between them is caused by different clustering properties of haloes and dark matters. Generally, the concept relating these two properties is called bias and the relation between the density fluctuations of haloes $\delta_{\rm h}$ and that or (dark) matters $\delta_{\rm m}$ is assumed following form;

$$\delta_{\rm h}(M,z) = b(M,z)\delta_{\rm m}(M,z) \, , \tag{2.75}$$

where $b(M,z)$ represents the bias, which determine the behavior of the density fluctuations of haloes.

Peak-Background Formalism

The theory giving the instinctive understanding about the halo clustering is the peak-background split (PBS) theory (Cole and Kaiser, 1989), and the bias in large scale where the density fluctu-

ations linearly grow can be treated by PBS. We first assume that the density fluctuations δ can be divided into two independent components such as the long wave modes $\delta_{\rm l}$ and the short wave modes, which correspond to the density fluctuations in the background and in the peak region haloes are formed, respectively;

$$\rho(\boldsymbol{x}) = \bar{\rho}(1+\delta) = \bar{\rho}(1+\delta_{\rm l}+\delta_{\rm s})\,. \tag{2.76}$$

It means that the density field is considered as the superposition of these two components. In the region where the background components is close to the peak, the object is easily formed and halo is significantly biased by the matters within that region. Therefore the effects of the density field of the background is explained as displacement of the critical density for the structure formation $\delta_{\rm c}$ and the density fluctuations have to reach the new critical value of $\delta_* = \delta_{\rm c} - \delta_{\rm l}$ to be collapsed.

We here consider the Taylor expansion of the mass function around $\delta_{\rm l} = 0$;

$$n(\delta) \simeq n(0) + \left.\frac{dn(\delta_{\rm l})}{d\delta_{\rm l}}\right|_{\delta_{\rm l}=0}\delta_{\rm l} + \frac{1}{2}\left.\frac{d^2n(\delta_{\rm l})}{d\delta_{\rm l}^2}\right|_{\delta_{\rm l}=0}\delta_{\rm l}^2 + \dots\,. \tag{2.77}$$

It corresponds to the behavior around the point where the critical value δ_* is not changed. On the other hand, the Lagrangian number density of haloes at position $\boldsymbol{x}$, $n(\boldsymbol{x})$ (the number density of haloes in a unit mass), is given with the fluctuations of the long wave mode $\delta_{\rm l}(\boldsymbol{x})$ as a function of the statistical value of the fluctuations of the short wave mode $P_{\rm s}(k_{\rm s})$. The averaged density of haloes drags the matter fluctuations in large-scales and it is given by

$$n(\boldsymbol{x}) = \bar{n}(1 + b_{\rm L}\delta_{\rm l})\ . \tag{2.78}$$

Comparing this equation with Eq. (2.77) by the first-order of $\delta_{\rm l}$, the Lagrangian bias is given by

$$b_{\rm L} = \bar{n}^{-1}\frac{\partial n}{\partial\delta_{\rm l}} = \frac{1}{\sigma_M f_{\rm MF}}\frac{df_{\rm MF}}{d\nu}\ . \tag{2.79}$$

Then, the Lagrangian bias corresponding to the Press-Shcecheter's mass function given by 2.69 is written by

$$b_L(z,M) = \frac{\nu^2-1}{\delta_c(z)}\ . \tag{2.80}$$

The bias in the Eulerian space is required to take into account the clustering in the Eulerian space and given by $b_{\rm E} = 1 + b_{\rm L}$.

Just as an example, the halo bias models corresponding to the halo mass function given by Eqs. (2.72) - (2.74) are given as follows.

- **Sheth & Tormen** (Sheth and Tormen, 1999)

$$b_{\rm L}(z,M) = \frac{1}{\delta_c(z)}\left[\frac{q\delta_{\rm c^2}(z)}{\sigma_M^2} - 1\right] + \frac{2p}{\delta_{\rm c}(z)}\left[1 + \left(\frac{q\delta_{\rm c}^2(z)}{\sigma_M^2}\right)^p\right]^{-1}\ , \tag{2.81}$$

with $p \sim 0.3,\ q \sim 0.75$.

- **Sheth, Mo & Tormen** (Sheth et al., 2001)

$$b_{\rm L}(z,M) = \frac{1}{\sqrt{a}\delta_{\rm c}(z)}\left[\sqrt{a}(a\nu^2) + \sqrt{a}b(a^2\nu^2)^{1-c} - \frac{(a\nu^2)^c}{(a\nu^2)^c + b(1-c)(1-c/2)}\right] , \quad (2.82)$$

  with $a = 0.707,\ b = 0.5,\ c = 0.6.$

- **Warren et. al.** (Warren et al., 2006)

$$b_{\rm L}(z,M) = \frac{1}{\delta_c(z)}\left(\frac{2c}{\sigma_M^2} - \frac{a}{1+b\sigma_M^a}\right) , \quad (2.83)$$

  with $A = 0.7234,\ a = 1.625,\ b = 0.2538,\ c = 1.1982.$

Chapter 3

Fundamental physics of the 21cm line

We here briefly review the fundamental physics of the hyperfine transition, mainly on the 21cm line, and observed 21cm signal from IGM, c.f. (Furlanetto et al., 2006a; Mo et al., 2010; Pritchard and Loeb, 2012). We first introduce the hyperfine transition and its spectrum line. Then we explain the spin temperature, and derive the observed signal, i.e. brightness temperature. Finally, we solve the evolution of ionization states and the temperature of gas in IGM.

3.1 Hyperfine transition

The splitting of energy levels due to the nuclear spin of atomic nucleus is called as hyperfine structure, and which is categorized into the magnetic hyperfine structure and the quadrupole hyperfine structure. The magnetic hyperfine structure is cased by the coupling of the electron's magnetic moment to the magnetic field produced by the proton's magnetic moment. Such kind of hyperfine structure rarely appears for molecules because most of molecules have paired electron and the effect of spin is canceled out. Therefore the hyperfine structure caused by the electric quadrupole interaction instead of the magnetic dipole interaction become of particular importance for molecules.

Atomic hydrogen can have the magnetic hyperfine structure and the electron and the proton in the atomic hydrogen interact each other by their magnetic moments. The grand state The electron in the electronic grand state ($1s$) can have its spin state either parallel or antiparallel to the spin state of the proton. The magnetic dipole-dipole interaction between the electron and the proton results in the hyperfine splitting of each spin state. The antiparallel spin state with degeneracy $g_0 = 1$ has the lower energy, and the parallel spin state with degeneracy $g_1 = 2F + 1 = 3$ ($F = 1$) has higher energy. The energy difference between these two levels ΔE cause the emission of a photon with a wavelength $\lambda = 21.11$ cm, whose energy corresponds to $\Delta E = 5.87 \times 10^{-6}$ eV, and the electron spin flips, when the electron drops from the parallel spin state to antiparallel spin state.

The interaction energy between nuclear spin and electron spin is given by using angular

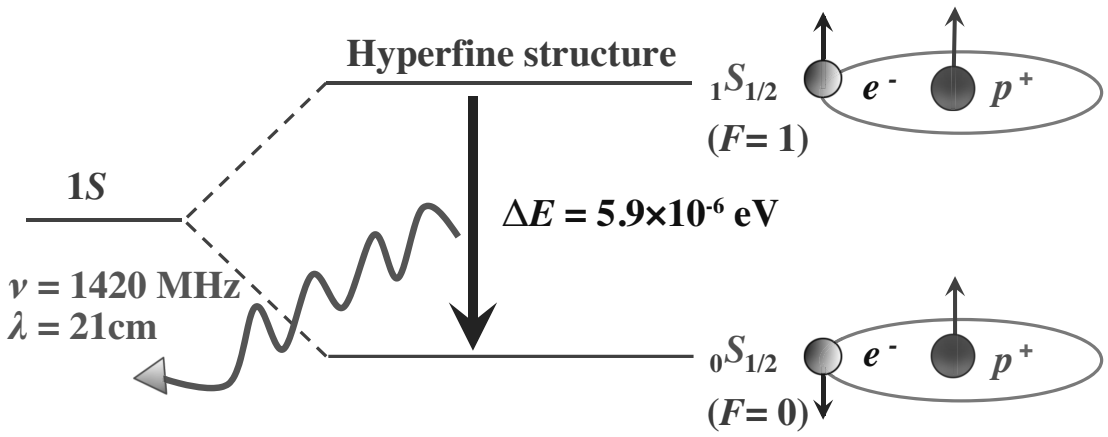

Figure 3.1: The schematic view of the hyperfine transition of neutral hydrogen.

momentum quantum numbers as

$$E_n = g(I)\frac{m}{m_{\rm p}}\frac{c\,h_{\rm p}R\,\alpha^2}{n^3}\left\{\frac{F(F+1)-I(I+1)-J(J+1)}{J(J+1)(J+2)}\right\}, \tag{3.1}$$

where F, I, J are respectively total angular momentum ($F = I + J$), nucleus's spin angular momentum (I), electron's total angular momentum ($J = L + S$), and electron's orbital angular momentum (L) and electron's spin angular momentum (S). $\alpha = \frac{2\pi e^2}{hc}$ is the fine-structure constant, $R = \frac{2\pi^2 me^4}{ch_{\rm p}^3}$ is Rydberg constant, n is the principal quantum number, m and e are mass and charge of a electron, and $m_{\rm p}$ is mass of a proton. $g(I)$ is called as g-factor[1].

For the atomic hydrogen in the grand state ($n = 1$ and $L = 0$), $S = 1/2$ and $I = 1/2$ lead to $J = 1/2$, and the energy difference between the parallel spin state ($F = 1$) and the antiparallel spin state ($F = 0$) is written by

$$E_{10} \equiv E_1 - E_0 = g(I)\frac{m}{m_{\rm p}}\frac{c\,h_{\rm p}R\,\alpha^2}{n^3}\frac{8}{3} \simeq 5.87\times10^{-6}\ {\rm eV}\,. \tag{3.2}$$

From the relation between energy and frequency $E_{10} = h_{\rm p}\nu_{10}$, this energy difference corresponds to a frequency of $\nu_{10} \simeq 1,420$ MHz and a wavelength of $\lambda_{10} \simeq 21.11$ cm, and a temperature of $T_{10} \equiv E_{10}/k_{\rm B} \simeq 0.06816$. Therefore the spectrum line attributed to the hyperfine transition of neutral hydrogen is called as *the 21cm line*. The schematic view of the hyperfine transition for neutral hydrogen is shown in Figure 3.1.

Besides neutral atomic hydrogen, for instance, deuterium and singly-ionized helium-3 can also have the hyperfine structure, and the other materials which is interesting on radio-astronomy can be found in (Townes, 1957).

[1] $g(I)$ is a proportional constant which makes a correlation among the magnetic moment of nuclear $\boldsymbol{\mu}$, nuclear magneton μ_N and angular moment $\boldsymbol{I}$. The magnetic moment of a proton $\boldsymbol{\mu}_{\rm p}$ is represented as $\boldsymbol{\mu}_{\rm p} = \frac{g(I)\mu_N}{\hbar_{\rm p}}\boldsymbol{I}$, where $\mu_N = \frac{e\hbar_{\rm p}}{2m_{\rm p}c}$ is $\left(\frac{m}{m_{\rm p}} \sim \frac{1}{1836}\right)$ times magnitude of the Bohr magneton $\mu_{\rm B}$ and $g(I) \sim 5.586$ for a proton.

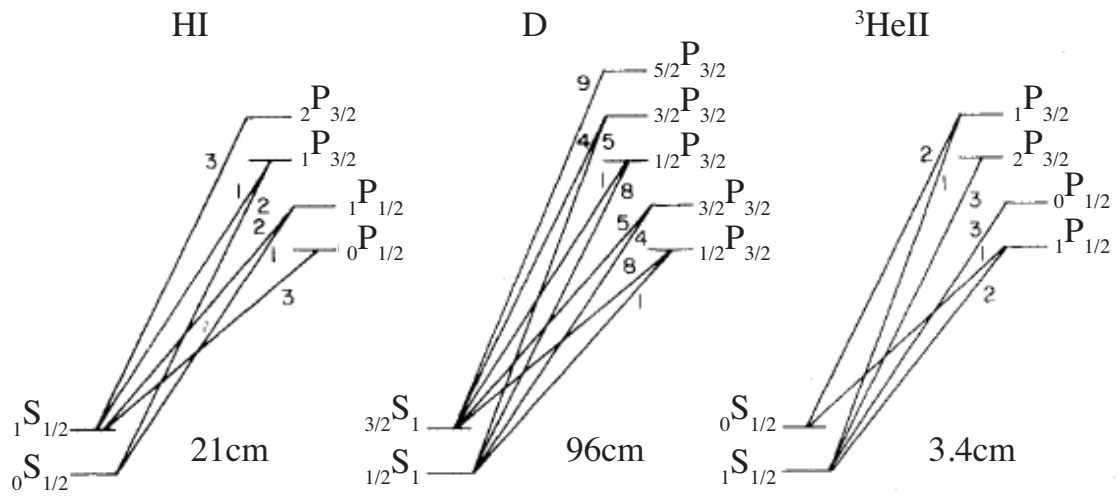

Figure 3.2: The level diagram for the Lyα transitions, which illustrates the WF process (Deguchi and Watson, 1985). The hyperfine sub-levels of the $1S$ and $2P$ states of H I, D and ^{3}He II are shown and the relative probabilities of the various transitions are indicated.

3.2 Spin temperature

In equilibrium, the relative abundance of the hyperfine excited state and the ground state is determined by *the spin temperature* $T_{\rm s}$ (or excitation temperature) as (Field, 1958)

$$\frac{n_1}{n_0} = \frac{g_1}{g_0} \exp\left[-\frac{h_{\rm p}\nu_{10}}{k_{\rm B}T_{\rm s}}\right] . \tag{3.3}$$

The spin temperature characterizes the thermal equilibrium between these two spin states, and $T_{\rm s}$ is determined by the balance between such processes as CMB photon absorption, collision between atoms, and scattering of Lyα photons. The scattering of Lyα is well known as the Wouthuysen-Field (WF) process (Wouthuysen, 1952; Field, 1958); a electron in the $n = 1$ level with a given spin state absorbs a Lyα or a Lyman-series photon to jump to the $n \geq 2$ level and then spontaneously decays back to the $n = 1$ level with a different spin state. The hyperfine sublevels of the $1S$ and $2P$ states of H I, D and ^{3}He II are illustrated in Figure 3.2, which describes the level diagram for the WF process.

In general, these processes can couple the spin temperature to the kinetic temperate of the gas $T_{\rm k}$ and the brightness temperature of the radiation field T_α

$$T_{\rm s} = \frac{T_{\rm CMB} + y_{\rm c}T_{\rm k} + y_\alpha T_\alpha}{1 + y_{\rm c} + y_\alpha} , \tag{3.4}$$

where $y_{\rm c}$ and y_α are the coupling factors of the collisional process and the WF process, respectively.

The coupling factors can be written as

$$y_{\rm c} \equiv \frac{C_{10}}{A_{10}}\frac{T_*}{T_{\rm k}} = \frac{\sum_i n^i \kappa^i_{10}}{A_{10}}\frac{T_*}{T_{\rm k}}\,, \tag{3.5}$$

and

$$y_\alpha \equiv \frac{P_{10}}{A_{10}}\frac{T_*}{T_\alpha} = \frac{4}{27}\frac{P_\alpha}{A_{10}}\frac{T_*}{T_\alpha}\,, \tag{3.6}$$

where A_{10} is the spontaneous decay rate from state 1 to 0, T_* is the equivalent temperature defined as $T_* \equiv h_{\rm p}\nu_{10}/k_{\rm B}$.

C_{10} is the rate of collisional de-excitation and κ^i_{10} is the rate coefficient for spin de-excitation in collisions with that species (Zygelman, 2005; Sigurdson and Furlanetto, 2006; Furlanetto and Furlanetto, 2007a; Furlanetto and Furlanetto, 2007b). We show these rates as a function of the kinetic temperature of gas in Figure 3.3. The total coupling coefficient is given by the sum over all species.

P_{10} is the rate of de-excitation due to the absorption of a Lyα photon, which is related to the total scattering rate of Lyα photons by $4P_\alpha/27$ for H I. For instance, P_{10} for deuterium and helium-3 can be written as follow;

$$P_{10} = \begin{cases} 4P_\alpha/27 & \text{for H I} \\ 16P_\alpha/81 & \text{for D} \\ 4P_\alpha/9 & \text{for } ^3\text{He II} \end{cases} \tag{3.7}$$

In Figure 3.4, we show the evolution of the temperature for CMB ($T_{\rm CMB}$), gas in the IGM ($T_{\rm k}$), which corresponds to the kinetic temperature of gas, and the spin temperature ($T_{\rm s}$). In the right panel, we take into account only the collisional process and the coupling with the radiation field is ignored. We here plot the result calculated from RECFAST[2] (Seager et al., 1999, 2000). On the other hand, in the right panel, we here take into account the gas heating by UV/X-ray sources and the pumping processes by Lyα photons. To include such processes, we have to know the evolution of UV/X-ray background or sources from observations and theoretical aspects. We here adopt the result from the semi-numerical simulation of the high-redshift 21cm signal (21cmFAST[3]) (Mesinger et al., 2011). In the following works from Chap. 4 to Chap. 5, we adopt some prediction for the UV/X-ray background and take into account the couplings with radiation field.

[2]http://www.astro.ubc.ca/people/scott/recfast.html
[3]http://homepage.sns.it/mesinger/DexM___21cmFAST.html

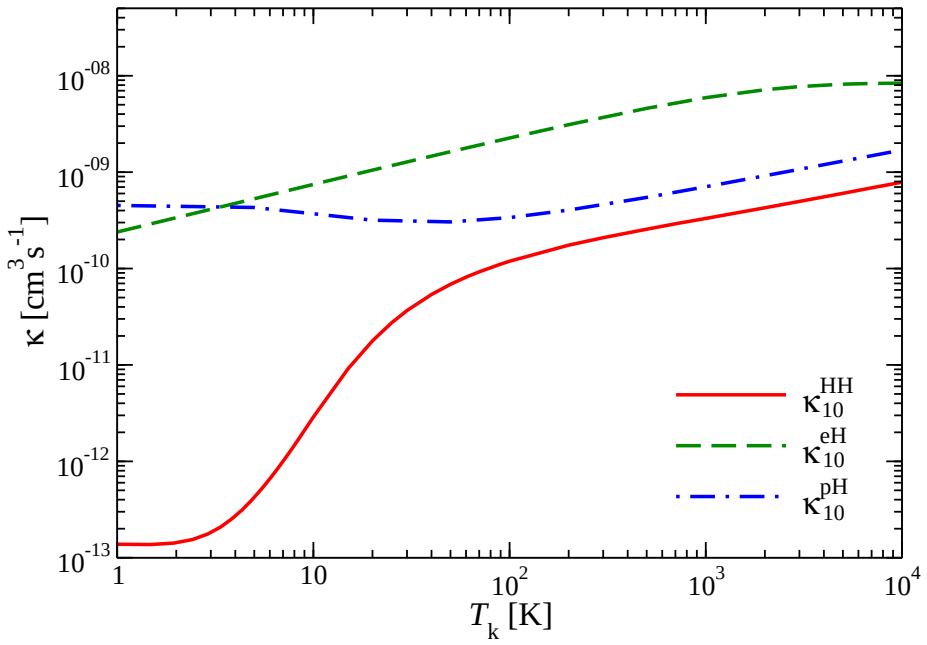

Figure 3.3: De-excitation rate coefficients for H-H collisions (solid/red line), H-e^- collisions (dashed/green line) and H-p collisions (dot-dashed/blue line) as a function of the kinetic temperature of gas $T_{\rm k}$.

3.3 Brightness temperature

If CMB photons propagate through a uniform cloud with $T_{\rm s} = $ const., the observed brightness temperature at frequency ν can be written by

$$T_{\rm b}(z) = T_{\rm CMB}(z)e^{-\tau(z)} + \left(1 - e^{-\tau(z)}\right) \frac{h_{\rm p}k_{\rm B}}{\exp(h_{\rm p}\nu/k_{\rm B}T_{\rm s}) - 1} \tag{3.8}$$

$$\simeq T_{\rm CMB}(z)e^{-\tau(z)} + \left(1 - e^{-\tau(z)}\right) T_{\rm s}(z)\,, \tag{3.9}$$

where $\tau(z)$ is the optical depth to photons, $T_{\rm CMB}(z)$ is the brightness temperature of the CMB in the absence of absorption. In the second line of 3.9, we apply the approximation in the Rayleigh-Jeans limit ($h_{\rm p}\nu \ll k_{\rm B}T_{\rm s}$).

When the line profile is unbroadened; $\phi(\nu) = \delta(\nu - \nu_0)$, the optical depth corresponds to that of the IGM at redshift z. For neutral hydrogen, the optical depth of the diffuse IGM is given by (Madau et al., 1997)

$$\tau(z) = \frac{3}{32\pi} \frac{c^2 h_{\rm p} A_{10}}{\nu_{10}^2 k_{\rm B} T_{\rm s}(z)} \frac{n_{\rm HI}(z)}{(1+z)({\rm d}v_\parallel/{\rm d}r_\parallel)}\,, \tag{3.10}$$

where $A_{10} = 2.85 \times 10^{-15}$ s^{-1} is the spontaneous decay rate from state 1 to state 0, ${\rm d}v_\parallel/{\rm d}r_\parallel$ is the gradient of the proper velocity along the line of sight, which includes both the Hubble expansion and the peculiar velocity.

The change in the brightness temperature is seen as the contrast to the CMB, and the differ-

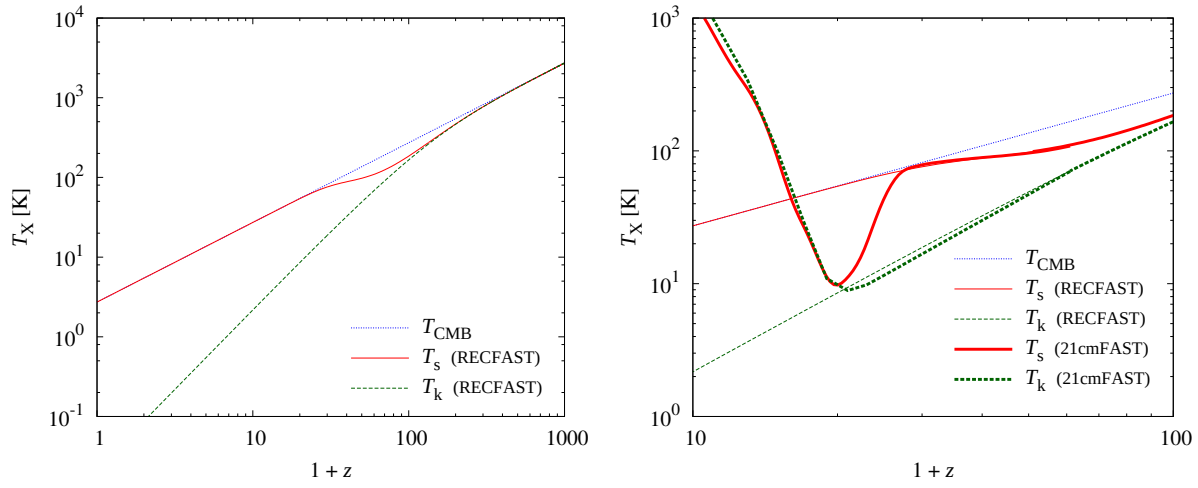

Figure 3.4: The evolution of the CMB ($T_{\rm CMB}$), the gas ($T_{\rm k}$) and the spin temperature ($T_{\rm s}$). (*Left*) The spin temperature includes only collisional coupling and only adiabatic cooling and Compton heating are involved for the IGM temperature evolution (from RECFAST). (*Right*) The heating by UV/X-ray sources and the pumping process by Lyα photons are included (from 21cmFAST).

ential brightness temperature observed at the present time is given by

$$\delta T_{\rm b} = T_{\rm b} - T_{\rm CMB} = \frac{(1 - e^{-\tau(z)})\,[T_{\rm s}(z) - T_{\rm CMB}(z)]}{1+z}\,. \tag{3.11}$$

As one can see, if the spin temperature completely couples to the CMB temperature, no net effect can not be observed as neither emission nor absorption. When the spin temperature is larger than the CMB temperature, the signal is observed as emission line ($\delta T_{\rm b} > 0$). To the contrary, when the spin temperature is lower than the CMB temperature, the signal is observed as absorption line to ($\delta T_{\rm b} < 0$).

If we assume optically thin cloud, $\tau(z) \ll 1$, the brightness temperature given by Eq. (4.13) is rewritten as

$$\delta T_{\rm b}(z) \simeq \frac{T_{\rm s}(z) - T_{\rm CMB}(z)}{1+z}\tau(z) \tag{3.12}$$

$$\simeq 10\, x_{\rm HI}(1+\delta)\left(1 - \frac{T_{\rm CMB}(z)}{T_{\rm s}(z)}\right)(1+z)^{1/2}\left(\frac{H(z)/(1+z)}{{\rm d}v_\parallel/{\rm d}r_\parallel}\right)\ {\rm mK}\,, \tag{3.13}$$

where $x_{\rm HI}$ is the ionization fraction for H I. We have substituted the velocity $H(z)/(1+z)$ in the third line, but this assumption is valid only for the uniform Hubble expansion and reasonably satisfied at high redshifts. Furthermore, we have substituted the local number density of the neutral hydrogen in the IGM

$$n_{\rm HI} = \bar{n}_{\rm HI}(1+\delta) \tag{3.14}$$

$$= (1 - Y_{\rm p})(\Omega_{\rm b}/\Omega_{\rm m})(\rho_{\rm m}/m_{\rm H})(1+\delta)\ , \tag{3.15}$$

Species	State	λ_{10} [cm]	ν_{10} [MHz]	A_{10} [s^{-1}]	g_1/g_0
H I	${}_1S_{1/2} - {}_0S_{1/2}$	21.11	1420.4	2.876×10^{-15}	3/1
D	${}_{3/2}S_1 - {}_{1/2}S_1$	91.6	327.3	4.695×10^{-17}	3/1
^{3}He II	${}_0S_{1/2} - {}_1S_{1/2}$	3.46	8665.7	1.959×10^{-12}	1/3

Table 3.1: The parameters related to the hyperfine transition for H I, D and ^{3}He II. λ_{10} and ν_{10} are the wave-length and frequency corresponding to the energy of the hyperfine transition, A_{10} is the spontaneous decay rate[2], and g_1/g_0 is the statistical weight of first-excited/ground states.

where $\bar{n}_{\rm HI}$ is the mean number density of the neutral hydrogen, $Y_{\rm p}$ is the helium fraction and $m_{\rm H}$ is the mass of a hydrogen atom.

In addition to the 21cm line of neutral hydrogen, there are some interesting spectra line on radio-astronomy, for instance isotope hydrogen (deuterium; D) and singly-ionized helium-3 ion, and we show some values related to the hyperfine transition for these materials in Table 4.1.

The brightness temperature can be given by the same form with Eq. (3.13) as follows;

$$\delta T_{\rm b,D}(z) \simeq 0.08\, x_{\rm HI}(1+\delta)\left(\frac{[{\rm D/H}]}{3\times10^{-5}}\right)\left(1-\frac{T_{\rm CMB}}{T_{\rm s,D}}\right)(1+z)^{1/2}\ \mu{\rm K}\,, \tag{3.16}$$

$$\delta T_{\rm b,{}^3He_{II}}(z) \simeq 0.5\, x_{\rm HeII}(1+\delta)\left(\frac{[^3{\rm He/H}]}{10^{-5}}\right)\left(1-\frac{T_{\rm CMB}}{T_{\rm s,He}}\right)(1+z)^{1/2}\ \mu{\rm K}\,, \tag{3.17}$$

where $x_{\rm HI}$ and $x_{\rm HeII}$ are respectively the ionization fraction of H I and He II, and the spin temperature is defined separately for D and ^{3}He II.

3.4 Thermal history of the IGM

To calculate the signal from H I due to the hyperfine transition, an estimation of its ionization states and abundances is required. To achieve this, we hove to solve the balance equations between the ionization and recombination processes. These processes are highly dependent on the environment in the IGM, e.g., the density and the temperature of gas. The photo-ionization and the heating processes through the IGM are also determined by the background radiation field. We here estimate the evolution of the abundance for each ionization state and the gas temperature in the IGM following the manner of (Fukugita and Kawasaki, 1994).

3.4.1 Ionization states of hydrogen and helium

We here assume that the system contains only H and He, the abundance of each ionization state, i.e. H I, H II, He I, He II and He III, is given by solving the balance equation between the

[2]The values of A_{10} for some materials which is interesting on radio-astronomy can be found in (Townes, 1957; Gould, 1994; Syunyaev, 1966; Goldwire and Goss, 1967).

ionization and recombination processes. The evolution of H I and H II are determined by

$$\frac{d}{dt}\left[\frac{n_{\rm HII}}{n_{\rm H}}\right] = \Gamma_{\rm HI} n_e \frac{n_{\rm HI}}{n_{\rm H}} + \beta_{\rm HI} n_e \frac{n_{\rm HI}}{n_{\rm H}} - \alpha_{\rm HII} n_e \frac{n_{\rm HII}}{n_{\rm H}}\,, \tag{3.18}$$

where n_e is the number density of electron, $n_{\rm HI}$ and $n_{\rm HII}$ are respectively the number densities of the neutral and the ionized hydrogen, and $n_{\rm H} \equiv n_{\rm HI} + n_{\rm HII}$ is the total number density of hydrogen.

The evolution of He I, He II and He III is determined by

$$\begin{aligned}\frac{d}{dt}\left[\frac{n_{\rm HeII}}{n_{\rm He}}\right] = {} & \Gamma_{\rm HeI} n_e \frac{n_{\rm HeI}}{n_{\rm He}} + \beta_{\rm HeI} n_e \frac{n_{\rm HeI}}{n_{\rm He}} - \beta_{\rm HeII} n_e \frac{n_{\rm HeII}}{n_{\rm He}} \\ & - (\alpha_{\rm HeII} + \xi_{\rm HeII}) n_e \frac{n_{\rm HeII}}{n_{\rm He}} + \alpha_{\rm HeIII} n_e \frac{n_{\rm HeIII}}{n_{\rm He}}\,,\end{aligned} \tag{3.19}$$

and

$$\frac{d}{dt}\left[\frac{n_{\rm HeIII}}{n_{\rm He}}\right] = \Gamma_{\rm HeII} n_e \frac{n_{\rm HeII}}{n_{\rm He}} + \beta_{\rm HeII} n_e \frac{n_{\rm HeII}}{n_{\rm He}} - \alpha_{\rm HeIII} n_e \frac{n_{\rm HeIII}}{n_{\rm He}}\,, \tag{3.20}$$

where $n_{\rm HeI}$, $n_{\rm HeII}$ and $n_{\rm HeIII}$ are respectively the number densities of the neutral, the singly-ionized and the doubly-ionized helium, and $n_{\rm He} \equiv n_{\rm HeI} + n_{\rm HeII} + n_{\rm HeIII}$ is the total number density of helium.

Assuming the ionization equilibrium, the electron number density is given by

$$n_e = n_{\rm HII} + n_{\rm HeII} + 2n_{\rm HeIII}\,, \tag{3.21}$$

and the abundance of each ionization state in this system is determined by these four equations, i.e. Eqs. (3.18)-(3.21).

Then, these functions used in the ionization equations are; the photo-ionization rate $\Gamma_{\rm X}$, the recombination rate $\alpha_{\rm X}$, the dielectronic recombination rate $\xi_{\rm X}$, and the collisional ionization rate $\beta_{\rm X}$. The label X represents the each component, X $\in$ {H I, H II, He I, He II, He III}. The functions for $\alpha_{\rm X}$, $\beta_{\rm X}$ and $\xi_{\rm X}$, are summarized in Appendix A.1 (Spitzer, 1978; Verner and Ferland, 1996). These values depend on the temperature of gas and we have to solve for the evolution of the gas temperature simultaneously together with the set of above four equations for the ionization states.

3.4.2 Evolution of the gas temperature in IGM

While the evolution of each ionization state depends on the temperature of gas in the IGM, the gas temperature also depends on the value of the local density and the flux of the background radiation through the heating or cooling processes. Assuming that the IGM is in the thermal equilibrium, the entropy equation can be written as (Mo et al., 2010)

$$\frac{d\ln T_{\rm g}}{d\ln(1+z)} = (\gamma - 1)\left[3 + \frac{1}{(\gamma-1)}\frac{d\ln\mu}{d\ln(1+z)} - \frac{\mathcal{H} - \Lambda}{H(z)\, n_{\rm b}\, k_{\rm B} T_{\rm g}}\right]\,, \tag{3.22}$$

where $n_{\rm b}$ is the baryon number density, γ is the adiabatic index, μ is the mean molecular weight, and $H(z)$ is the Hubble parameter. $\mathcal{H}$ and Λ are the heating and cooling functions, respectively. We summarize the cooling function in Appendix A.3 (Black, 1981; Cen, 1992). The first term in the right hand side of Eq. (3.22) corresponds to the adiabatic cooling through the Hubble expansion.

Chapter 4

Probing large scale filaments with H I and ^{3}He II

We explore the observability of the neutral hydrogen (H I) and the singly-ionized isotope helium-3 (^{3}He II) in the intergalactic medium (IGM) from the Epoch of Reionization down to the local Universe. The hyperfine transition of ^{3}He II, which is not as well known as the H I transition, has energy splitting corresponding to 8 cm. It also has a larger spontaneous decay rate than that of neutral hydrogen, whereas its primordial abundance is much smaller. Although both species are mostly ionized in the IGM, the balance between ionization and recombination in moderately high density regions renders them abundant enough to be observed. We estimate the emission signal of both hyperfine transitions from large scale filamentary structures and discuss the prospects for observing them with current and future radio telescopes. We conclude that H I in filaments is possibly observable even with current telescopes after 100 hours of observation. On the other hand, ^{3}He II is only detectable with future telescopes, such as SKA, after the same amount of time.

4.1 Introduction

Since the prediction of the 21 cm hyperfine transition by van de Hulst (1945) and its first detection by Ewen and Purcell (1951) and Muller and Oort (1951), forbidden quantum transition lines have been powerful tools in exploring various astrophysical systems. The advent of new larger and more sensitive radio telescopes makes it possible to use such tools for exploring even higher redshifts and lower density environments. Two recent examples are the use of redshifted 21 cm for exploring the Epoch of Reionization (EoR) (see e.g., Furlanetto et al. (2006a); Pritchard and Loeb (2012); Zaroubi (2013)); and for mapping neutral gas around redshift $\sim$ 1-2 to probe the baryon acoustic peaks (Chang et al., 2008). Another line, that has been discussed in the literature, is the singly-ionized helium-3 isotope, ^{3}He II (Townes, 1957; Sunyaev, 1966; Goldwire and Goss, 1967; Rood et al., 1979; Bell, 2000; McQuinn and Switzer, 2009; Bagla and Loeb, 2009). In this study we propose to use H I and ^{3}He II to detect large scale filaments and the accumulation of baryons within them as a function of redshift.

At the local Universe, most of the baryons in the intergalactic space reside in filamentary structures, the so-called cosmic web (Bond et al., 1996). These filaments are readily seen by modern galaxy surveys, such as the 2-degree Field Galaxy Redshift Survey (Colless et al., 2001; Erdoğdu et al., 2004), the Sloan Digital Sky Survey (York et al., 2000) and the 2-Micron All-Sky Survey (Skrutskie et al., 2006). Unfortunately, however, such surveys are not able to probe the baryonic content of these filaments and its distribution, where less than half of baryons at the local Universe have been identified (Cen and Ostriker, 1999; Fukugita and Peebles, 2004).

The observation of filamentary structures in the IGM through the hyperfine transition of neutral hydrogen can be a powerful tool that has the potential for detecting the missing baryons in the local Universe (see e.g., Popping et al. (2009) and Popping and Braun (2011)). However, below redshift ~ 6, the detection of H I in the diffuse IGM becomes very difficult as the Universe reionizes and a very small neutral fraction is left. Despite this difficulty, Chang et al. (2010) and Masui et al. (2012) have detected H I at low redshift by cross correlating the aggregate 21-cm glow with data from other probes of large-scale structure. Still, the signal of the auto-correlation at low-redshifts can be interpreted as an upper bound on the 21 cm signal (Switzer et al., 2013). Direct detection of H I from IGM filaments has not been reported yet.

Observation of ^{3}He II transition from the diffuse and filamentary structure in the IGM is very difficult to carry out, mainly because of its low abundance relative to hydrogen, and therefore, in principle in harder to detect. Furthermore, the sensitivity of the current radio telescopes at the appropriate frequency range is too poor for such a task. However, despite the low primordial abundance of ^{3}He relative to hydrogen ($\sim 10^{-5}$), it has some mitigating factors that render it observationally accessible. These factors are as follows:

1. The spontaneous decay rate of ^{3}He II ($A_{10} = 1.959 \times 10^{-12}$ s^{-1}) is $\sim$680 times larger than that of the H I ($A_{10} = 2.876 \times 10^{-15}$ s^{-1}) (Gould, 1994; Sunyaev, 1966; Goldwire and Goss, 1967), which significantly increases its emission rate.

2. The ionization energy of He II (54.4 eV) is 4 times larger than that of neutral hydrogen (13.6 eV), namely, it requires harder photons to fully ionize. Conversely, this difference in ionization energy causes the He III recombination rate to be $\sim$5 times larger than that of H II (Verner and Ferland, 1996). Hence, the abundance fraction of ^{3}He II in the IGM should be larger than that of H I.

3. The line transition occurs at a frequency of 8.7 GHz, in which the foreground synchrotron radiation from our galaxy and distortions from the terrestrial ionosphere are both less pronounced.

The overdensity of filaments in the IGM is roughly of the order of 10-100 times the mean density of the Universe. Therefore, given the size of such filaments, one can accumulate a sizable column density of both H I and ^{3}He II, in particular if they are elongated along the line of sight. Furthermore, at these densities, the recombination rates for both species are generally shorter than Hubble time and a reasonable fraction of H I and He II is expected to be present. Detection of either species will go a long way in accounting for the baryons in the Universe at the redshift

of detection. In addition, the relative abundance of these species can constrain the hardness of the UV background as a function of redshift.

Our aim in this study is to estimate the prospect of observing these two species within large scale structure filaments with the present and future radio telescopes in the redshift range $\sim 0-8$. Here, we consider a number of single dish telescopes, e.g., GBT[1] (Chang et al., 2010; Masui et al., 2012) and Arecibo[2](Freudling et al., 2011), and radio interferometers such as EVLA[3], and GMRT[4]. Note that LOFAR does not have the proper frequency range for observing either of the two transitions, except H I at $z \gtrsim 6$ (van Haarlem et al., 2013a). We also make predictions for future telescopes that generally have more sensitivity, a larger field of view and wider frequency coverage: FAST[5], MeerKAT[6] and, of course, the mega radio telescope SKA[7], which is expected to be completed around 2024.

This chapter is organized as follow. We summarize the physical models used in the paper for calculating the H I and ^{3}He II signal from large scale filamentary structure in the IGM in Section 4.2. In the same section, we also evaluate the abundance of each ionization state, the gas temperature in the IGM and the spin and brightness temperatures. The predicted hyperfine transition signal of H I and ^{3}He II for simple models as well as for filaments from large scale structure simulations is presented in Section 4.3. Finally we discuss the prospects of observing the emission signal of the hyperfine transition from filamentary structures with current and future radio telescopes in Section 4.3.3. The paper ends with a conclusion and discussion section.

Throughout this paper, we adopt the cosmological parameters from the WMAP 7 years data (Komatsu et al., 2011).

4.2 The physical Model for H I and ^{3}He II

To calculate the signal from H I and ^{3}He II, an estimation of their ionization states and abundances is required. To achieve this, we solve the balance equations between the ionization and recombination processes. These processes are highly dependent on the environment in the IGM, e.g. the density and the temperature of gas. The photo-ionization and the heating processes through the IGM are also determined by the background radiation field. We here adopt the UV/X-ray background model of Haardt and Madau (2012), hereafter "HM12".

Furthermore, the signal of the hyperfine transition is related to the relative occupation number of the excited state relative to the ground state, which determines the spin temperature. The spin state is mainly affected by two processes; one is the collisional excitation process with other species or itself, and the other is the Ly-α pumping of the line which is called as the Wouthuysen-Field (WF) process (Wouthuysen, 1952; Field, 1958, 1959). We estimate the spin temperature taking into account both these processes.

[1]https://science.nrao.edu/facilities/gbt
[2]http://www.naic.edu/
[3]https://science.nrao.edu/facilities/vla
[4]http://gmrt.ncra.tifr.res.in/
[5]http://fast.bao.ac.cn/en/FAST.html
[6]http://www.ska.ac.za/meerkat/index.php
[7]http://www.skatelescope.org/

In this section, we summarize the physical models for the estimation of the hyperfine transition and its signal from the filamentary structure in the IGM. In Sec. 4.2.1 and 4.2.2, we estimate the evolution of the abundance for each ionization state and the gas temperature in the IGM following the manner of (Fukugita and Kawasaki, 1994) and adopting the photo-ionization rates $\Gamma(z)$ and the heating function $\mathcal{H}(z)$ given by HM12. In Sec. 4.2.3, we summarize the physical processes determining the spin state and estimate the spin temperature. Finally, we calculate the brightness temperature and estimate the signal from the filamentary structure in Sec. 4.2.4.

4.2.1 Ionization state of hydrogen and helium

We here assume that the system contains only H and He, the abundance of each ionization state, i.e. H I, H II, He I, He II and He III, is given by solving the balance equation between the ionization and recombination processes. The evolution of H I and H II are determined by Eq. (3.18), and the total number density of hydrogen is given by $n_{\rm H} \equiv n_{\rm HI} + n_{\rm HII}$.

The evolution of He I, He II and He III is determined by Eqs. (3.19) and (3.20), and the total number density of helium is given by $n_{\rm He} \equiv n_{\rm HeI} + n_{\rm HeII} + n_{\rm HeIII}$.

Assuming the ionization equilibrium, the electron number density is given by Eq. (3.21) and the abundance of each ionization state in this system is determined by these four equations, i.e., Eqs. (3.18)-(3.21).

Then, we adopt the value of each photo-ionization state $\Gamma_{\rm X}$ from HM12, which takes into account the photo-ionization heating of H I, He I and He II , and Compton heating. The other functions adopted in our calculation, $\alpha_{\rm X}$, $\beta_{\rm X}$ and $\xi_{\rm X}$, are summarized in Appendix A.1 (Spitzer, 1978; Verner and Ferland, 1996). These values depend on the temperature of gas and we have to solve for the evolution of the gas temperature simultaneously together with the set of above four equations for the ionization states.

4.2.2 Gas temperature

While the evolution of each ionization state depends on the temperature of gas in the IGM, the gas temperature also depends on the value of the local density and the flux of the background radiation through the heating or cooling processes. Assuming that the IGM is in the thermal equilibrium, the evolution of the gas temperature is given by Eq. (3.22). Then, we adopt the HM12 heating function $\mathcal{H}$, wheres the cooling function used in this work is summarized in Appendix A.3 (Black, 1981; Cen, 1992).

To describe the local density contrast of baryons, we define the local number density of each baryon component as,

$$n_{\rm X} \equiv (1+\delta)\, f_{\rm b}\, \bar{n}_{\rm X} = \Delta_{\rm b}\, \bar{n}_{\rm X}\,, \tag{4.1}$$

where δ is the density fluctuation of matter, $f_{\rm b}$ represents the bias, $\bar{n}_{\rm X}$ is the average number density of a component X, and we define the the baryon density contrast as $\Delta_{\rm b} \equiv (1+\delta)\, f_{\rm b}$. The distribution of baryons might be different from that of matter, but we assume this effect should be small on the scales in which we are interested in this chapter, i.e. $f_{\rm b} = 1$. Therefore

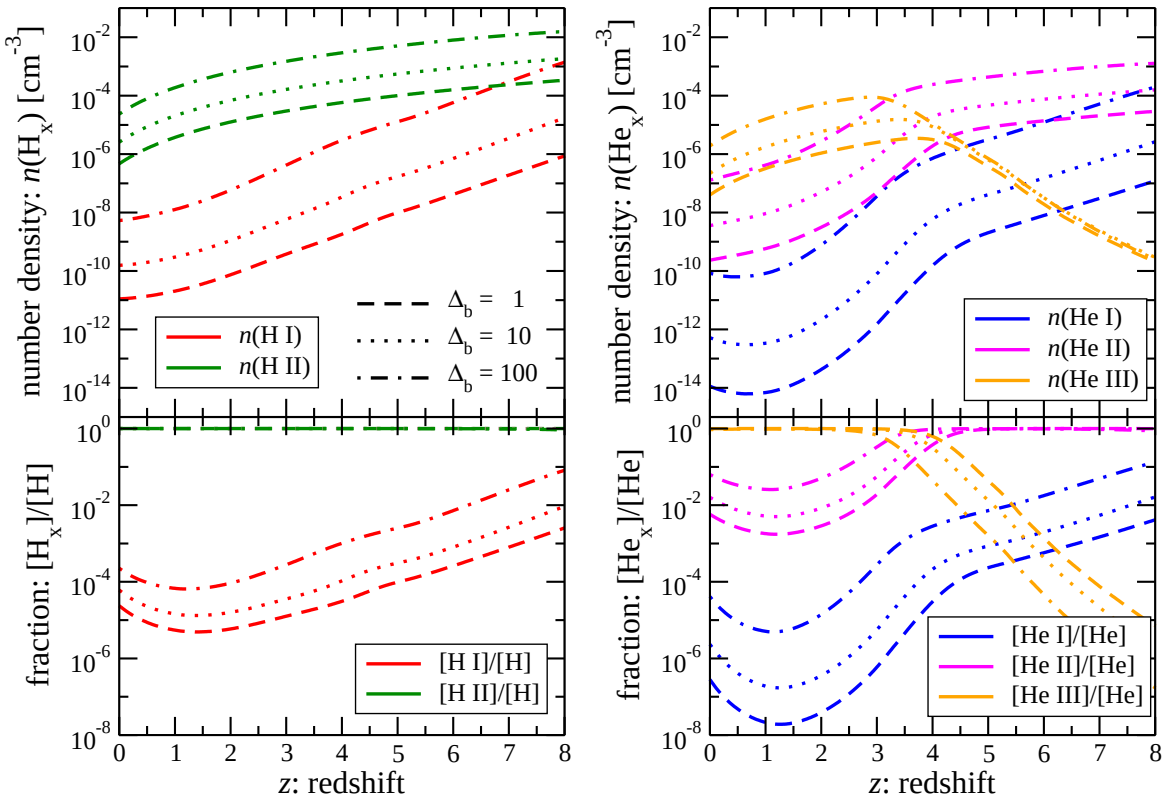

Figure 4.1: The time evolution of the ionization states for the hydrogen (Left) and the helium (Right). The top panels show the number density of each ionization state, while the bottom panels show their fractional abundance against the total number of hydrogen $n_{\mathrm{H_x}}/n_{\mathrm{H}}$ or helium $n_{\mathrm{He_x}}/n_{\mathrm{He}}$; the label X represents the each ionization state. The ionization states for the hydrogen are taken into account two states, H I (red) and H II (green), while the ones for the helium are taken into account three states, He I (blue), He II (magenta) and He III (orange). The different line types represent the different values of the baryon density contrast parameter Δ_{b} defined in Eq. (4.1), and dashed, dotted and dashed-dot lines respectively correspond to Δ_{b} =1, 10 and 100.

$\Delta_b = 1$ corresponds to the mean number density in the IGM. The definition of the baryon density contrast parameter Δ_{b} includes this uncertainties.

The interaction time scale of the ionization and recombination for each species are given by $t_{\mathrm{X}}^{\mathrm{ion}} = (\Gamma_{\mathrm{X}} + \beta_{\mathrm{X}} n_e)^{-1}$ and $t_{\mathrm{X}}^{\mathrm{rec}} = (\alpha_{\mathrm{X}} n_e)^{-1}$, respectively. If these time scales are much shorter than Hubble time, the assumption of the ionization equilibrium is valid. For example, the typical time scales for hydrogen in the IGM are respectively $t_{\mathrm{HI}}^{\mathrm{ion}} \sim (10^{-14}/\Gamma_{\mathrm{HI}}) \times 10^7$ yr and $t_{\mathrm{HII}}^{\mathrm{rec}} \sim \Delta_{\mathrm{b}}^{-1} \times 10^{11}$ yr at $z = 0$. Since the recombination time scale is longer than the Hubble expansion time at low-density region, the assumption of the ionization equilibrium is not satisfied for hydrogen. However, the condition for the assumption of ionization equilibrium is satisfied in the high-density region ($\Delta_{\mathrm{b}} \gtrsim 10$) such as in the case of filamentary structure in the IGM. In such a region, the local thermal equilibrium is also reasonably satisfied, since the interactions between the electrons and ionized species work effectively.

Assuming equilibrium, we solve these five independent equations Eqs. (3.18)-(3.22) simultaneously. We show the results of the abundance for some different values of the baryon density parameter, $\Delta_{\rm b} = 1$, 10 and 100, in Figure 4.1. We should note that the assumption of the equilibrium seems invalid for $\Delta_{\rm b} = 1$, but we show for comparison purpose.

4.2.3 Spin temperature

In this section, we summarize the spin temperature and its coupling factors due to collisions and to the Wouthuysen-Field (WF) effect for both neutral hydrogen H I and singly-ionized isotope helium-3 ^{3}He II.

The relative abundance of the hyperfine excited state and the ground state is determined by the spin temperature $T_{\rm s}$ as

$$\frac{n_1}{n_0} = (g_1/g_0) \exp\left[-\frac{h_{\rm p}\nu_{10}}{k_{\rm B}T_{\rm s}}\right], \tag{4.2}$$

where n_1 and n_0 are the numbers of hyperfine excited state and the ground state, respectively. The factor g_1/g_0 is the statistical weight of first-excited/ground state, $h_{\rm p}$ is the Planck constant, $k_{\rm B}$ is the Boltzmann constant, ν_{10} is the frequency which corresponds to the energy of the hyperfine transition.

The spin temperature is determined by two processes. One is the collisional excitation or de-excitation of the spin states. The other is the change of the spin states through the absorption and spontaneous re-emission of a Lyα photon or any Lyman-series photon (Madau et al., 1997; Shaver et al., 1999; Hirata, 2006; Furlanetto and Pritchard, 2006; Pritchard and Furlanetto, 2006). These two processes couple the spin temperature to the gas field and radiation field as (Field, 1958)

$$T_{\rm s} = \frac{(T_{\rm CMB} + y_{\rm c}T_{\rm k} + y_\alpha T_\alpha)}{(1 + y_{\rm c} + y_\alpha)}, \tag{4.3}$$

where $T_{\rm k}$ is the kinetic temperate of gas, T_α is the brightness temperature of the radiation field, $y_{\rm c}$ and y_α are the coupling factors of the collisional process and the WF process, respectively. The coupling factors can be written as

$$y_{\rm c} = \frac{C_{10}}{A_{10}}\frac{T_*}{T_{\rm k}}, \qquad y_\alpha = \frac{P_{10}}{A_{10}}\frac{T_*}{T_\alpha}, \tag{4.4}$$

where A_{10} is the spontaneous decay rate from state 1 to 0, C_{10} is the rate of collisional de-excitation, P_{10} is the rate of de-excitation due to the absorption of a Lyα photon, and T_* is the equivalent temperature defined as $T_* \equiv h_{\rm p}\nu_{10}/k_{\rm B}$.

In general, the rate of collisional de-excitation is written as

$$C_{10} = n_e \sqrt{\frac{k_{\rm B}T_{\rm k}}{\pi m_e c^2}} c\bar{\sigma}, \tag{4.5}$$

Species	λ_{10} [cm]	ν_{10} [MHz]	A_{10} [s^{-1}]	λ_α [Å]	f_α	g_1/g_0	primordial abundance
H I	21.1	1420.4	2.876×10^{-15}	1215.67	0.4162	3/1	—
^{3}He II	3.46	8665.7	1.959×10^{-12}	303.78	0.4162	1/3	1.0×10^{-5}

Table 4.1: The parameters related to the hyperfine transitions for H I and ^{3}He II. λ_{10} and ν_{10} are the wave-length and frequency corresponding to the energy of the hyperfine transition, A_{10} is the spontaneous decay rate, λ_α and f_α is respectively the wave-length and the oscillator length of the Lyα transition, and g_1/g_0 is the statistical weight of first-excited/ground state. The primordial abundance for ^{3}He is expressed as the fractional abundance against hydrogen, i.e., ^{3}He/H.

and $\bar{\sigma}$ is the averaged cross-section for spin exchange given by

$$\bar{\sigma} = \frac{1}{(k_{\rm B}T_{\rm k})^2}\int_0^\infty dE\sigma(E)Ee^{-E/(k_{\rm B}T_{\rm k})}\,, \tag{4.6}$$

where $\sigma(E)$ is the cross-section for spin exchange as a function of collision energy.

The rate of de-excitation due to the absorption of Lyα photons is written as

$$P_{10} = \frac{4\pi e^2 f_\alpha}{m_e c}\begin{cases} \dfrac{4}{27}J_\alpha & \text{for H I} \\ \dfrac{4}{9}J_\alpha & \text{for } ^3\text{He II} \end{cases} \tag{4.7}$$

where e is the electron charge, m_e is the electron mass, f_α is the oscillator length of the Lyα transition, J_α is the flax at Lyα wave-length, and g_1/g_0 is the statistical weight of the first-excited/ground state. These values are defined for each hyperfine structure and we summarize some values related to these processes in Table 4.1. We give the detailed values on these rates for H I and ^{3}He II in the following sections.

H I : neutral hydrogen

For the collisional excitation of the neutral hydrogen (H I), the main process is the collision with a electron, while collisions with a proton or a neutral hydrogen atom themselves are sub-dominant. The total rate of collisional de-excitation can be expressed as the summation of these three processes;

$$C_{10}^{\rm H\,I} = \left[\kappa_{10}^{\rm HH}(T_{\rm k})n_{\rm H} + \kappa_{10}^{e\rm H}(T_{\rm k})n_e + \kappa_{10}^{p\rm H}(T_{\rm k})n_p\right]\,, \tag{4.8}$$

where $\kappa_{10}^{\rm HH}$, $\kappa_{10}^{e\rm H}$ and $\kappa_{10}^{p\rm H}$ are respectively the collisional rates for H-H, e-H and p-H processes, and we can find these values as a function of the kinetic temperature $T_{\rm k}$ in (Zygelman, 2005; Sigurdson and Furlanetto, 2006; Furlanetto and Furlanetto, 2007a; Furlanetto and Furlanetto, 2007b).

For the WF process of H I, following Eq. (4.7), the de-excitation rate is related to the radiation

field as

$$P_{10}^{\rm HI} = \frac{16\pi e^2 f_\alpha^{\rm HI}}{27 m_e c} J_{{\rm Ly}\alpha,{\rm HI}}\,, \tag{4.9}$$

where $f_\alpha^{\rm HI} = 0.4162$ is the oscillator length of the H I Lyα transition, and $J_{{\rm Ly}\alpha,{\rm HI}}$ is the flax at H I Lyα wave-length ($\lambda_{{\rm Ly}\alpha,{\rm HI}} = 1216$Å).

^{3}He II : singly-ionized isotope helium-3

The most dominant process of collisional coupling for the singly-ionized isotope helium-3 (^{3}He II) is the collision with electrons. Then, following Eq. (4.8), the rate of collisional process can be written as

$$C_{10}^{\rm ^3HeII} = n_e \sqrt{\frac{k_{\rm B} T_{\rm k}}{\pi m_e c^2}}\, c\, \bar{\sigma}^{e\,^3{\rm He}}\,, \tag{4.10}$$

and $\bar{\sigma}^{e\,^3{\rm He}}$ is the averaged cross-section of spin exchange between ^{3}He II and electron, which can be approximately given from (McQuinn and Switzer, 2009) as

$$\bar{\sigma}^{e\,^3{\rm He}} \simeq \frac{14.3{\rm eV}}{k_{\rm B} T_{\rm k}} a_o^2\,, \tag{4.11}$$

where a_o is the Bohr radius.

For the WF process of ^{3}He II, the de-excitation rate can be estimated from Eq. (4.7) in the same manner as the case of H I and given by

$$P_{10}^{\rm ^3HeII} = \frac{16\pi e^2 f_\alpha^{\rm HeII}}{9 m_e c} J_{{\rm Ly}\alpha,{\rm HeII}}\,, \tag{4.12}$$

where $f_\alpha^{\rm HeII} = 0.4162$ is the oscillator length of the He II Lyα transition, and $J_{{\rm HeII,Ly}\alpha}$ is the flax at He II Lyα wave-length ($\lambda_{{\rm Ly}\alpha,{\rm HeII}} = 304$Å).

In both cases, i.e. for H I and ^{3}He II, we have to assume the Ly-α flux as a function of redshift. Throughout this chapter, we adopt the recent model of UV/X-ray background from HM12.

We compute the spin temperature with the assumption that the kinetic temperature $T_{\rm k}$ and the color temperature T_α are coupled to the gas temperature $T_{\rm g}$; i.e., $T_{\rm k} \simeq T_\alpha \simeq T_{\rm g}$. We show the evolution of the spin temperature of H I and ^{3}He II in the left panel of Figure 4.2, and the kinetic temperature $T_{\rm k}$ and the temperature of CMB $T_{\rm CMB}$ are also plotted in the same panel.

Although the contribution of the radiative coupling to the spin temperature is so weak at low-redshifts, it becomes important around the EoR. Moreover some exotic models show that the contribution of X-ray alter the history of reionization dramatically (Furlanetto et al., 2006b; Shchekinov and Vasiliev, 2007), and the uncertainties sill remain on the estimation of the spin temperature around EoR or at high-redshift.

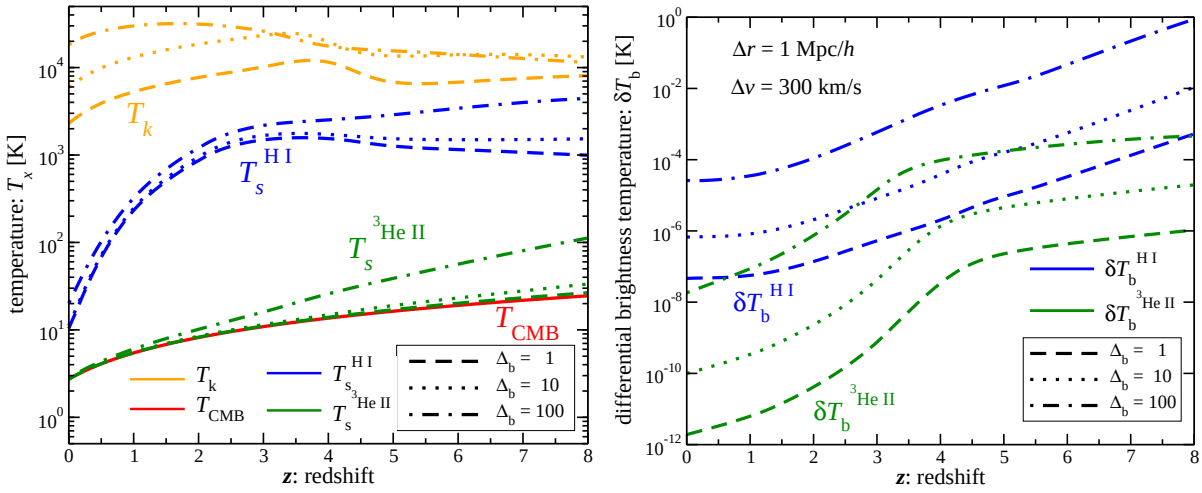

Figure 4.2: (Left) The time evolution of the kinetic temperature $T_{\rm k}$ (orange), the spin temperature of H I (blue) and ^{3}He II (green), and the temperature of CMB $T_{\rm CMB}$ (red), (from top to bottom). (Right) The evolution of the differential brightness temperature of H I and ^{3}He II as a function of redshift. In both panels, the different line types represent the different values of the baryon density contrast parameter $\Delta_{\rm b}$, and the dashed, dotted and dot-dashed lines respectively correspond to $\Delta_{\rm b} = 1$, 10 and 100 (from bottom to top). On the estimation of the differential brightness temperature, we assume the filament structure with 1 Mpc/h width ($\Delta r = 1$ Mpc/h) and the proper line-of-sight velocity to be $\Delta v = 300$ km/s.

4.2.4 Differential brightness temperature

In radio astronomy, the emission from the hyperfine transition of H I or ^{3}He II are observed, in term of the differential brightness temperature relative to the CMB, and given by

$$\delta T_{\rm b}^{\rm X}(z) \equiv T_{\rm b}^{\rm X}(z) - T_{\rm CMB}(z) = \frac{[T_{\rm s}^{\rm X}(z) - T_{\rm CMB}(z)](1 - e^{-\tau_{\rm X}(z)})}{1+z}\,, \tag{4.13}$$

where $T_{\rm b}^X$ is the brightness temperature and $\tau_{\rm X}(z)$ is the optical depth, where X marks either H I or ^{3}He II. In general, the optical depth is defined as

$$\tau_{\rm X}(z) = \frac{g_1}{g_0+g_1}\frac{c^2 h_{\rm p} A_{10}}{8\pi\nu_{10}^2 k_{\rm B}}\frac{n_{\rm X}(z)}{T_{\rm s}^{\rm X}(z)}\frac{1}{(dv_\parallel/dr_\parallel)}\,, \tag{4.14}$$

where $n_{\rm X}(z)$ is the number density of species X, and $dv_\parallel/dr_\parallel$ is the velocity gradient along the line-of-sight, including both the Hubble expansion and the peculiar velocity (Kaiser, 1987).

If the optically thin regime (i.e. $\tau \ll 1$), Eq. (4.13) can be rewritten as

$$\begin{aligned}\delta T_{\rm b}^{\rm X}(z) &\simeq \frac{\left[T_{\rm s}^{\rm X}(z) - T_{\rm CMB}(z)\right]\tau_{\rm X}(z)}{1+z} \\ &\simeq \frac{g_1}{g_0+g_1}\frac{c^2 h_{\rm p} A_{10}}{8\pi\nu_{10}^2 k_{\rm B}}\frac{n_{\rm X}(z)\Delta r}{(1+z)\Delta v}\left(1 - \frac{T_{\rm CMB}(z)}{T_{\rm s}^{\rm X}(z)}\right)\,,\end{aligned} \tag{4.15}$$

where Δr denotes the line-of-sight width of the filamentary structure and Δv denotes the proper

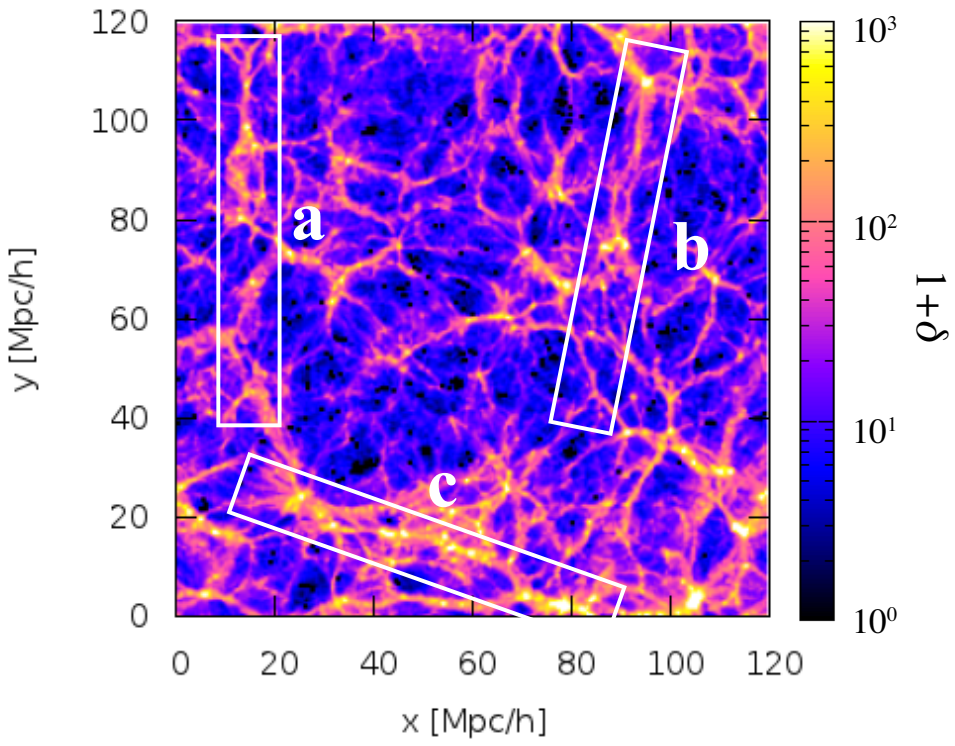

Figure 4.3: A 1.4 Mpc/h slice of the density field through the N-body simulation at present redshift. The color-bar represents the over density $1 + \delta$. The boxes and symbols are the appropriately-defined filamentary structures and their center positions.

line-of-sight velocity. In the second line in Eq. (4.15), we used the optical depth given by Eq. (4.14). Eq. (4.15) shows that the differential brightness temperature can be observed as the emission(absorption) signal when the spin temperature is larger(smaller) than the CMB.

We show the differential brightness temperature of H I and ^{3}He II in the right panel of Figure 4.2 for the different values of the baryon bias parameters, $\Delta_{\rm b} = 1$, 10 and 100. Here we assume the filament with the width $\Delta r = 1$ Mpc/h and the proper line-of-sight velocity $\Delta v = 300$ km/s. The H I column density of this filament corresponds to $N_{\rm HI} = n_{\rm HI}\Delta r \simeq 10^{15} - 10^{16}$ cm^{-2} with $\Delta_{\rm b} = 100$ around the present redshift.

The emission from ^{3}He II shows a different redshift dependence relative to that of H I. This is because the reionization state of H I is different from that of He. The drop in $\delta T_{\rm b}^{^3{\rm HeII}}$ around $z \sim 4$ corresponds to the epoch of He II reionization (He II→He III), where the fraction of He II for the total helium components decreases after that. Therefore it is expected that it becomes more difficult to observe ^{3}He II emission after $z \sim 4$. However the advantage of the observation with high-frequencies at low-redshifts also motivates us to attempt to probe the missing baryon in the filamentary structures through the emission line of the hyperfine transition of ^{3}He II.

4.3 The Signal Estimation

In the previous section, we estimated the brightness temperature of the hyperfine structures with some assumptions on the filamentary structure, which were about the density fluctuations δ, the proper line-of-sight velocity Δv and the width Δr of the filament. As a next step, we calculate the signals adopting more realistic values for the filaments from the N-body simulation of the large-scale structures.

First, as a preparation to estimate the signal from the filamentary structure, we summarize the N-body simulation used to make the large-scale structures and the procedure to estimate the signal of hyperfine transition based on the N-body simulation. Furthermore, we focus on the signal from an elongated filamentary structure and consider the signal as a result of observing the filament from various angles. Finally we summarize the sensitivity of the current and future radio telescopes to estimate their ability to detect the signal.

4.3.1 N-body Simulation

To make the snapshots of N-body data, we use the parallel Tree-Particle Mesh code *Gadget-2* (Springel, 2005) in its full Tree-PM mode. We employ 512^3 particles 120 Mpc/h on a side, and the minimum mass resolution corresponds to $9.68 \times 10^8 M_\odot/h$. The initial conditions are generated following the standard Zel'dovich approximation and we employ the linear matter transfer function computed from $CAMB$ (Lewis et al., 2000) in this step. We show the matter density field estimated through the N-body simulation at the present time in Figure 4.3. The frames and the symbols are, respectively, the appropriately-determined filamentary structures and their center position. We focus on the signals from these filaments later in the following section.

We here estimate the signal of the hyperfine transition for H I and ^{3}He II based on the N-body simulation of the large-scale structures. On the calculation of the brightness temperature, we firstly divide the simulation box into 256^3 grids and estimate the density contrast $\delta \equiv (\rho - \bar{\rho})/\bar{\rho}$ and the proper line-of-sight velocity Δv with Cloud-in-Cell (CIC) interpolation on each grid. Then we estimate the differential brightness temperature through Eq. (4.13) adopting the values of the density contrast and the proper line-of-sight velocity on each grid. Both signals from H I and ^{3}He II are estimated with above manner.

We show the thin sliced maps of the differential brightness temperature for H I and ^{3}He II at some redshift slices, which are $z = 0$, 1, 2 and 4, in Figure 4.4 and Figure 4.5, respectively. The depth of the slice along the line-of-sight is 1.4 Mpc/h for all, and we compute these two-dimensional maps by accumulating the signals of some thin slices on each patch. Please note, the depth of 1.4 Mpc/h along the line-of-sight corresponds to the frequency bandwidth of $\sim$0.7 MHz for the H I survey and $\sim$ 4 MHz for the ^{3}He II survey at $z = 0$.

We can see the filamentary structures in both cases through the brightness temperature, and the amplitudes are $\delta T_\mathrm{b} \sim 10^{-6}$ K for H I and $\sim 10^{-9}$ K for ^{3}He II in the maps at $z = 0$. The signals are lower than the signals calculated on the assumption for the filamentary structure with $\Delta_\mathrm{b} \simeq 100$ — this also applies for higher redshifts. As we can see from Figure 4.3, the density

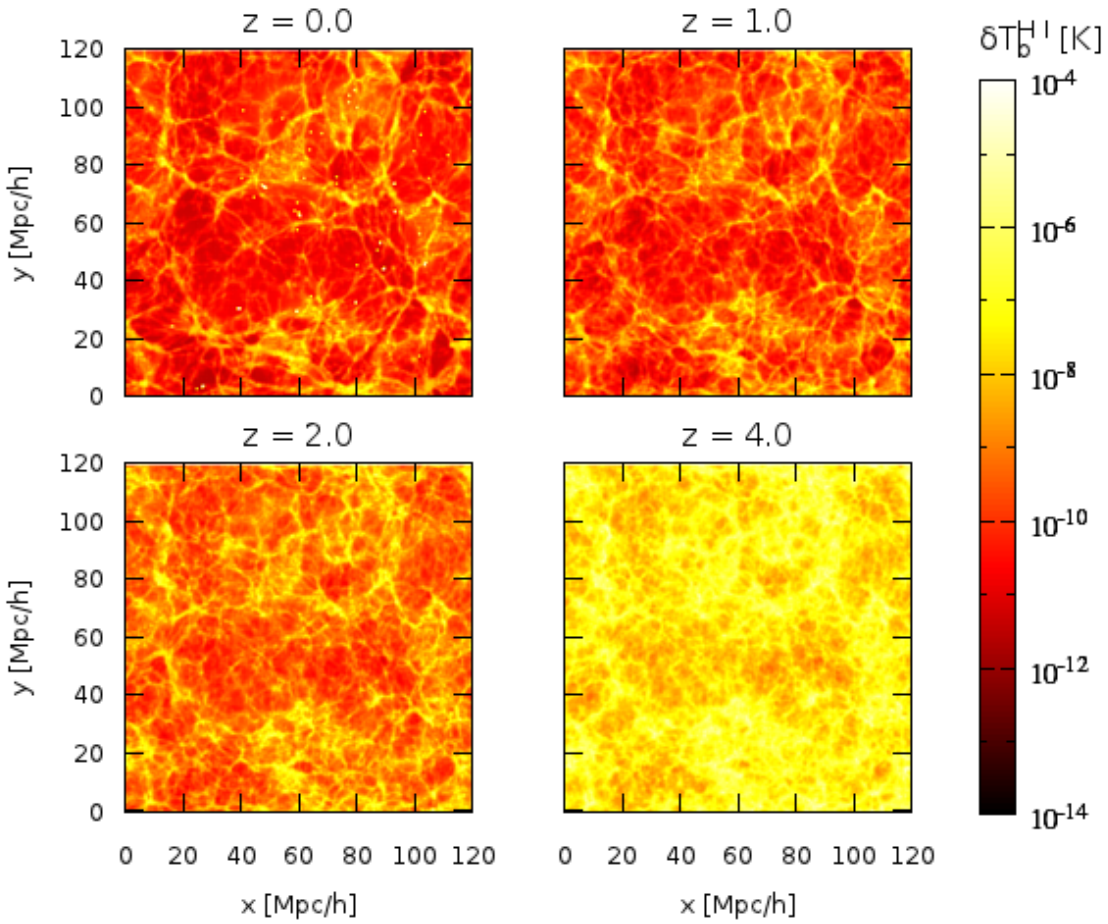

Figure 4.4: The thin sliced maps of the differential brightness temperature of H I at different redshift slices, which are at $z = 0$ (Top-Left), $z = 1$ (Top-Right), $z = 2$ (Bottom-Left) and $z = 4$ (Bottom-Right). We estimate the density contrast and the proper line-of-sight velocity from the snapshots of the N-body simulation, then calculate the differential brightness temperature through Eq. (4.13). All slices are 120 Mpc/h on a side and the depth along the line-of-sight are 1.4 Mpc/h.

contrast of the filaments is $\Delta_b \lesssim 100$ at present redshift. We can also clearly see the drastic drastic transition of ^{3}He II from $z = 4$ to $z = 2$, which reflects the He II reionization.

4.3.2 Signal from a filamentary structure

Here we focus on the signal from a filamentary structure. As confirmed from the optical observation of the large-scale structures, the observed filamentary structures have the elongated shapes (Erdoğdu et al., 2004; Choi et al., 2010; Pandey et al., 2011). When a filament extends toward the line-of-sight and the filament and the line-of-sight direction are parallel to each other, we can expect to detect the highest signal from the filamentary structure. On the other hand, when the filament and the line-of-sight direction are perpendicular to each other, the signal should be lower than the former case. Therefore the signal from a filamentary structure depends on the

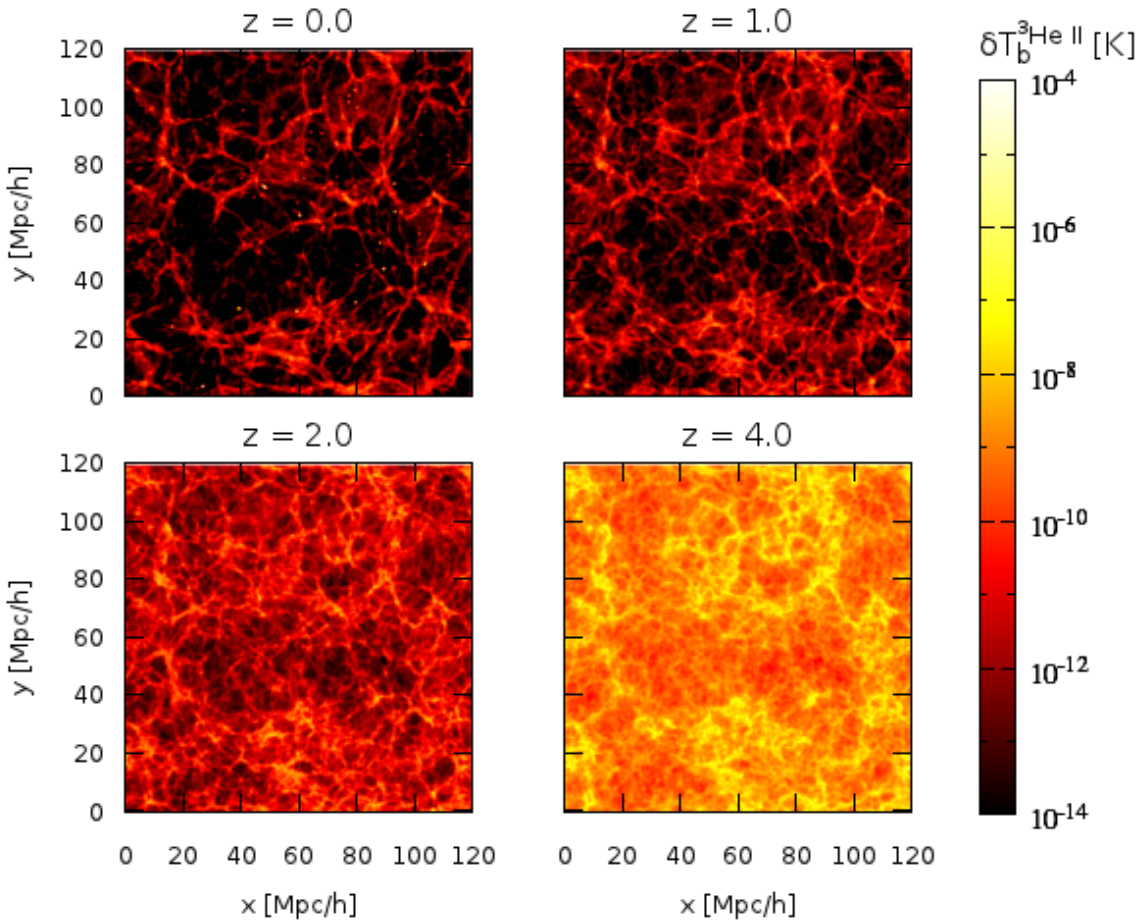

Figure 4.5: Same as Figure 4.4, except the maps are for the differential brightness temperature of ^{3}He II. The realization of N-body simulation is use the same one with the map of H I.

direction we observe the filament or the angle between the filament and the line-of-sight direction.

We estimate $\delta T_{\rm b}$ for three filaments which correspond to the ones shown in Figure 4.3 and labeled with "a", "b" and "c". We here assume the cylindrical skewer on the x-y plane shown in Figure 4.3 and rotate a skewer by angle θ around the center of the filament. The positional relation between the filamentary structures and the observed skewer is shown in Figure 4.6. In this case, we put the skewer on the same plane with the filament and the line-of-sight directions is on the x-y plane. The angle θ represents the separation between a filament and a skewer, and we choose $\theta = 0^\circ$ when the line-of-sight direction is parallel to the filament. We show the signals at present redshift with different angles for H I in Figure 4.8 and for ^{3}He II in Figure 4.9. In those figures, we show results for the different values of the spacial resolution; $r_s = 1$, 3, 5 and 10 Mpc/h, and the length of the skewer is adopted as $R = 100$ Mpc/h for all cases. We should note that these results have no contribution from the high-density region whose density contrast is $\delta \geq 200$, because our targets are the emission signals from the filamentary structures and the signals from the high-density regions such as galaxies are out of this work, also our assumptions are not valid anymore. On such a region, we have to take care of baryon physics or the stellar

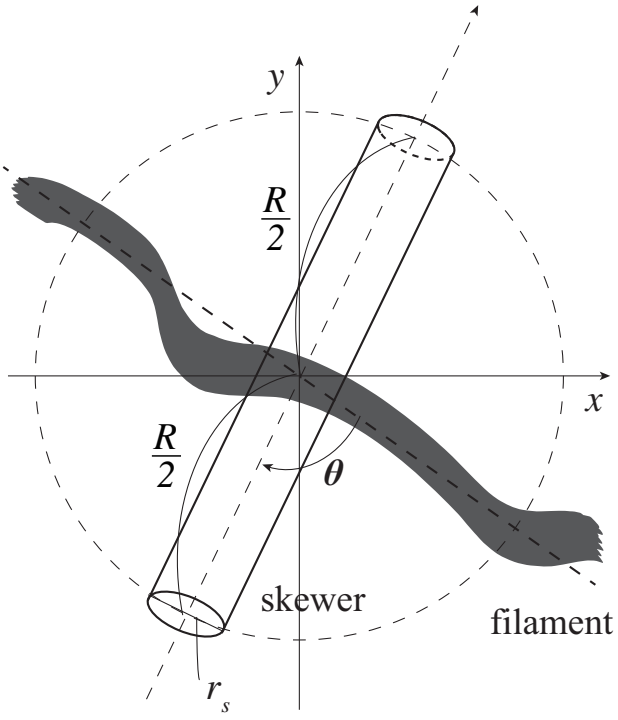

Figure 4.6: The positional relation between the filamentary structures and the observed skewer. θ represents the angle between the skewer and x-axis, R and r_s respectively represent the length along the line-of-sight and the spacial resolution of skewer. The center of the filament corresponds to the symbol shown in Figure 4.3 and the direction of the line-of-sight is fixed on the x-y plane.

production process of ^{3}He more carefully.

From Figure 4.8 and 4.9, we can see the angular dependence of the signal on each filamentary structure. The small spikes reflect the contributions from the other structures around the filament. Compared to the filament-a and -b, the filament-c has more widespread structure and this is the reason the angular dependence of the filament-c is feeble. If we observe the filament which extends along the line-of-sight, the amplitude of the emission signal can be expected $\delta T_{\rm b} \sim 10^{-5}$ K for H I and $\sim 10^{-8}$ K for ^{3}He II with spacial resolution of $r_s = 1$ Mpc$/h$, and these amplitudes are more than 10 times lager than the lowest cases.

The signal, of course, is expected to be higher, if we require the larger values of the spacial size for the skewer. However it highly depends on the specification of rivers or the survey strategy. In the following sections, we, discuss the prospects for observing the signals of the hyperfine transition.

4.3.3 Observational sensitivity

In this section, we summarize the sensitivity of the radio-telescope to estimate the prospects for observing the signals of H I and ^{3}He II. Here we assume some kind of different radio observations and the expressions for the noise of the radio telescope are adopted from (Furlanetto et al., 2006a).

The finest achievable resolution of the radio-telescope is called as "diffraction limit" and it depends on the largest dimension of the telescope $D_{\rm max}$ and the observing frequency λ as $\theta_{\rm D} = \lambda/D_{\rm max}$. Therefore the resolution is restricted by not only the specification of the telescope but also the observing frequency.

The sensitivity or the brightness temperature uncertainty of radio telescope can be often given as

$$\delta T_{\rm N}(\lambda) \simeq \frac{\lambda^2/\theta_{\rm s}^2}{A_{\rm tot}} \frac{T_{\rm sys}}{\sqrt{\Delta\nu T_{\rm obs}}}\,, \tag{4.16}$$

where λ is the observing frequency, $\theta_{\rm s}$ is the angular resolution, $T_{\rm sys}$ is the systematic temperature, $A_{\rm tot}$ is the total collecting area, $\Delta\nu$ is the band width, and $T_{\rm obs}$ is the integration time of the observation.

At low-frequencies the sky is so bright and the synchrotron radiation from the Milky Way dominates the sky around $\sim$ 150 MHz where is relevant to the EoR of H I. Contrary the sky at high-frequencies gains a great advantage, and can keep the systematics from foreground quiet low. From some empirical rules at high-latitude, the temperature in "quiet" portions of the sky is given as v

$$T_{\rm sky} \sim 180 \left(\frac{\nu}{180{\rm MHz}}\right)^{-2.6} {\rm K}\,. \tag{4.17}$$

We here assume that the foreground is the dominant component for the systematics and take into account only the sky temperature as the systematic temperature; i.e., $T_{\rm sys} \simeq T_{\rm sky}$. Adopting the sky temperature given in Eq. (4.17), the noise of the interferometer can be written from Eq. (4.16);

$$\delta T_{\rm N}^{\rm sky}(\nu) \simeq 5.0 \left(\frac{10^5\ {\rm m}^2}{A_{\rm tot}}\right) \left(\frac{1'}{\Delta\theta}\right)^2 \left(\frac{1+z}{1}\right)^{4.6} \left(\frac{1420\,{\rm MHz}}{\nu_0}\right)^{4.6} \left(\frac{\rm MHz}{\Delta\nu}\frac{100\ {\rm hr}}{T_{\rm obs}}\right)^{1/2} \mu{\rm K}\,, \tag{4.18}$$

where ν is the targeting frequency, $\Delta\theta$ is the beam angular resolution, and ν_0 represents the rest frame frequency of the observed hyperfine transition; i.e., ν_0=1420 MHz for H I or ν_0=8667 MHz for ^{3}He II.

Although the observation with high-frequencies at low-redshifts has the advantage to achieve high-sensitivity due to less contaminants from the foreground, the receiver noise $T_{\rm rec}$ dominates the system temperature. The noise due to the receiver noise can be written from Eq. (4.16);

$$\delta T_{\rm N}^{\rm rec} \simeq 23.9 \left(\frac{T_{\rm rec}}{30\ {\rm K}}\right) \left(\frac{10^5\ {\rm m}^2}{A_{\rm tot}}\right) \left(\frac{1'}{\Delta\theta}\right)^2 \left(\frac{1+z}{1}\right)^{2.0} \left(\frac{1420\,{\rm MHz}}{\nu_0}\right)^{2.0} \left(\frac{\rm MHz}{\Delta\nu}\frac{100\ {\rm hr}}{T_{\rm obs}}\right)^{1/2} \mu{\rm K}\,, \tag{4.19}$$

where T_{rec} is the receiver noise. Therefore, we should take into account the contribution from the receiver noise for the reasonable estimation; $T_{\rm sys} \equiv T_{\rm sky} + T_{\rm rec}$, and it should be the crucial aspects for the observation of ^{3}He II.

Then we define the total noise combining Eqs. (4.18) and (4.19) as

$$\delta T_{\rm N} = \left(\delta T_{\rm N}^{\rm sky} + \delta T_{\rm N}^{\rm rec}\right) \times \begin{cases} 1 & \text{(single dish)} \\ 1/\sqrt{N_{\rm B}} & \text{(interferometer)} \end{cases} \tag{4.20}$$

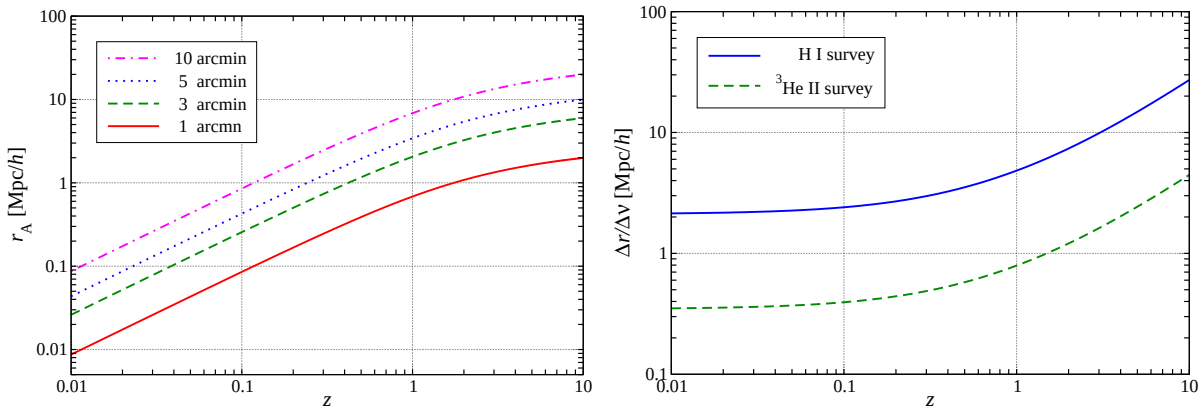

Figure 4.7: (Left) The spacial size $r_{\rm A}$ with different values of the angular size θ_s as a function of redshift. (Right) The relationship between the frequency band width $\Delta\nu$ and the spacial length along the line-of-sight Δr for the H I (solid-line) and the ^{3}He II (dashed-line) observations.

where $N_{\rm B} = N_{\rm dish}(N_{\rm dish}-1)/2$ is the number of pair-wise correlations or base lines, and $N_{\rm dish}$ is the number of telescopes for the interferometer. The noise for the interferometer can be reduced by the factor of $1/\sqrt{N_{\rm B}}$.

4.3.4 Spacial resolution of Observations

The spacial size $r_{\rm A}$ and the depth along the line-of-sight Δr for a observation depend on the cosmological model. We here summarize them and their relationship with the survey parameters.

When the angular resolution θ_s is given, the spacial size can be determined by

$$r_{\rm A} = \theta_s \chi(z)\,, \tag{4.21}$$

where $\chi(z)$ is the comoving distance to the observed source at redshift z. On the other hand, the depth along the line-of-sight is determined by the frequency band width $\Delta\nu$ and the relationship between them is given by

$$\frac{\Delta r}{\Delta\nu} \simeq \frac{1+z}{\nu_0}\frac{c}{H(a)}\,, \tag{4.22}$$

where $\Delta\nu$ is the frequency band width and ν_0 is the restframe frequency of the observed source. Therefore this relationship differs between the H I and ^{3}He II observations.

We show the results with our cosmological model as a function of redshift in Figure 4.7.

We consider some on-going or future radio-telescopes, which are Green Bank Telescope (GBT), Arecibo Radio Telescope (Arecibo), Five-hundred-meter Aperture Spherical Telescope (FAST), Giant Metrewave Radio Telescope (GMRT), Expanded VLA (EVLA), MeerKAT and Square-Kilometer Array (SKA), and we show the characteristic parameters for these radio telescope in Table 4.2. We should note that the operating range of GMRT does not have enough frequency range to observe the signal of ^{3}He II at low-redshifts and its achievable redshift range is $z > 4.7$. The operating range of FAST also does not reach the restframe frequency of ^{3}He II, however the

Telescope	$R_{\rm dish}$ [m]	$N_{\rm dish}$	$A_{\rm tot}$ [m^2]	$\epsilon_{\rm ap}$	Operating range	$D_{\rm max}$ [km]
Single dish						
GBT	100	—	7,850·$\epsilon_{\rm ap}$	0.7	100 MHz - 116 GHz	0.1
Arecibo	305	—	73,000·$\epsilon_{\rm ap}$	0.8	47 MHz - 10 GHz	0.3
FAST	500	—	200,000	1	70 MHz - 3 GHz	0.5
Interferometer						
EVLA	25	27	13,300	—	1,000 MHz - 50 GHz	1 - 36
GMRT	45	30	60,750	—	50 MHz - 1.5 GHz	25
MeerKAT (phase 2)	13.5	64	9,160	—	580 MHz - 14.5 GHz	20
SKA (phase 2)	15	1,500	300,000	—	70 MHz - 10 GHz	5c

Table 4.2: The characteristic parameters for the specification of the radio-telescopes. GBT and Arecibo are the single dish telescopes and the others are the radio-interferometers. $R_{\rm dish}$ is the diameter of a dish for one telescope, $N_{\rm dish}$ is the number of telescopes, and $A_{\rm tot}$ is the effective total collecting area of the telescope. The parameter $\epsilon_{\rm ap}$ represents the aperture efficiency of the single dish telescope. $D_{\rm max}$ is the maximum base line length of the telescope; for EVLA the value depends on the configuration of the telescopes, and for SKA we take the extent of compact core.

future updating may allow to observe up to 8 GHz (Nan et al., 2011).

We show the emission signals and the sensitivity curves for the observation of H I and ^{3}He II in Figure 4.10 and 4.11, respectively. The signals are adopted the same ones shown in the right panel of Figure 4.2, and we assume the $T_{\rm rec} = 30$ K of the receiver noise for all cases. We should note that the sensitivity of EVLA and FAST are almost same amplitude in our assumption and we plot only that of FAST for the illustrative purpose. We compare three types of observation with different angular resolutions; $\Delta\theta$ =30, 10 and 1 arcmin. The solid curves represent the sensitivity of each telescope, and we here take into account both the sky temperature and the receiver noise for the system temperature. Then, we assume 100 hours of integration time and $\Delta\nu$ =30 MHz of frequency band width for H I and $\Delta\nu$ =200 MHz for ^{3}He II, respectively. These values for the band width correspond to ~ 100 Mpc/h depth along the line-of-sight around $z = 0.5$.

As shown in Figure 4.4 and 4.5, the emission signal is expected to increase at higher redshifts for both H I and ^{3}He II. In Figure 4.12 and Figure 4.13, we show the signal from each filamentary structure at various redshifts, $z = (0, 0.5, 1, 2, 4)$, for H I and ^{3}He II, respectively. We also plot the sensitivity curves for each survey in the same panels. The way to estimate the signal is same as that of shown in Figure 4.8 and 4.9, and we consider observing a filament from various angles. Each data point shows the range of signal between maximum and minimum amplitudes, and the symbol represents the average value.

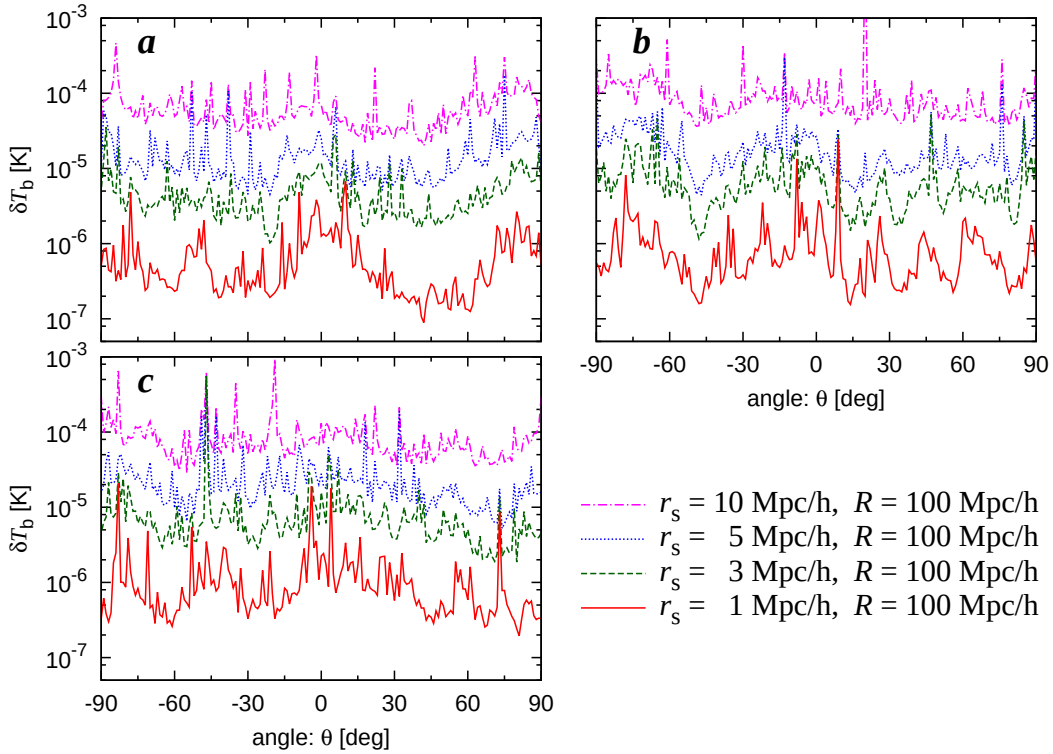

Figure 4.8: The signal of H I from the filamentary structures at $z = 0$. The angle θ represents the angular size between a filament and the line-of-sight, r_s and R represent the spacial size and the line-of-sight width for a skewer. The different color lines show the different values of r_s; which are 10 Mpc/h (magenta), 5 Mpc/h (blue), 3 Mpc/h (green) and 1 Mpc/h (red), and the width is fixed to be $R = 100$ Mpc/h for all cases. The positional relation between a filament and a skewer is pictured in Figure 4.6. The label "a", "b" and "c" correspond to the filaments shown in Figure 4.3.

4.4 Discussion

4.4.1 Prospect of observation

We here discuss the prospects for detecting the emission signals of H I and ^{3}He II with the on-going or future radio-telescopes.

For the signals of H I, the amplitude of signal at z =0 to 1 is $\delta T_b \sim 10^{-6}$ to 10^{-4} K with $r_s = 3$ Mpc/h from Figure 4.12. The angular resolution of $\Delta\theta = 10$ arcmin corresponds to $\sim$ 3.9 Mpc/h spacial width at $z = 0.5$ and it seems that these specifications can be enough for our purpose to observe the filamentary structures. Actually, the beam size of the present receiver for this frequency range is adequate; g.e. 9 arcmin for GBT and $\sim$ 3.5 arcmin for Arecibo. Therefore we have possibility for detecting the H I signal even by present instruments. We here assume 100 hours integration time, but GMRT, EVLA and future telescopes may have enough sensitivity to detect the signal with shorter integration time.

On the other hand, compared to the signal of H I, the signal of ^{3}He II is so weak and the

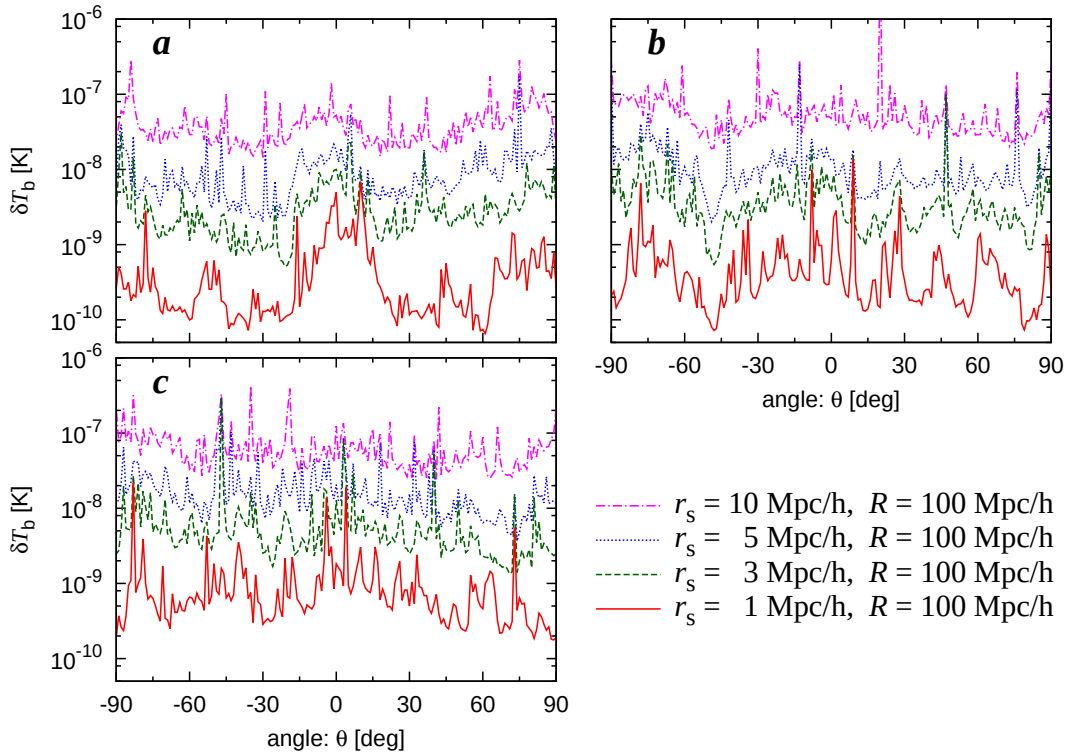

Figure 4.9: Same as Figure 4.8, but for the signals of ^{3}He II.

amplitude is less than the order of micro-kelvin at $z = 0$ to 1. When we assume a skewer with $r_s = 1$ Mpc/h and $R = 100$ Mpc/h, the amplitude is $\delta T_\mathrm{b} \sim 10^{-10}$ to 10^{-8} K at $z = 0.5$ from Figure 4.13. Such level of sensitivity can be achieve by the future telescopes such as MeerKAT and SKA. The amplitude of noise due to the sky temperature also can be lower than that of H I under the favor of high-observing frequency at restframe frequency of 8.6 GHz for ^{3}He II hyperfine transition. However the system temperature is dominated by the receiver noise rather than the sky temperature at high-frequency. After all, the amplitude of noise for the ^{3}He II observation is comparable to one of the H I observation.

The other crucial aspect is the narrow beam size at the high-frequencies. Generally the beam size of the receiver at high-frequencies is smaller than at low-frequencies. Therefore the observing area becomes so tiny; g.e. 1.7 arcmin for GBT and 0.7 arcmin for Arecibo, and the angular size is $r_s \sim 0.3$ Mpc/h for Arecibo at $z = 0.5$. In general, the field-of-view for the single dish telescope corresponds to the beam size, and the observing area is so tiny. If we require $r_s = 1$ Mpc/h angular size with Arecibo, we have to observe $z \geq 2$. From this aspect, the single dish telescope seems unsuitable for the detection of the ^{3}He II signal at low-redshifts. Wheres, the field-of-view for the interferometer is given by the dish size of a small telescope; $\theta_\mathrm{FoV} \simeq \lambda / R_\mathrm{dish}$. Therefore the interferometer has a larger field-of-view than the single dish telescopes, and we can get the larger skewer, e.g. $\theta_\mathrm{FoV} \sim 4$ arcmin for EVLA and $\theta_\mathrm{FoV} \sim 8$ arcmin for MeerKAT. The future telescopes such as MeerKAT and SKA have enough sensitivity for detecting the ^{3}He II signal around these redshifts.

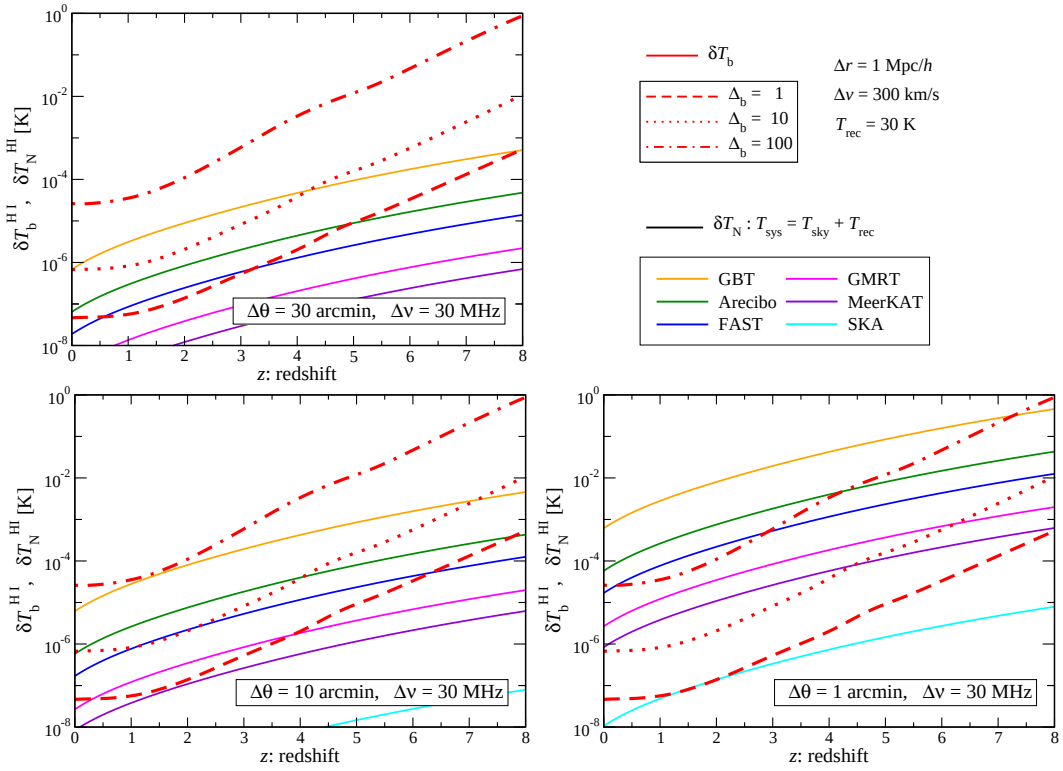

Figure 4.10: The signal and noise spectrum for the hyperfine transition of H I as a function of redshift. The signal represents the differential brightness temperature of H I (red-lines), which is same as shown in the right panel of Figure 4.2. The noise spectrum is adopted for the observation at the rest frame frequency of 1.4 GHz with GBT (orange), Arecibo (green), EVLA (violet), FAST (blue), MeerKAT(violet) and SKA (cyan). The solid curves represent the noise taking into account only the sky temperature, and the dashed curves with same color represent the noise taking into account both the sky temperature and the receiver noise of $T_{\rm rec} = 30$ K. The three panels show the difference of the noise spectra with the different values of the spacial resolution $\Delta\theta$ for the observation; we adopt the values to be $\Delta\theta = 30$ arcmin (Top-Left), $\Delta\theta = 10$ arcmin (Bottom-Left), and $\Delta\theta = 1$ arcmin (Bottom-Right). The frequency band width of $\Delta\nu = 30$ MHz, which corresponds to $\sim$100 Mpc/h width along the line-of-sight at $z = 0.5$, is adopted for all cases. We assume the 100 hours of integration time for all telescopes.

Furthermore, at higher redshift, $z \geq 2$, we still have possibility for detecting the ^{3}He II signal with present instruments such as Arecibo and EVLA. The angular size increase at higher redshifts, and the observing frequency decrease. The beam size of Arecibo reaches 3 arcmin at $z = 4$ and it corresponds to the spacial size of $r_s \sim 5$. Around these redshifts, we can not use the galaxy catalogs of the optical galaxy redshift survey, but the results from the observation of Ly-α can be adopted as tracers to find the high-density regions.

We should note that GMRT seems one of the best telescope in the on-going instruments for the observation of ^{3}He II, however its operating frequency range is unfortunately less than 1.5 GHz and we can not use GMRT for the prove of ^{3}He II at $z < 4.7$. Instead of GMRT, the Arecibo telescope can be prove even at low-redshifts with similar sensitivity to GMRT.

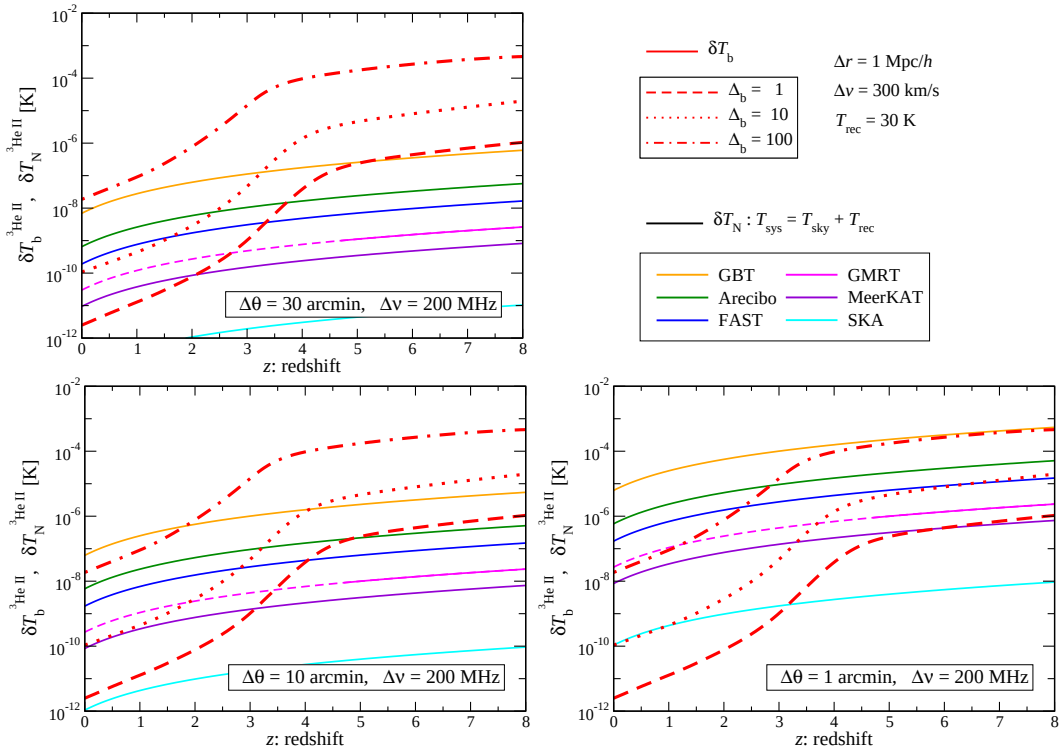

Figure 4.11: Same as the right panel in Figure 4.10, except the signals are the differential brightness temperature of ^{3}He II and the noise spectra are adopted for the observation at the rest frame frequency of 8.7 GHz. The frequency band width of $\Delta\nu = 200$ MHz, which corresponds to ∼100 Mpc/h width along the line-of-sight at $z = 0.5$, is adopted for all cases.

4.4.2 Systematics

Specification of Receiver

One of the benefits of the observation with high-frequencies is less contaminants from the foreground, and the sky temperature achieves less than a few K around a few GHz observation. However, the systematics is dominated by the receiver noise rather than the sky temperature on the observation with high-frequencies. In Figure 4.10 and 4.11, we also show the sensitivity of each telescope taking into account the receiver noise for systematics. The dashed-curves correspond to the noise taking into account both the sky temperature and the receiver noise for the systematic temperature; i.e. $T_{\rm sys} = T_{\rm sky} + T_{\rm rec}$, and $T_{\rm rec} = 30$ K of receiver noise is assumed here.

On the sensitivities of H I, the contribution from the receiver noise dominates the systematics at low-redshifts. The receiver of Arecibo around 1.4 GHz range can achieve the system temperature of $\sim$ 30 K. However the sensitivity of Arecibo is still enough to detect the signals at low-redshifts, if we assume the angular resolution with $\Delta\theta \geq 30$ arcmin and enough integration time with $T_{\rm obs} \sim 100$ hours. On the other hand, the contribution from the receiver noise on the observation of ^{3}He II is significant, and the systematics should be set by the receiver noise rather than the sky temperature. Actually the receivers of Arecibo at high-frequency range can achieve

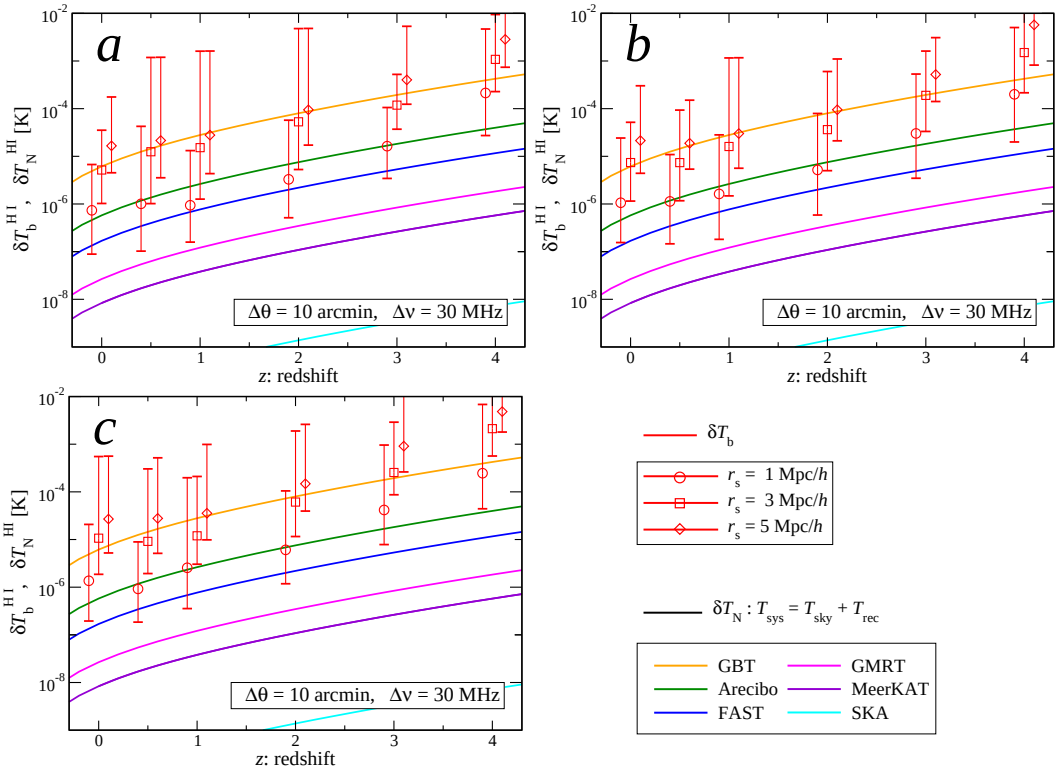

Figure 4.12: The redshift evolution of the H I signals from the filamentary structures labeled as a, b and c, and we show the results at $z = 0.5$, 1, 2 and 4. Each data point represents the range of signal between maximum and minimum amplitudes, and the symbol represents the average value. The different symbols show respectively $r_s = 1$ Mpc/h(circle), $r_s = 3$ Mpc/h(square) and $r_s = 5$ Mpc/h(diamond), and $R = 100$ Mpc/h is adopted for all cases.

the system temperature $\sim$ 30 K and the receiver of GBT also has almost same level of the system temperature. Therefore one of the key point for the detection of the ^{3}He II signal at low-redshifts is to make the receiver noise low.

^{3}He production around star forming region

In addtion to the primordial production predicted by BBN, ^{3}He should be produced in stars (Goldwire and Goss, 1967; Olive et al., 1995; Rood et al., 1998). Therefore the stellar production of ^{3}He contaminates the measurements of the primordial abundance of ^{3}He and estimation of the missing baryon components. Moreover the precise measurement of the primordial ^{3}He abundance requires the detailed modeling of the stellar production. However, from the observations of intergalactic H II regions, a significant excess against the primordial abundance is not observed (Balser et al., 2007; Eggleton et al., 2008), and the measurement of ^{3}He in the intergalactic regions would be less contaminated by the stellar production of ^{3}He.

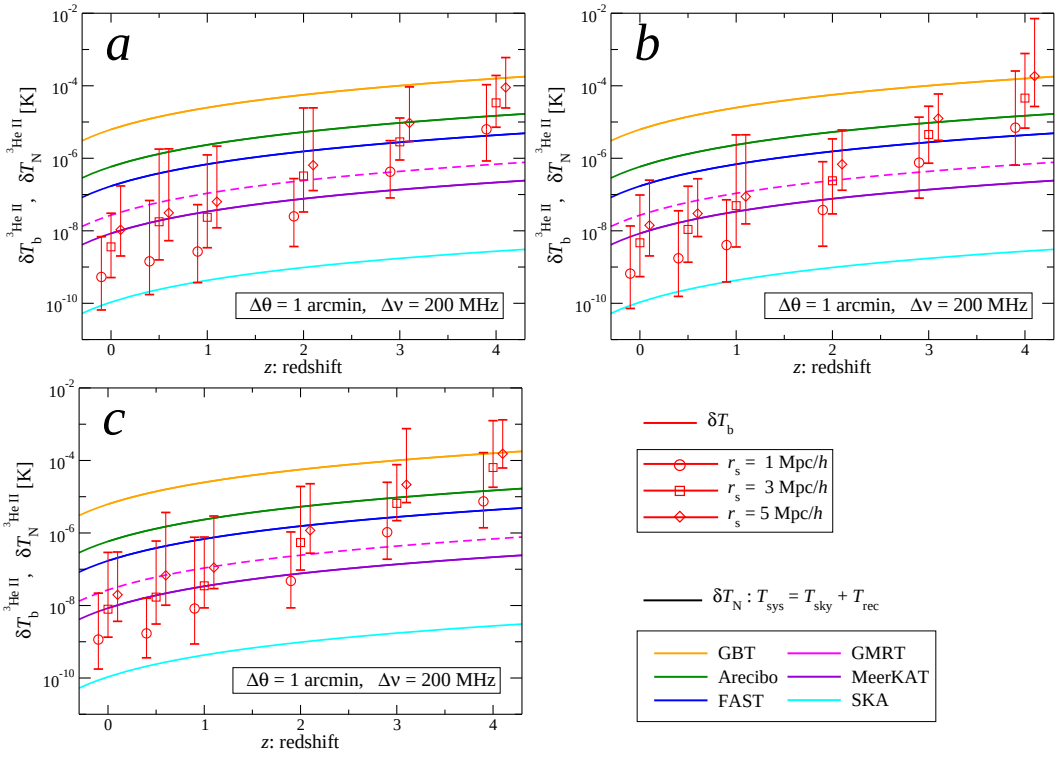

Figure 4.13: Same as Figure 4.12, but for the signal and sensitivity curves of ^{3}He II.

Contaminants from other lines

The contaminants from different lines for the absorption system of ^{3}He II are discussed in (McQuinn and Switzer, 2009) in detail, and we consider the contaminants for the ^{3}He II signal at low-redshifts following them. The abundance of ^{3}He II is quiet small compared to the universal abundance of some atoms, and the different lines can cause the systematics on the detection of signals of ^{3}He II at low-redshifts. The cosmological redshifted signals are allowed to fall into the lower frequency even though the higher frequency transitions than the observing range of H I or ^{3}He II at low-redshifts.

For the hyperfine transition from metals, the most anxious line is the 4.2 GHz transition of ^{14}NV. While it is subdominant absorber to ^{3}He, the redshifted emission signal of ^{14}NV may contaminates the diffused background at $\sim$ 2 GHz at $\delta T_{\rm b} \sim 10^{-7}$ K-level with the relative abundance to Solar $\langle W \rangle = 0.1$ (Syunyaev and Churazov, 1984). However the signal of ^{3}He II at such frequency is $\delta T_{\rm b} \sim 10^{-6}$ and the contaminants from the metals may be subdominant to both H I and ^{3}He II signals.

For the radio recombination lines (RRLs), it has been considered as a possible contaminant for the H I signal (Oh and Mack, 2003). If the RRL falls within a frequency channel of observing frequency band width $\Delta\nu$, it affects the signal (Shaver, 1975). However the RRL emission may also be subdominant and unimportant for the signal of ^{3}He II.

For molecular lines, the molecules rotation lines are negligible though the rotational transition

rates of molecules are many orders of magnitude higher than for ^{3}He II. This is because that the lowest lines of diatomic molecules rotation lines lie at high-frequency $\geq$ 50 GHz, and their abundance is negligible at redshifts which the signals of 1−2 GHz band come from. On the other hand, the redshifted signal from molecular hyperfine or rotational modes of polyatomic molecules may be worrisome. However the abundance of polyatomic molecules is many orders of magnitudes lower than ^{3}He and their emission signals are also unimportant. However the bright maser emission of 1.7 GHz OH hyperfine transitions are a possible contaminant of the H I signal, while it is unimportant for the ^{3}He II signal at low-redshifts.

For the fine structure lines, the $2P_{3/2} \rightarrow 2P_{1/2}$ transition at 10.9 GHz can appear in absorption in H II regions or in H I regions under some conditions pumping the $2S$ state. In galactic H II regions, collisions and recombinations work effectively, and the $2P_{3/2} \rightarrow 2P_{1/2}$ transition appears in absorption. On the other hand, the mechanism pumping $2S$ state is inefficient Dijkstra et al. (2008) in H I regions, and it appears in emission. Therefore it is a possible contaminants for the ^{3}He II signals, but the contributions to the signal at $\nu \geq 2$ GHz band may be unimportant because the most of hydrogen is ionized at low-redshifts.

4.4.3 Survey strategy

Considering to try observing these signals from the intergalactic filament structures actually, the strategy for the observing area and the targeting frequency may become the key for the detection. The recent galaxy redshift survey such as SDSS has revealed the vast area of universe at low-redshifts, and its galaxy catalog data can be provide the fruitful information to take aim at the targeting area, though it is not suitable for the high-redshifts. This is also the benefit for the observation at low-redshifts.

Statistical signals

Sometimes, the statistical signals allow us to detect the signals with high-significance even though the sensitivity of the observation is poor. The cross-correlations with the other observables which have high-sensitivity help extracting the faint signals of hyperfine transition.

Actually some works observe the emission signals of H I from IGM at low-redshifts; (Chang et al., 2010) detected the aggregate 21-cm glow around $z \sim 0.8$ at a significance of $\sim 4\sigma$ by cross correlating intensity mapping data from GBT with the DEEP2 galaxy survey (Davis et al., 2001), and (Masui et al., 2012) improved (Chang et al., 2010) by cross correlating new intensity mapping data by GBT with the WiggleZ Dark Energy Survey (Drinkwater et al., 2010).

Therefore we can apply the intensity mapping for the signal of ^{3}He II and the statistical signal helps to detect the signal of ^{3}He II with higher confidence level than the direct observation. However we keep this topics as a future work.

4.5 Summary

We have also discussed whether current telescopes can reach the sensitivities required for observing H I and ^{3}He II emission from our filament models. Despite the low signal of H I, we have shown in this paper that these levels of sensitivity can be reached even by the present instruments, such as GBT, EVLA, and Arecibo with 100 hours of integration time. The ^{3}He II signal is much weaker than that of H I and is very hard to detect with present instruments. However, we show that detecting both H I and ^{3}He II from large scale filaments is possible with future telescopes, such as the full MeerKAT and SKA, given a reasonable amount of integration time.

At higher redshifts one benefits from larger signal, however, other issues start to become important. Most importantly, the beam size at higher frequencies becomes smaller, along with the field of view. The smaller beam size means that more distant filaments will not fill the beam, leading to a smaller detected signal. The field of view issue will limit the size of the filaments we can detect, especially if the filament is mostly elongated perpendicular to the line-of-sight. However, as we show the ^{3}He II signal around $z \sim 4$ is still in principle detectable even with the present instrument such as GMRT and Arecibo.

Obviously, one of the benefits of observing the two lines in the same filament is to give us a handle on the UV/X-ray background. In this work, we have adopted a single model for the background, but in future work this aspect will be explored in more detail.

In this chapter we focus only on the direct detection of these signals. Less direct detections, e.g., statistical methods or cross-correlation approaches are also possible and, in some cases of H I been discussed by other authors (Chang et al., 2008). This is clearly an exciting route that promise to yield results in the foreseeable future.

It should be mentioned that we have not considered a number of effects that might make it more difficult to observe the signal, e.g., foregrounds, contamination from recombination lines, meta lines, etc. This will be dealt with in a future publication.

Chapter 5

Constraints on the isocurvature modes by the 21cm line from minihaloes

We investigate the effects of isocurvature perturbations on the 21cm radiation from minihaloes (MHs) at high redshifts and examine constraints on the isocurvature amplitude and power spectrum using the next generation of radio telescopes such as the Square Kilometre Array. We find that there is a realistic prospect of observing the isocurvature imprints in the 21cm emission from MHs, but only if the isocurvature spectral index is close to 3 (*i.e.* the spectrum is blue). When the isocurvature fraction increases beyond $\sim 10\%$ of the adiabatic component, we observe an unexpected decline in the 21cm fluctuations from small-mass MHs, which can be explained by the incorporation small MHs into larger haloes. We perform a detailed Fisher-matrix analysis, and conclude that the combination of future CMB and 21cm experiments (such as CMBPol and the Fast-Fourier-Transform Telescope) is ideal in constraining the isocurvature parameters, but will stop short of distinguishing between CDM and baryon types of isocurvature perturbations, unless the isocurvature fraction is large and the spectrum is blue.

5.1 Introduction

Recent measurements of the anisotropies in the cosmic microwave background (CMB) by the *Planck* satellite have placed constraints of unprecedented accuracy on the amplitude of the primordial density fluctuations (Planck Collaboration et al., 2013a,c). Planck also revealed that these fluctuations are consistent with having originated from *adiabatic* initial conditions, characterized by the constancy of the ratios of density contrasts of various particle species in the early Universe (see Kodama and Sasaki (1984); Bardeen (1980) for reviews). This is in agreement with previous CMB measurements by the *WMAP* satellite (Hinshaw et al., 2013; Bennett et al., 2013). On the other hand, if the aforementioned ratios of density contrasts are *not* constant, the fluctuations are said to be generated from *isocurvature* initial conditions, of which there are four types, namely, the cold-dark-matter (CDM), baryon, neutrino-density and neutrino-velocity

isocurvature perturbations (Bucher et al., 2000). Constraints from Planck limit any isocurvature contributions to the CMB temperature anisotropies to less than ~ 10 percent.

The simplest model of inflation involving a single, slowly rolling scalar field predicts that density fluctuations are generated from purely adiabatic initial conditions. Hence, the detection of any isocurvature contribution would be a window to novel physical mechanisms in the inflationary era. Such mechanisms include the curvaton mechanism (Lazarides et al., 2004; Langlois and Vernizzi, 2004; Moroi et al., 2005; Moroi and Takahashi, 2005; Ichikawa et al., 2008a; Langlois et al., 2008), the axion and gravitino CDM (Rajagopal et al., 1991; Covi et al., 2001, 2002; Brandenburg and Steffen, 2004) and the modulated reheating scenarios (Dvali et al., 2004; Kofman, 2003; Ichikawa et al., 2008b; Takahashi et al., 2009; Takahashi et al., 2009) as well as various combinations of such scenarios. In most of these models, a large isocurvature fraction can be produced at the expense of the introduction of a few additional parameters (Moroi and Takahashi, 2002; Lyth et al., 2003; Lyth and Wands, 2003; Beltran, 2008; Moroi and Takahashi, 2009; Takahashi et al., 2009).

According to our current understanding of cosmology, inflation-stretched primordial quantum fluctuations subsequently grow via gravitational instability into the observed cosmic structures. One of the earliest cosmic structures to form were minihaloes (MHs), which are virialized haloes of dark and baryonic matter with typical mass $10^4 - 10^8\ M_\odot$, and temperature $\lesssim 10^4$ K, at very high redshift ($z \sim 6 - 20$). Minihaloes typically host a high density of neutral hydrogen, which can be detected by the 21cm absorption/emission line due to the transition of the hydrogen atom from a parallel to anti-parallel spin state. MHs are typically at such high temperatures that their 21cm signal appears in emission with respect to the CMB (Iliev et al., 2002). The 21cm signals from MHs give us information on the small-scale density fluctuations at high redshifts, and their detection will therefore lead to a deeper understanding of small-scale physics during the earliest structure-formation epoch.

The 21cm signal from MHs has previously been studied by Chongchitnan and Silk (2012), who showed that the 21cm emissions from MHs are a sensitive probe of primordial non-Gaussianity, due to a strong dependence of the MH number density and bias on the amplitude of non-Gaussianity. Tashiro et al. (2013) calculated the 21cm fluctuations due to MHs in cosmic wakes produced by cosmic strings.

In this paper, we present a new probe of isocurvature fluctuations using the 21cm signal from MHs. We will show that the fluctuations in the 21cm emission from MHs are a viable probe of isocurvature fluctuations. We also give forecasts on the isocurvature fraction and spectral index using the next generation of large arrays of radio interferometers, which are expected to measure the cosmic 21cm signals over a wide range of redshifts, from the cosmic Dark Ages ($z \sim 30 - 50$) down to the Epoch of Reionization (EoR) at $z \sim 6$. Such radio surveys include: the Low-Frequency Array (LOFAR*), the Murchion Widefield Array (MWA†), and the Giant Metrewave Radio Telescope (GMRT‡), all of which focus on $6 \lesssim z \lesssim 30$, as well as more ambitious future

*http://www.lofar.org
†http://www.mwatelescope.org
‡http://gmrt.ncra.tifr.res.in

arrays such as the Square Kilometre Array (SKA[§]), and the Fast Fourier Transform Telescope (FFTT) (Tegmark and Zaldarriaga, 2009), which can probe the radio Universe at $z \gtrsim 30$.

There have only been a handful of works exploring the link between 21cm cosmology and isocurvature perturbations: Barkana and Loeb (2005) and Lewis and Challinor (2007) discussed the prospects for differentiating between the CDM and baryon isocurvature fluctuations using 21cm signals. Further work by Kawasaki et al. (2011) showed that 21cm surveys can effectively probe the difference between CDM and baryon isocurvature fluctuations if the spectrum of isocurvature perturbations is strongly blue tilted (we revisit this claim later). Gordon and Pritchard (2009) investigated the constraints on isocurvature modes from 21cm observations, focusing on the so-called compensated isocurvature perturbations.

This chapter is organized as follows: we summarize the 21cm radiation from minihaloes and its sensitivity to the presence of isocurvature modes in Sec. 5.2. The effects of isocurvature modes on the *fluctuations* of this signal are explained in Sec. 5.3. Forecasts on the constraints of isocurvature parameters from future radio surveys are discussed in Sec. 5.4 and 5.5. Finally, Sec. 5.6 and 5.7 contain further discussions and a summary of our main conclusions.

Throughout this work, we assume a flat Universe and adopt the cosmological parameters from Planck (Planck Collaboration et al., 2013b).

5.2 21cm emission line from minihaloes

Whether the 21cm line appears in emission or absorption signal against the CMB temperature depends on the spin temperature. The spin temperature is determined by the balance between collisional and radiative excitation or de-excitation of spin states by atoms, electrons and photons. These processes couple the spin temperature to the gas field and radiation field as (Field, 1958)

$$T_{\rm s} = \frac{T_{\rm CMB} + y_\alpha T_\alpha + y_{\rm c} T_{\rm k}}{1 + y_\alpha + y_{\rm c}} \ , \tag{5.1}$$

where T_α is the color temperature of the Lyα photons, $T_{\rm k}$ is the kinetic temperature of gas, y_α and $y_{\rm c}$ are the radiative and collisional excitation efficiencies (Madau et al., 1997). We now assume that bright UV and X-ray sources have not formed yet or the MHs are isolated from such sources, then we neglect the radiative coupling and can set $y_\alpha = 0$.

The 21cm signal from a halo depends on the profiles of the density, the velocity and the temperature in a halo. We adopt the model called as a truncated isothermal sphere (TIS) (Shapiro et al., 1999; Iliev and Shapiro, 2001), where a MH of a given mass is modeled with radius r_t, temperature $T_{\rm k}$, dark matter density profile $\rho(r)$ and velocity dispersion σ_V.

The MHs host the high density of neutral hydrogen and the gas temperature inside them is heated enough to decouple from the CMB temperature. Therefore even a single minihalo can

[§]http://www.skatelescope.org

produce an observable 21cm signal. The observed brightness temperature along a line-of-sight through a halo at comoving distance r from the center of the halo is given by

$$T_{\rm b}(r) = T_{\rm CMB}(z)e^{-\tau(r)} + \int_0^{\tau(r)} T_{\rm s}e^{-\tau'}d\tau' \ , \tag{5.2}$$

where $\tau(r)$ is the total optical depth of neutral hydrogen to photons at frequency ν through a halo along a line-of-sight from the center of a halo, and can be expressed as (Furlanetto and Loeb, 2002)

$$\tau(\nu) = \frac{3c^2A_{10}T_*}{32\pi\nu_0^2}\int_{-\infty}^{\infty}\frac{n_{\rm HI}(\ell)\phi(\nu,\ell)}{T_{\rm s}(\ell)}dR \ , \tag{5.3}$$

where R and ℓ are radial comoving distances satisfying $\ell^2 = R^2+(\alpha r_t)^2$; α is the impact parameter in unit of r_t, and $n_{\rm HI}$ is the number density of neutral hydrogen. $\phi(\nu)$ is the intrinsic line profile modeled as a Doppler-broadened given by

$$\phi(\nu) = \frac{1}{\Delta\nu\sqrt{\pi}}\exp\left[-\left(\frac{\nu-\nu_0}{\Delta\nu}\right)^2\right] \ , \tag{5.4}$$

with $\Delta\nu = (\nu_0/c)\sqrt{2k_{\rm B}T_{\rm k}/m_{\rm H}}$.

When the line profile is unbroadened; $\phi(\nu) = \delta(\nu-\nu_0)$, the optical depth corresponds to that of the IGM at redshift z and can be given by (Madau et al., 1997)

$$\tau_{\rm IGM}(\nu;z) = \frac{3c^3A_{10}T_*n_{\rm HI}(z)}{32\pi\nu_0^3T_{\rm s}(z)H(z)} \ , \tag{5.5}$$

where A_{10} and ν_{10} are the spontaneous decay rate and the restframe frequency for the 21cm transition, T_* is the equivalent temperature defined as $T_* \equiv h_{\rm p}\nu_{10}/k_{\rm B}$. Then we can rewrite the total optical depth as

$$\tau(\nu,R) = \tau_{\rm IGM}(\nu) + \frac{3c^2A_{10}T_*}{32\pi\nu_0^2}\int_{-\infty}^{R}\frac{n_{\rm HI}(\ell')\phi(\nu,\ell')}{T_{\rm s}(\ell')}dR' \ . \tag{5.6}$$

The first and second terms respectively represent the contribution from IGM and a halo.

The observed 21cm brightness temperature is expressed as the differential brightness temperature respect to the CMB and given by

$$\delta T_{\rm b} = \frac{1}{1+z}\left(\frac{\int dAT_{\rm b}(r)}{A} - T_{\rm CMB}(z)\right) \ , \tag{5.7}$$

where $T_{\rm b}$ is averaged over the halo cross-section $A = \pi r_t^2$. Then the mean 21cm emission from an ensemble of MHs in the mass range $[M_{\rm min},M_{\rm max}]$ is given by (Iliev et al., 2002)

$$\overline{\delta T_{\rm b}} = \frac{c(1+z)^4}{\nu_0 H(z)}\int_{M_{\rm min}}^{M_{\rm max}}\Delta\nu_{\rm eff}\delta T_{\rm b}(M)A\frac{dn}{dM}dM \ , \tag{5.8}$$

where $\nu_{\rm eff} = [\phi(\nu_0)(1+z)]^{-1}$ is the effective redshifted line-width, and we adopt $M_{\rm max}$ corresponding to the virial temperature of 10^4 K and $M_{\rm min}$ corresponding to the Jeans mass $M_{\rm J}$, respectively.

The rms fluctuations in the 21cm emission for a pencil-beam survey with frequency width $\Delta\nu$ and angular size $\Delta\theta$ is given by

$$\langle \delta T_{\rm b}^2 \rangle^{1/2} = \sigma_{\rm p}(z, \Delta\nu, \Delta\theta)\beta(z)\overline{\delta T_{\rm b}}(z) \ , \tag{5.9}$$

where $\sigma_{\rm p}$ is the variance in a cylinder and β is the flux weighted average of bias.

The variance in a cylinder is given by

$$\sigma_{\rm p}(z, \Delta\nu, \Delta\theta) = 2\pi \int \frac{dk_z}{k_z} \left[\frac{k_z^3 P(k_z)}{2\pi^2}\right] \int_{1/R}^{\infty} dk_r \left[\frac{2}{k_r R(z)} j_0\left(\frac{k_z L(z)}{2}\right) J_1\left(k_r R(z)\right)\right]^2 , \tag{5.10}$$

where L and R respectively represent the width along the line-of-sight and the spacial resolution of survey, $P(k)$ is the matter power spectrum, and ν_0 is the restframe frequency of 21cm line; i.e. $\nu_0 = 1.420$ GHz.

The flux weighted average of bias is given by

$$\beta(z) = \frac{\int_{M_{\rm min}}^{M_{\rm max}} b(M,z)\mathcal{F}(M)\frac{dn}{dM}dM}{\int_{M_{\rm min}}^{M_{\rm max}} \mathcal{F}(M)\frac{dn}{dM}dM} \ , \tag{5.11}$$

where $\mathcal{F}(M) \propto T_{\rm b} r_t^2 \sigma_{\rm V}$ is the effective flux from the MHs and $b(M,z)$ is the halo bias which we adopt the model of (Sheth et al., 2001) in this work.

5.3 Effects of isocurvature modes

As a preliminary step for estimating the effects from isocurvature modes, we parameterize the primordial power spectrum for isocurvature fluctuations as

$$\mathcal{P}_{S_i}(k) \equiv \mathcal{P}_{S_i}(k_0)\left(\frac{k}{k_0}\right)^{n_s^i - 1} \ , \tag{5.12}$$

where $i = c$ and b respectively indicate CDM and baryon isocurvature modes, $\mathcal{P}_{S_i}(k_0)$ and $n_s^{(i)}$ are respectively the amplitude and the spectra index for the mode i defined at the reference scale k_0. In this work, we take the reference scale k_0 as $k_0 = 0.05$ Mpc^{-1}. Then we define the primordial isocurvature fraction as

$$r_{\rm cdm} \equiv \frac{\mathcal{P}_{S_c}(k_0)}{\mathcal{P}_\zeta(k_0)} \ , \quad r_{\rm bar} \equiv \frac{\mathcal{P}_{S_b}(k_0)}{\mathcal{P}_\zeta(k_0)} \ , \tag{5.13}$$

where $\mathcal{P}_\zeta(k_0)$ is the amplitude of the primordial power spectrum for the adiabatic (curvature) perturbation ζ. For simplicity, we adopt the same values for the spectra indices of CDM and baryon isocurvature modes with $n_s^{\rm iso}$ (i.e. $n_s^c = n_s^b = n_s^{\rm iso}$).

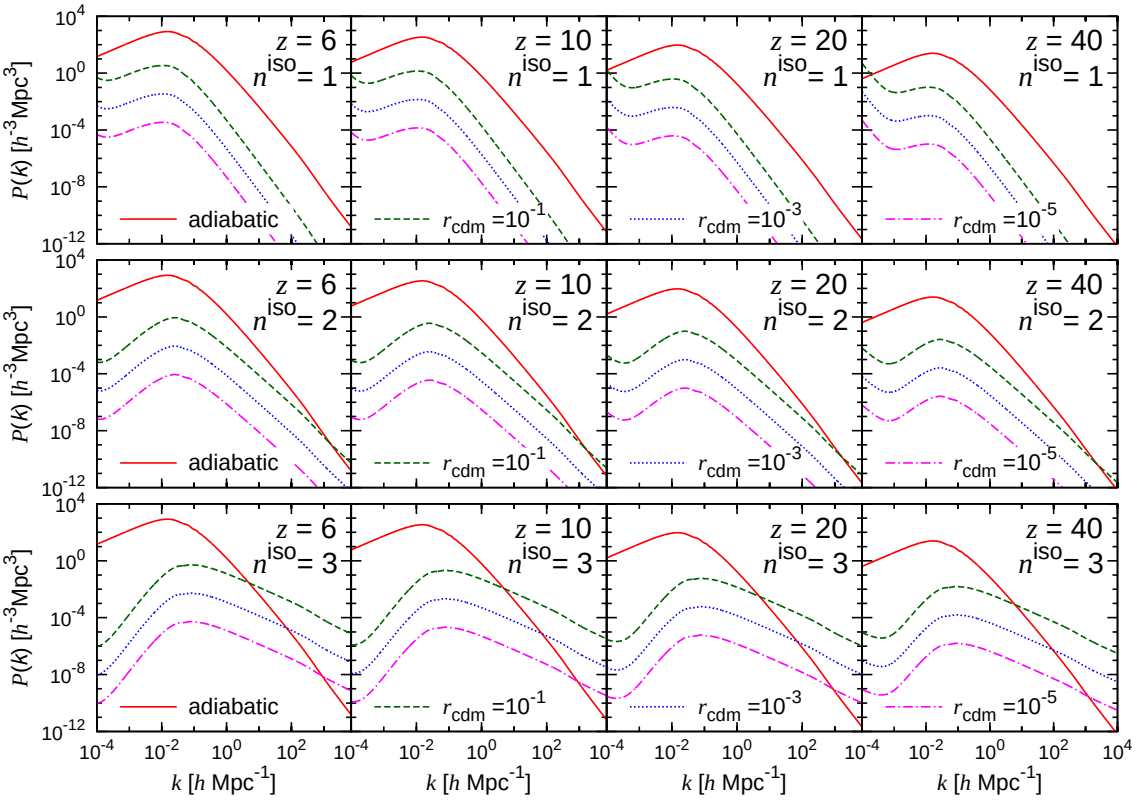

Figure 5.1: The matter power spectra of the adiabatic and pure CDM isocurvature fluctuations at redshifts $z = 6$, 10, 20 and 40 (from left to right). The spectral indices of the isocurvature mode are assumed as $n_s^{\rm iso} = 1$, 2 and 3, (from top to bottom). In each panel, the different curves represent the matter power spectrum of the adiabatic fluctuations (solid/red) and the CDM isocurvature fluctuations with $r_{\rm cdm} = 10^{-1}$ (dashed/green), 10^{-3} (doted/blue) and 10^{-5} (dash-dotted/magenta).

Before discussing the 21cm emission from MHs, we show the effects of isocurvature modes for the matter power spectra in Figure 5.1 at some redshifts ($z = 6$, 10, 20 and 40). We here adopt the pure CDM isocurvature mode and vary the fractional amplitude ($r_{\rm cdm} = 10^{-5}$, 10^{-3} and 10^{-1}) and the spectra index ($n_s^{\rm iso} = 1$, 2 and 3). For the very blue-tilted spectrum, $n_s^{\rm iso} = 3$, the effects of the CDM isocurvature mode can be identified clearly in small-scales, whereas the contribution of the isocurvature mode with scale-invariant spectrum ($n_s^{\rm iso} = 1$) is only a small effect for the matter power spectrum even with relatively large amplitude of isocurvature fluctuations.

In addition, we show deviation of the halo mass function due to isocurvature fluctuations in Figure 5.2, which is calculated from the matter power spectrum shown in Figure 5.1, and we here adopt the prescription of Press and Schechter (1974) for the reference model. The effect of the isocurvature mode becomes prominent in small-mass scales, and the effect appears more notably in higher-redshifts. We should note that isocurvature modes with very blue-tilted spectrum ($n_s^{\rm iso} = 3$) show the completely different features from the other spectrum with $n_s^{\rm iso} = 1$ or 2, their contribution to the halo mass function no longer show the smooth trend according to the

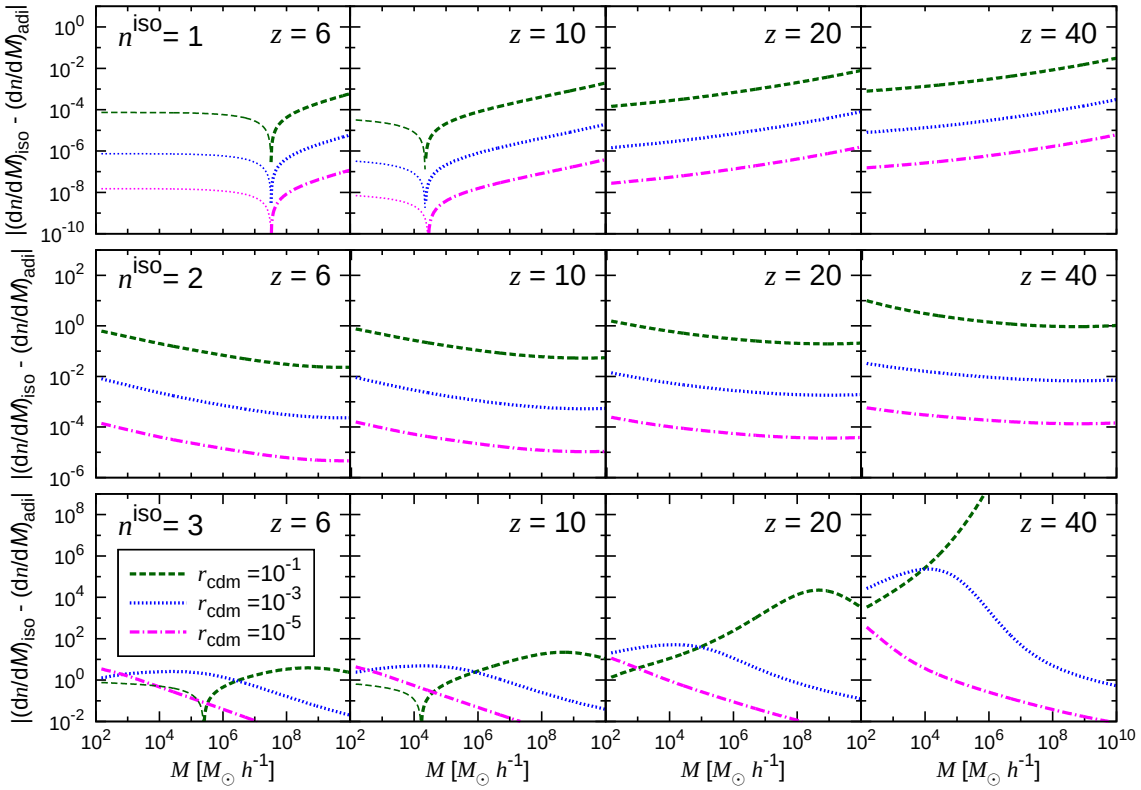

Figure 5.2: The deviations of the halo mass function for the case with pure CDM isocurvature fluctuations from the adiabatic case at redshifts $z = 6$, 10, 20 and 40 (from left to right), and we adopt the prescription of Press-Schechter. The thick lines represent positive values, whereas the thin lines represent negative values. The spectral indices of the isocurvature mode are assumed as $n_s^{\rm iso} = 1$, 2 and 3, (from top to bottom). In each panel, the different curves represent the deviation for the case with the CDM isocurvature fluctuations with $r_{\rm cdm} = 10^{-1}$ (dashed/green), 10^{-3} (doted/blue) and 10^{-5} (dash-dotted/magenta).

fractional amplitudes $r_{\rm cdm}$. The blue-tilted isocurvature spectrum enhances the fluctuations in small-scales, and leads to the increase of small haloes. However, if the contribution of isocurvature modes get more significant, the small haloes might become incorporated into a larger halo. As a result of such a process, the significant contribution of isocurvature modes causes such a strange feature that the abundance of haloes increases in the large-mass scales, but decreases in the small-mass scales. Such a feature appears in the mass-range of MHs, i.e. $M = [M_{\rm min}, M_{\rm max}]$, and it can be expected that the 21cm signal from MHs may also trace such a trend.

Finally, we show the r.m.s. fluctuations in the 21cm emission from MHs $\langle \delta T_{\rm b}^2 \rangle^{1/2}$ in Figure 5.3, and we here assume the pure CDM isocurvature modes. The sensitivity curves are for the LOFAR, SKA and FFTT missions, and the details on the sensitivity of each telescope are explained in the following section later. The contribution from the flat-isocurvature spectrum ($n_s^{\rm iso}$=1) is so small and the difference from the adiabatic mode is $\lesssim 10^{-4}$ mK even with $r_{\rm cdm} = 0.1$ and to distinguish

the isocurvature mode from the adiabatic mode should be hard work in this case. Even with more blue-tilted isocurvature spectrum ($n_s^{\rm iso} = 2$), the contribution to the 21cm emission from MHs is still faint, but the model with $r_{\rm cdm} = 0.1$ enhances the signal by more than a few percent around the peak redshifts. For the very blue-tilted isocurvature spectrum ($n_s^{\rm iso} = 3$), the case with large amplitude of isocurvature fluctuations predicts the large signal at high-redshifts, whereas such spectrum shows the smaller amplitude of the fluctuations in the 21cm emission form MHs around $z \lesssim 20$ than that with smaller amplitude of the isocurvature fluctuations. This is the results of the incorporation of MHs into a larger halo, which is discussed above section. Because of such a process, the abundance of MHs decreases due to the significant contribution of isocurvature modes and the similar features can be seen on the halo mass function shown in Figure 5.2.

The detection of isocurvature modes through the fluctuations in the 21cm emission from MHs can be possible by future telescopes such as SKA and FFTT. If isocurvature fluctuations has very blue-tilted spectrum and the amplitude of $r_{\rm cdm} \simeq 10^{-3}$, the signals from the isocurvature mode might be detected at low redshifts even by LOFAR. However, the case with the larger amplitude of $r_{\rm cdm}$ is impossible because the larger amplitude of $r_{\rm cdm}$ drives the incorporation of MHs into a larger halo and suppress the signal at $z \lesssim 20$. We discuss the systematics or uncertainties on the estimation of the 21cm signal from MHs in more detail later in Sec. 5.6.

In the following sections, we investigate how accurately we can put he constraints on isocurvature modes from the observation of the 21cm emission form MHs with future radio telescopes.

5.4 Forecasts

We put the constraints on the cosmological parameters from the expected measurements of CMB and the fluctuations in the 21cm line from MHs with the Fisher matrix analysis. We define the total Fisher information matrix by combining the CMB and the 21cm line surveys as

$$F_{\alpha\beta} = F_{\alpha\beta}^{(\rm CMB)} + F_{\alpha\beta}^{(\rm 21cm)} \ , \tag{5.14}$$

where α, β refer to the model parameters, and $F_{\alpha\beta}^{(\rm CMB)}$ and $F_{\alpha\beta}^{(\rm 21cm)}$ respectively represent the contributions from CMB and 21cm observations, which are explained below. We adopt following 12 model parameters for our analysis;

$$\boldsymbol{p} = \{\Omega_{\rm b}h^2,\ \Omega_{\rm c}h^2,\ \Omega_\Lambda,\ \tau^{\rm reion},\ n_{\rm s},\ A_{\rm s}, w,\ Y_p,\ \alpha_{\rm s},\ r_{\rm cdm}, r_{\rm bar},\ n_s^{\rm iso}\} \ , \tag{5.15}$$

where $\Omega_{\rm b}$, $\Omega_{\rm c}$ and Ω_Λ are the density parameter of baryon, CDM and cosmological constant, respectively; h is the dimension less Hubble constant; w is the equation of state for dark energy; Y_p is the primordial abundance of Helium; $\tau^{\rm reion}$ is the optical depth at the EoR [¶] ; $n_{\rm s}$ and $A_{\rm s}$ are the spectra index and the amplitude of the initial power spectrum for the adiabatic mode,

[¶]We treat $\tau^{\rm reion}$ as a model parameter only for CMB and $\tau^{\rm reion}$ does not affect the signal of 21 cm lines in our analysis. Therefore the constraint of $\tau^{\rm reion}$ comes only from CMB.

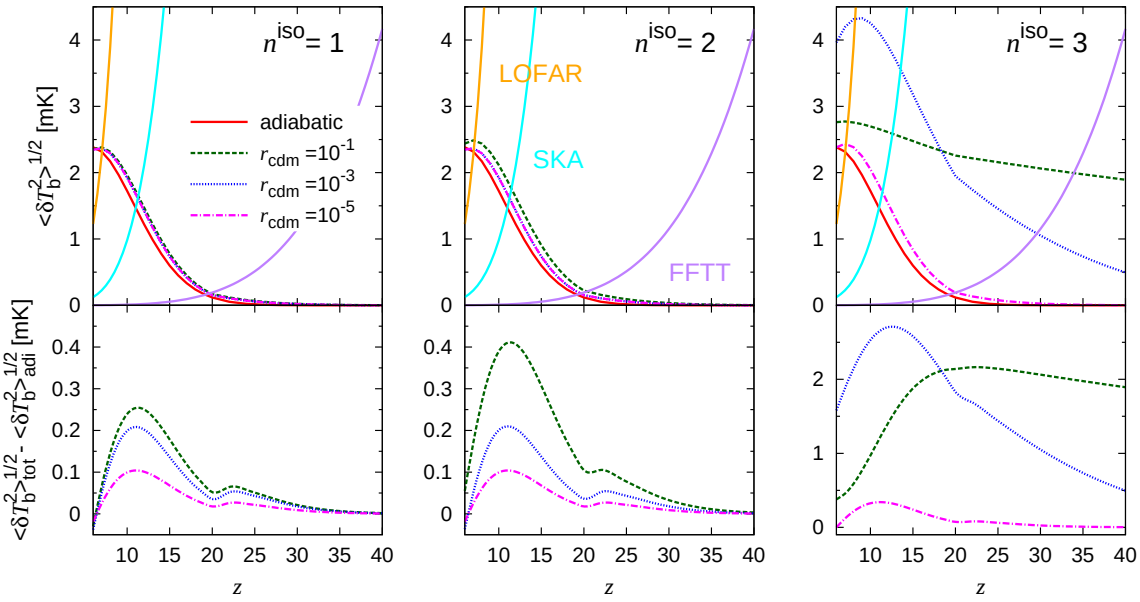

Figure 5.3: *Top panels*: The r.m.s. fluctuations in the 21-cm emission from MHs $\langle \delta T_{\rm b}{}^2 \rangle^{1/2}$ and the sensitivity curves for LOFAR (orange), SKA (cyan) and FFTT (purple) missions. In each panel, we adopt the the prescription of Press-Schechter for the halo mass function, and the different curves represent the case for the adiabatic condition (solid/red) and the case with pure CDM isocurvature fluctuations with $r_{\rm cdm} = 10^{-1}$ (dashed/green), 10^{-3} (doted/blue) and 10^{-5} (dash-dotted/magenta).. *Bottom panels*: The deviations from the adiabatic case and each curve corresponds to that of top panel. The spectral indices are assumed as $n_s^{\rm iso} = 1$, 2 and 3, (from left to right).

respectively; $\alpha_{\rm s}$ is the running for the primordial power spectrum; $r_{\rm cdm}$ and $r_{\rm bar}$ are the ratios of the amplitude of the initial power spectrum for the CDM and baryon isocurvature modes, respectively; $n_s^{\rm iso}$ is the spectra index for isocurvature modes.

5.4.1 CMB

The Fisher information matrix for the CMB survey is given by (Tegmark et al., 1997)

$$F_{\alpha\beta}^{\rm (CMB)} = f_{\rm sky}^{\rm CMB} \sum_{\ell=2}^{l_{\rm max}} \frac{2\ell+1}{2} {\rm Tr}\left[\mathbf{C}_{\ell;\alpha}\mathbf{C}_\ell^{-1}\mathbf{C}_{\ell;\beta}\mathbf{C}_\ell^{-1}\right] \ , \tag{5.16}$$

where α, β refer to the model parameters, $f_{\rm sky}^{\rm CMB}$ is the sky coverage of the CMB survey, $\mathbf{C}_\ell$ is the covariance matrix and $\mathbf{C}_{\ell;\alpha}$ represents its derivative by the parameter p_α; $\mathbf{C}_{\ell;\alpha} \equiv \partial \mathbf{C}_\ell / \partial p_\alpha$. As for the CMB observables, we consider the temperature anisotropies (T), the E-mode polarization E, and the CMB lensing potential (ψ), then the covariance matrix of the CMB observables is

Experiment	ν [MHz]	$\theta_{\rm FWHM}$ [arcmin]	Δ_ν^T [μK arcmin]	Δ_ν^P [μK arcmin]
CMBPol	45	17	5.85	8.27
	70	11	2.96	4.19
	100	8	2.29	3.24
	150	5	2.21	3.13
	220	3.5	3.39	4.79

Table 5.1: The specification for the CMBPol (EPIC-2m) mission used in our analysis. ν refers the frequency of each channel, $\theta_{\rm FWHM}$ is the angular resolution, Δ_ν^T, and Δ_ν^P respectively represent the sensitivity for the temperature and polarization.

defined as

$$\mathbf{C}_\ell \equiv \begin{pmatrix} C_\ell^{TT}+N_\ell^{TT} & C_\ell^{TE} & C_\ell^{T\psi} \\ C_\ell^{TE} & C_\ell^{EE}+N_\ell^{EE} & C_\ell^{E\psi} \\ C_\ell^{T\psi} & C_\ell^{E\psi} & C_\ell^{\psi\psi}+N_\ell^{\psi\psi} \end{pmatrix} , \tag{5.17}$$

where C_ℓ and N_ℓ represent the angular power spectrum and the noise spectrum, respectively. For simplicity, we assume that the cross-correlation between E-mode polarization and the CMB lensing potential can be negligible (i.e. $C_\ell^{E\psi}=0$) [‖]. The noise spectra of the CMB observation is given by (Knox, 1995)

$$N_\ell^{T,P} = \left[\sum_\nu \left\{ \left(\Delta_\nu^{T,P}\theta_{\rm FWHM}\right)^2 e^{-\ell(\ell+1)\theta^2_{\rm FWHM}/8\ln 2} \right\}^{-1} \right]^{-1} , \tag{5.18}$$

where $\Delta_\nu^{T,P}$ denotes the sensitivity for the temperature or polarization, and $\theta_{\rm FWHM}$ represents the angular resolution. We estimate the noise spectrum for the CMB lensing potential following the manner in (Hu and Okamoto, 2002; Okamoto and Hu, 2003).

In this work, we assume the projected CMBPol (Baumann et al., 2009) mission and we adopt $f_{\rm sky}^{\rm CMB}$=1 and $\ell_{\rm max}$=4000. We use the specification for the mid-cost CMBPol (EPIC-2m) mission which is shown in Table 5.1.

5.4.2 21cm line from minihaloes

For the 21cm emission line survey, we define the Fisher information matrix as

$$F_{\alpha\beta}^{(21{\rm cm\,MH})} = f_{\rm sky}^{21{\rm cm}} \sum_i \sum_{\rm pixel} \left(\frac{\partial S^i}{\partial p_\alpha}\right) \frac{1}{2(S^i+N^i)^2} \left(\frac{\partial S^i}{\partial p_\beta}\right) , \tag{5.19}$$

[‖]The E-mode polarization is generated via the Thomson scattering around last scattering surface wheres the source of CMB lensing is the large-scale structures from the last scattering surface to us, therefore this assumption is almost valid. However, strictly speaking, they should have non-vanishing cross-correlation, because the E-mode polarization can be generated during the EoR and the structures in such era also contribute to the lensing sources (Lewis et al., 2011).

where i refers to the redshift slices, $f_{\rm sky}^{\rm 21cm}$ is the sky coverage for the 21cm survey, S^i and N^i represent the signal and the noise in the i-th redshift slice. In our analysis, we define the signal and the noise as $S^i \equiv \langle \delta T_{\rm b}^2(z_i)\rangle^{1/2}$ and $N^i \equiv \delta T_N(z_i)$, respectively, and $\delta T_N(z)$ is given by (Furlanetto et al., 2006a)

$$\delta T_N(z) = 20{\rm mK}\frac{10^4{\rm m}^2}{A_{\rm tot}}\left[\frac{10'}{\Delta\theta}\right]^2\left[\frac{1+z}{10}\right]^{4.6}\left[\frac{\rm MHz}{\Delta\nu}\frac{\rm 100hr}{t_{\rm int}}\right]^{1/2}, \tag{5.20}$$

where $A_{\rm tot}$ is the effective collecting area of the telescope, $\Delta\theta$ is the spacial angular resolution, $\Delta\nu$ is the frequency band width , and $t_{\rm int}$ is total integration time. The noise thresholds for each sensitivity curve shown in Figure 5.3 assume total effective areas $A_{\rm tot} = 10^4$ m^2 (LOFAR), $A_{\rm tot} = 10^5$ m^2 (SKA) and $A_{\rm tot} = 10^7$ m^2 (FFTT), and $t_{\rm int} = 1000$ hours integration time is adopted in each case.

As a fiducial survey model in our analysis, we mainly focus on the observation by the FFTT survey and we assume the following survey parameters; $A_{\rm tot}$=10^7 m^2, $\Delta\theta$=10 arcmin, $\Delta\nu$=1 MHz, and $t_{\rm int}$=1000 hours.

5.5 Result

We summarize the constraints on isocurvature modes from CMB and the fluctuations in the 21cm emission of MHs in Figure 5.4. The contours show the projected 1σ (68%) and 2σ (95%) CL constraints expected from CMBPol alone and the combination with the 21cm line survey such as SKA or FFTT. We here choose the redshift range of $z = [6, 40]$ at certain intervals of $\Delta z = 1$.

As shown in the previous section, the contribution from the scale-invariant isocurvature spectrum to the fluctuations in the 21cm emission from MHs is less significant, and the improvement from the constraint by CMBPol alone is also less significant. On the other hand, the improvement by adding the information of the 21cm survey can be possible for the blue-tilted isocurvature spectra. Compared to the constraint from CMB, the constraint from the 21cm survey alone is so poor due to the strong degeneracies with the other cosmological parameters even for the blue-tilted isocurvature spectra. However the information from CMB helps to break the degeneracies.

Comparing the constrains from SKA and FFTT, both constraints show the almost consistent results except the fiducial mode with very blue-tilted isocurvature fluctuations ($n_s^{\rm iso} = 3$), but the constraint from FFTT is a little bit tighter than that from SKA. We here adopt the maximum redshift of $z_{\rm max} = 40$, As a conservative results, we show the constrains from FFTT by utilizing the information from lower-redshifts in Figure 5.5. The contours show the 1σ CL areas expected from CMBPol and FFTT and we here adopt the maximum redshift of $z_{\rm max} = 20$, 30 and 40. If we use the information up to $z_{\rm max} \sim 40$, we can see the signature differentiating CDM and baryon isocurvature modes. We have checked that the constraints from SKA are saturate with $z_{\rm max} \gtrsim 20$.

For the flat spectrum ($n_s^{\rm iso} = 1$), the constraint on the $r_{\rm cdm}$-$r_{\rm bar}$ plane is dominated by CMB

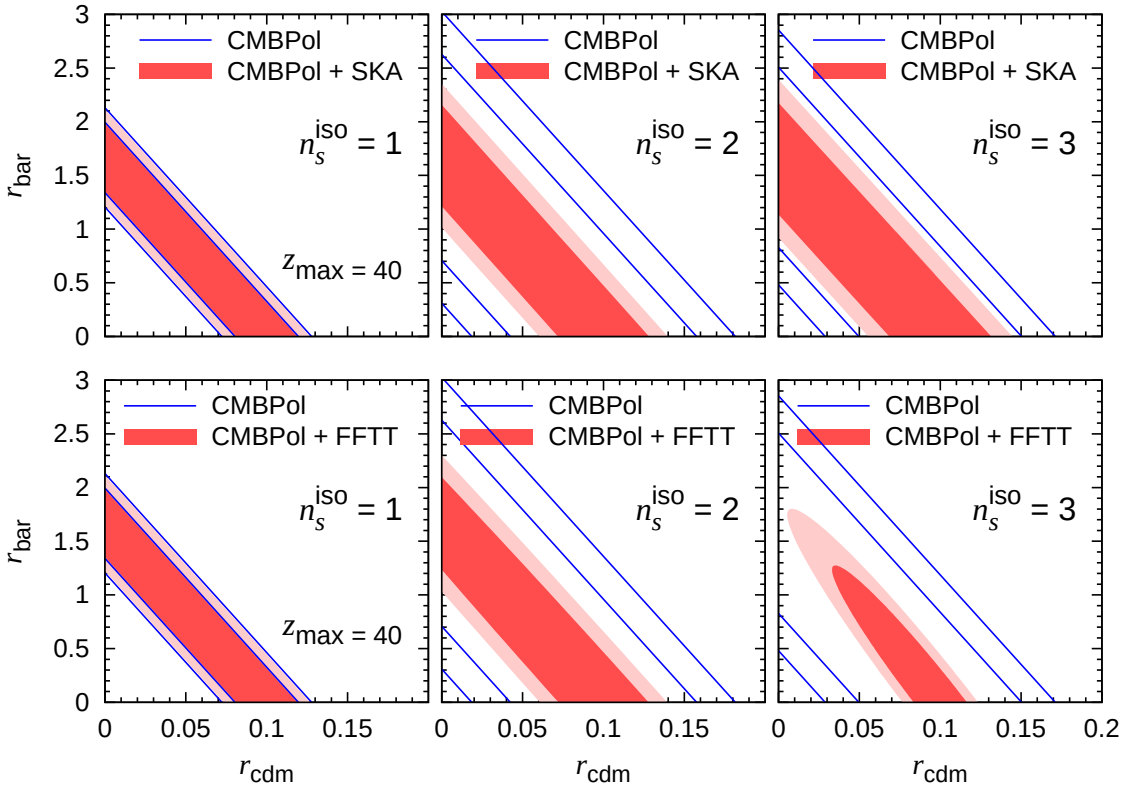

Figure 5.4: Projected 1σ (68 %) and 2σ (95 %) CL constraints on $r_{\rm cdm}$ and $r_{\rm bar}$ from CMB alone (solid/blue line) and CMB + 21-cm (shaded/red region). We assume the CMBPol mission for the CMB observation and the SKA (top panels) or FFTT (bottom panels) mission for the observation of the 21-cm emission from MHs. As for the fiducial model, the spectral indices of isocurvature modes are assumed as $n_s^{\rm iso} = 1$, 2 and 3 (from top to bottom), and the amplitude is adopted as $(r_{\rm cdm}, r_{\rm bar})$=$(0.1, 0)$ in all cases.

and the contribution from the 21cm line survey is less important, whereas the constraint on the spectra index of isocurvature fluctuations $n_s^{\rm iso}$ is improved by the 21cm line survey. The 21cm survey has potential to improve the constraints for the blue-tilted isocurvature spectra and to put the tighter constraints on isocurvature fluctuations than CMB. Therefore the information of the fluctuations in the 21cm emission from MHs works extremely well for the prove of blue-tilted isocurvature fluctuations, and we hereafter focus on the constraints for the very blue-tilted isocurvature fluctuations ($n_s^{\rm iso} = 3$). The detection of such isocurvature fluctuations may open the new window for the physics in the early Universe and some models predict very blue-tilted isocurvature spectrum with $n_s^{\rm iso} = 2$ - 4, which are discussed in (Kasuya and Kawasaki, 2009).

To understand which redshift slices put the constraints on isocurvature modes the most effectively, we show the some diagonal components for the inverse matrix of the Fisher information matrix $(\boldsymbol{F}^{-1})_{\alpha\alpha}$, which correspond to the marginalized 1σ error, and unmarginalized 1σ error in Figure 5.6; for $r_{\rm cdm}$, $r_{\rm bar}$ and $n_s^{\rm iso}$. The observation of the 21cm survey is assumed with FFTT,

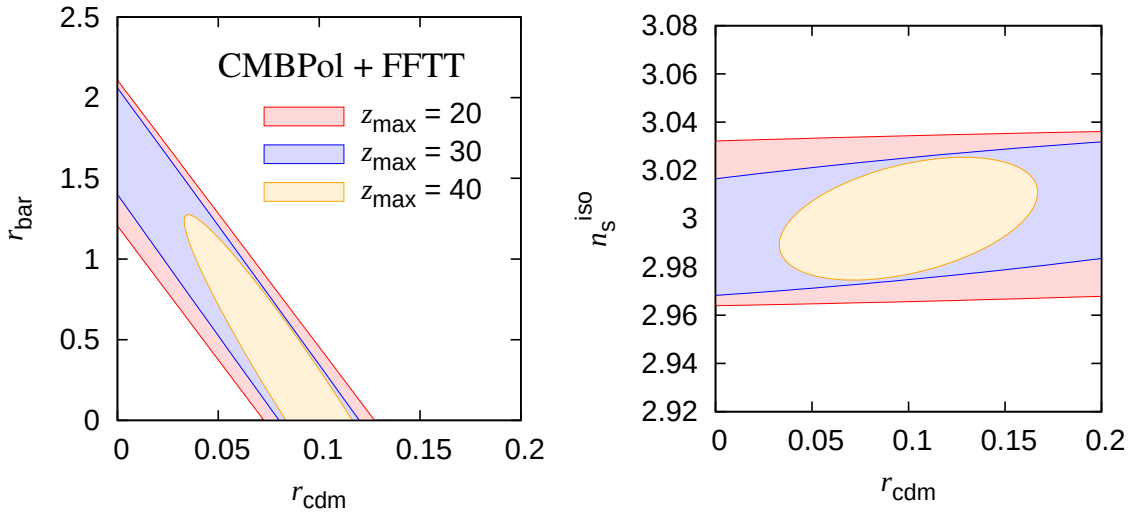

Figure 5.5: The 68 % CL constraints from the CMBPol and FFTT surveys. The fiducial model is the adiabatic mode plus the pure CDM isocurvature mode with $r_{\rm cdm} = 0.1$ and $n_s^{\rm iso} = 3$. The different colors represent the maximum redshift range of the 21cm line survey; $z_{\rm max} = 20$ (red), 30 (blue), 40 (orange), and the minimum redshift of $z_{\rm min} = 6$ is adopted in all cases.

and we add the CMB prior from the CMBPol survey in each redshift slice.

For the unmarginalize error, the minimum points of 1σ errors appear around $z \sim 20$, and which is a little bit higher than the peaks of the 21cm signal from MHs. This is because the effects of isocurvature modes appear more prominently at higher-redshifts, though the the signal-to-noise ratio of the 21cm emission from MHs has peak around $z \sim 10$. On the other hand, the marginalized errors show the different trends from the unmarginalized errors for $r_{\rm cdm}$ and $r_{\rm bar}$. It is related to the strong degeneracy between CDM and baryon isocurvature modes, or degeneracies with the other cosmological parameters. As discussed in Kawasaki et al. (2011), the difference between CDM and baryon isocurvature modes become prominent in large-scales, and the observation at higher-redshift allow to take the larger correlation length with same angular scale. Therefore the marginalized constraints on $r_{\rm cdm}$ and $r_{\rm bar}$ are reduced with the increase of the observing redshift. However the constraint from a single redshift slice is not so significant. For the tighter constraints on isocurvature modes, the tomographic survey which combines the information from different redshift slices is essential.

Finally we estimate the effects of survey area for the constraint of isocurvature modes. As a reference survey design for the observation of the 21cm line, we assume the ambitious all sky survey. We compare the constraints from the fluctuations in the 21cm emission of MHs with different values of the survey area; $f_{\rm sky} = 0.01$, 0.1, 0.5 and 1, and show the 1σ CL areas in Figure 5.7. To get the tight constraint which exclude $r_{\rm cdm} = 0$ with 1σ CL, more than half sky survey is essential for our reference survey model. On the other hand, the spectra index can be

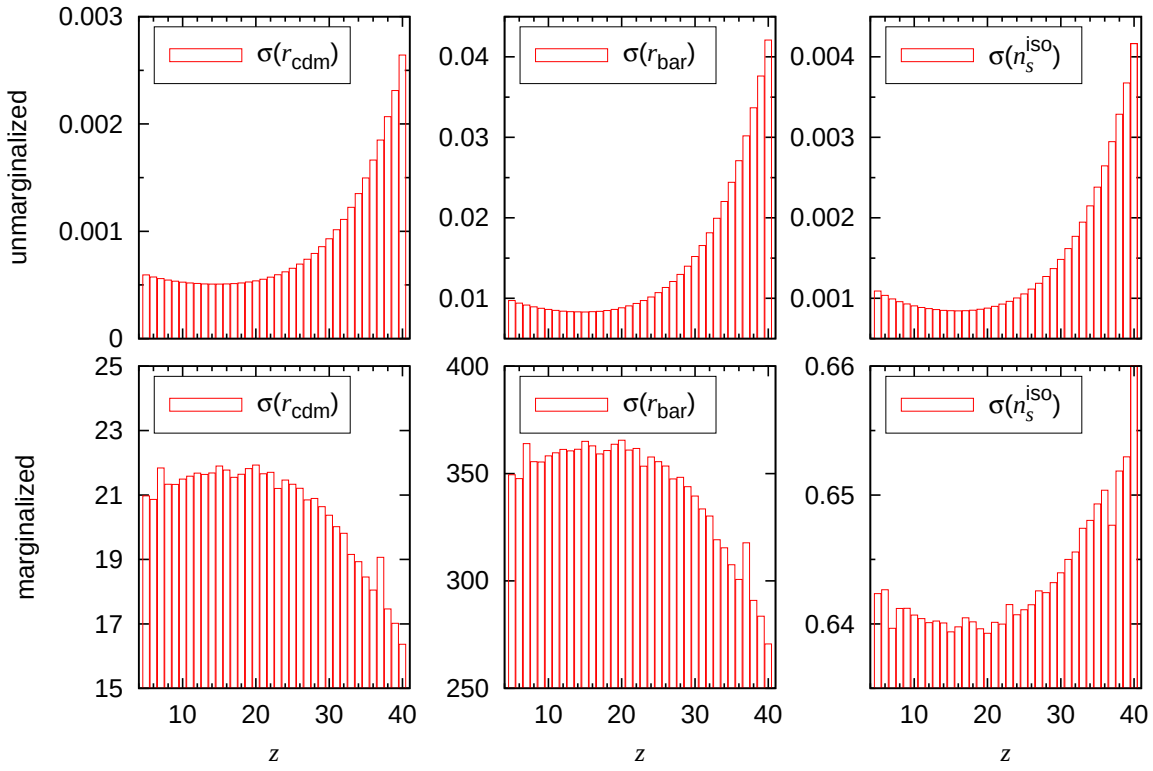

Figure 5.6: The unmarginalize (top panels) and marginalize (bottom panels) 1σ errors expected from each single redshift slice with CMB prior. The fiducial model is the adiabatic mode plus the pure CDM isocurvature fluctuations with $(r_{\rm cdm},r_{\rm bar})$=(0.1,0) and $n_s^{\rm iso}=3.0$, and the observations by the CMBPol and FFTT missions are assumed. The spatial and frequency resolutions are adopted with $\Delta\theta$=9 arcmin and $\Delta\nu$=1 MHz in each redshift slice.

determined by a few percent accuracy even with $f_{\rm sky}=0.1$.

5.6 Discussion

We here consider some ambiguous aspects on the estimation of the 21cm signal from MHs, which come from either the difficulty to understand the non-linear physics on small-scales, which is related to the MHs, or the uncertainty of the history of reionization. Following the discussion in (Chongchitnan and Silk, 2012), we also focus on the three aspects; (i) halo mass function, (ii) uncertainty of mass range of MHs, (iii) radiative coupling through the Lyα pumping, and investigate the effects from them to the 21cm signal from MHs and the constraints on isocurvature modes.

MHs are extremely small objects and their dynamics are governed by non-linearity on small-scales, therefore we have to lean much on the N-body simulations. However it is quite hard

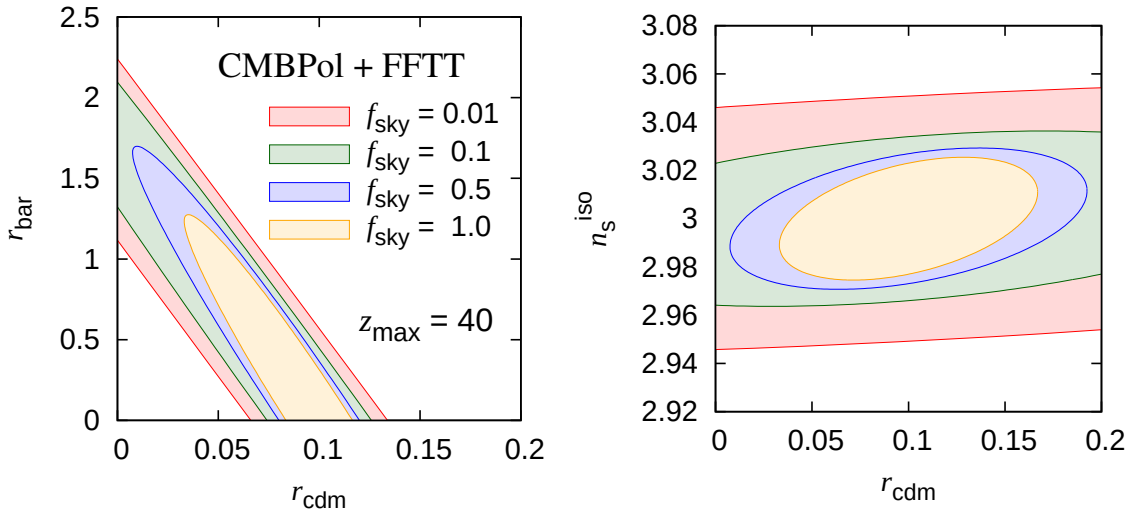

Figure 5.7: Projected 68 % CL constraints from CMBPol and FFTT with different survey area; $f_{\rm sky} = 0.01$ (red), 0.1 (green), 0.5 (blue) and 1.0 (orange). The fiducial model is the adiabatic mode plus the pure CDM isocurvature fluctuations with $r_{\rm cdm} = 0.1$ and $n_s^{\rm iso} = 3$, and the maximum redshift of $z_{\rm max} = 40$ is assumed for all cases.

to resolve the such scale of MHs in N-body simulations, and the 21cm signal from MHs shall depend on the model of halo mass function. We here investigate how the 21cm emission from MHs is affected by the choice of mass function. In the left panels of Figure 5.8, we show the 21cm fluctuations for $(r_{\rm cdm}, r_{\rm bar}) = (0.1, 0)$ (top) and $(r_{\rm cdm}, r_{\rm bar}) = (10^{-3}, 0)$ (bottom) using the halo mass functions of Press and Schechter (1974), Sheth and Tormen (1999), Tinker et al. (2008) and (Warren et al., 2006).

For the case of smaller contribution of isocurvature fluctuations ($r_{\rm cdm} = 10^{-3}$), as claimed in (Chongchitnan and Silk, 2012), the Press-Schechter and Tinker prescriptions similarly high amplitudes of the signal from MHs, whereas the Warren and Sheth-Tormen prescriptions show lower amplitudes. Then the trends are reversed for high-redshifts. Even for the case of larger contribution of isocurvature fluctuations ($r_{\rm cdm} = 0.1$), similar trends still remains except the Press-Schechter prescription and the reversed trends can not be seen in this redshift range. In any case, the uncertainty in the mass function hardly affects the prospects for the detection so significantly.

In Figure 5.9, we show the constraints adopting the different models of the halo mass function. Each model of the halo mass function predicts the different constraints and correlations of parameters, and the model which predicts the larger amplitudes of $\langle \delta T_{\rm b}{}^2 \rangle^{1/2}$ show relatively tighter constraints. Especially the Press-Schechter prescription shows small-correlations on the $n_s^{\rm iso} - r_{\rm cdm}$ plane, and has possibility to overestimate the constraints on isocurvature modes.

The other uncertainty of the signal from MHs is the mass range of MHs. For instance, the

large relative velocity between dark matter and baryons cause the adovection of baryons out of dark matter potential and may lead to such situation of $M_{\rm min} > M_{\rm J}$ (Tseliakhovich et al., 2011). The lower bound alter the signal more significantly than the upper bound because of the sharp depression of halo mass function and there are much more haloes in small-mass scales than in large-mass scales. In this work, we determined the lower bound of MHs from the Jeans mass $M_{\rm J}$, however the Jeans mass is just the mass scale which the objects start to collapse by their self-gravity and the minimum mass of haloes might be actually larger than $M_{\rm J}$. The signals for the different values of $M_{\rm min}$ are shown in the middle panel of Figure 5.8 and we here adopt the value of the minimum mass of MHs as $10M_{\rm J}$, $50M_{\rm J}$ and $100M_{\rm J}$.

The increase of the value of $M_{\rm min}$ suppresses the signal over all redshifts and the effects become more prominent at higher-redshifts. Basically the increase of $M_{\rm min}$ reduces the total number of MHs . Compared to the lower-redshifts, there are less haloes with large mass in higher-redshifts and the total number of MHs falls to an extremely low level when $M_{\rm min}$ is increased.

In the middle panels in Figure 5.9, we show the constraints on isocurvature modes when the minimum mass of MHs is varied to $M_{\rm min} = 1M_{\rm J}$, $10M_{\rm J}$, $50M_{\rm J}$, and $100M_{\rm J}$. The signal gets lower when $M_{\rm min}$ is increased, and the constraints on isocurvature modes become poor. The effects of isocurvature modes appears relatively prominently at higher-redshifts, therefore the suppression of signal at higher-redshifts is crucial for the constraints on isocurvature modes.

Finally, we estimate the effects of the coupling with radiation field for the 21cm signal from MHs and constraints on isocurvature modes. We assume that the radiative coupling can be neglect and adopt $y_\alpha = 0$ thus far, but we here adopt the Ly-α coupling factor given by (Chuzhoy and Shapiro, 2006)

$$y_\alpha = 1.3 \times 10^{-12} \left[\frac{J_\alpha T_*}{A_{10} T_{\rm k}} \right] \frac{\exp\left(-0.3(1+z)^{1/2} T_{\rm k}^{-2/3}\right)}{1 + 0.4 T_{\rm k}^{-1}} \ , \tag{5.21}$$

where J_α denotes the fraction to the typical value for the flux intensity of radiation field. We show the effects of Ly-α pumping for the signal from MHs in the right panel of Figure 5.8 and we here adopt the value of J_α as 0.1 0.5 and 1.0.

The effects of Ly-α pumping can be seen especially around the EoR and less prominent at higher-redshifts. The radiation intensity increase then the spin temperature couples to the temperature of radiation sources, and the emission from MHs will be suppressed due to the huge absorption signal from the IGM. However there are less radiation sources at higher-redshifts and the effects of Ly-α will be small (due to the exponential dumping in Eq. (5.21)).

The constraints on isocurvature modes are shown in the right panels of Figure 5.9. Compared to the choice of the mass function and the uncertainty of the minimum mass value of MHs, the uncertainty of the coupling with the radiation field seems less serious. Stating a little bit more in detail, a large change can be seen between $J_\alpha = 0.1$ and 0.5. Although the signal is suppressed by Ly-α pumping, the constraints are improved for the strong effects from Ly-α pumping. Through the Ly-α pumping, the mean 21cm emission $\overline{\delta T_{\rm b}}$ is submerged under the absorption signal from IGM and suppressed with increase of J_α, while the variance of density field σ_p and the bias β are

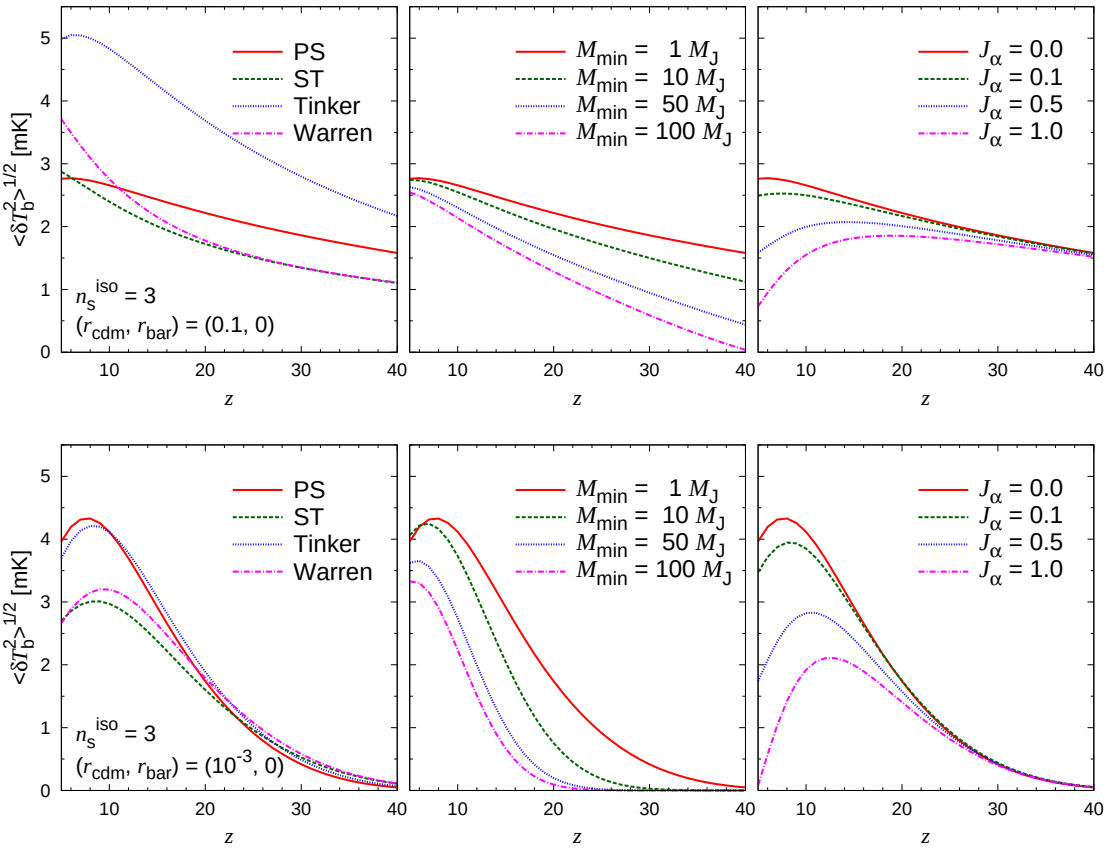

Figure 5.8: Systematics of the fluctuations in the 21-cm emission from MHs. The fiducial model is the case with pure CDM isocurvature with $r_{\rm cdm} = 0.1$ (top-panels) or 10^{-3} (bottom-panels) and $n_s^{\rm iso} = 3$ and we adopt the PS's halo mass function. (Left) The model of halo mass function; PS (Press and Schechter, 1974), ST (Sheth and Tormen, 1999), Tinker (Tinker et al., 2008) and Warren (Warren et al., 2006). (Middle) The minimum mass of MHs; $M_{\rm min} = 1M_{\rm J}$, $10M_{\rm J}$, $50M_{\rm J}$ and $100M_{\rm J}$. (Right) The effects of Ly-α pumping; $J_\alpha = 0.0$, 0.1, 0.5 and 1.0.

hardly affected by the Ly-α pumping. Therefore the deviation of parameter which is sensitive to σ_p or β stands out and leads to the increase information related such parameter. For these reasons, the constraints of some parameters (e.g. $\Omega_{\rm b}h^2$ and $\Omega_{\rm c}h^2$) are improved. Then the parameter degeneracies between the isocurvature fluctuations and such parameters are also broken and it leads to the improvement of the constraints on isocurvature modes.

5.7 Summary

We estimated the effects of isocurvature modes for the 21cm emission lines from MHs at high-redshifts. For the isocurvature fluctuations with scale-invariant primordial spectra hardly affect the abundance of MHs and change the 21cm signal from MHs by less than a few percent around its

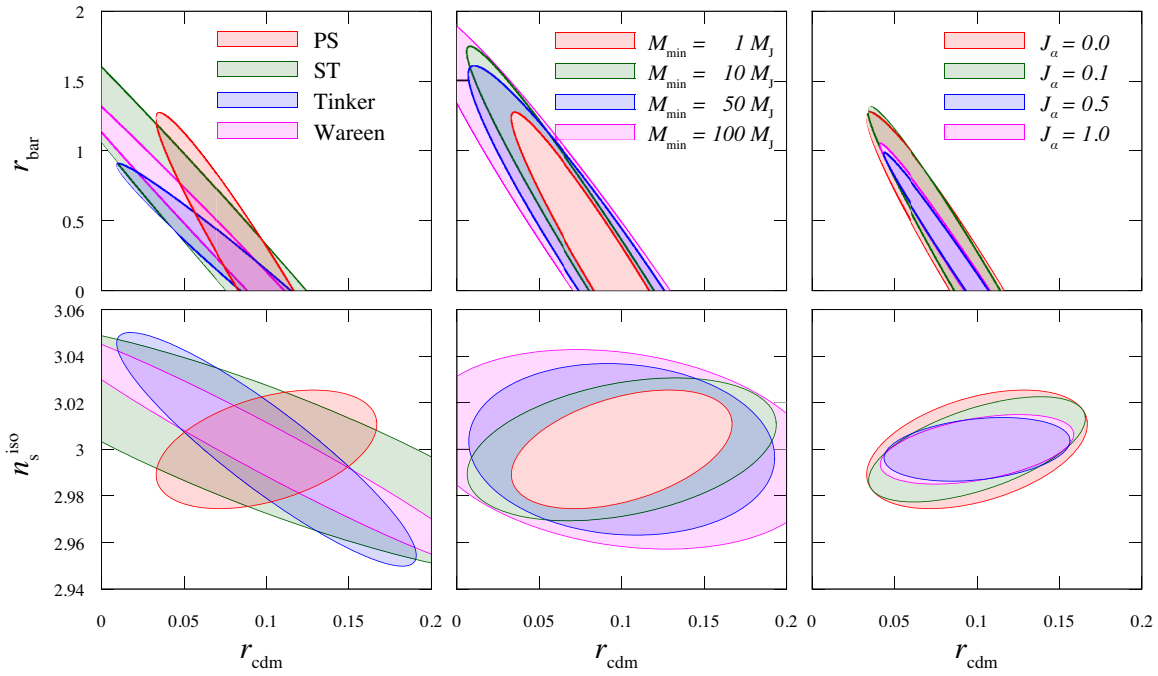

Figure 5.9: Projected 68 % CL constraints from CMBPol and FFTT with maximum redshift of $z_{\rm max} = 40$, when the halo mass function (Left), the minimum mass of MHs $M_{\rm min}$ (Middle), or J_α (Right) is changed.

peak. However, strongly blue-tilted spectrum of isocurvature modes lead to a significant increase in the amplitude of the fluctuations and the huge radio telescope in the next generation such as SKA and FFTT have potential for detecting the signals from such isocurvature modes.

Furthermore we confirmed the characteristic signature on the abundance of MHs and the 21cm signal from MHs due to isocurvature modes. In some cases, the isocurvature fluctuations with larger amplitude predicts the smaller abundance of MHs and 21cm signal from MHs than that with smaller amplitude at low-redshifts. We considered that this is because of the interpolations of MHs into the larger haloes. Although the very blue-tilted isocurvature spectrum enhance the fluctuations in small-scales and will create more MHs, too much of fluctuations induce the incorporation of MHs and collapse into a larger halo if the density fluctuations around such MHs reaches the critical density.

Then we investigated how well the fluctuations in the 21cm emission of high-redshift MHs can constrain on isocurvature modes by the Fisher matrix analysis. For the isocurvature fluctuations with scale-invariant primordial spectra, it seems to be difficult to improve the constraints from the observation of CMB and the difference between the CDM and the baryon isocurvature fluctuations can not be seen even with the FFTT and CMBPol surveys. However, the very blue-tilted isocurvature spectrum can distinguish CDM and baryon isocurvature modes if we observe high-redshifts $z \gtrsim 40$.

We discussed the systematics on the estimation of the 21cm signal from MHs, which are about the uncertainties of the halo mass function, the effect of radiative coupling through pumping processes by the Ly-α photons, and the mass range of MHs. The uncertainty of halo mass function should be the most significant for the detection of isocurvature modes. Due to the incorporation processes of MHs on the existence of isocurvature modes, the signals show irregular trends for the model of halo mass function in some cases. However the signal remains enough large to observe and can be detect by the SKA or FFTT surveys. The uncertainty of the mass range of MHs changes the signal over all redshifts and the increase of the lower bound mass suppresses the signals at high-redshifts significantly even by a order of magnitude. On the other hand, the Ly-α pumping processes suppress the signal around the EoR, but shall be negligible at high-redshifts.

Furthermore we estimate the effects for the constraints on isocurvature modes for each case. The constraints on isocurvature modes significantly depends on the model of mass function, and especially the prediction of Press-Schechter has possibilities to under-estimate the constraints. The effect of the Ly-α pumping is significant around the EoR, but the tight constraints on the isocurvature modes comes from the higher-redshifts. Therefore the effect of the Ly-α pumping has lesser impact on the constraints. On the other hand, the increase of the lower mass bound of the MHs suppress the signals at high-redshifts significantly, and the constraints are also severely affected.

The verification of isocurvature modes by the fluctuations in the 21cm signal from MHs will be a power full tool, especially for the very blue-tilted isocurvature spectrum. For the observation of CMB, the detection of very blue-tilted isocurvature spectrum is difficult because the CMB spectrum dumps rapidly in small-scales. Furthermore the observation of the 21cm line has potential to distinguish the CDM and baryon isocurvature modes and can give some important implications for the mechanism of the CDM and baryon matter generations.

Our analysis focused on the pure CDM or baryon isocurvature modes, but we have not taken into account the degree of correlation between the isocurvature mode and the adiabatic mode. Although the addition of these parameters leads to a large number of degrees of freedom, the values of the parameters can be limited to certain values from the theoretical or the phenomenological aspects in some cases. Therefore our future analyses should be extended to the specific cases.

[Note: prior to the publication of this work, we became aware of the work by Sekiguchi et al. (2013), which significantly overlaps with our work. The conclusions in their work are similar to ours.]

Chapter 6

Conclusion

It has been expected that the upcoming huge radio interferometer missions can probe the history of the cosmic reionization through the observation of the 21cm line from the IGM at EoR and the competitive race for detecting the signal from EoR has already started. To utilize data from such surveys exhaustively, the more careful theoretical understanding on the physics around EoR. Furthermore, the investigations for the detectability of signals and the accuracies of determination for model parameters are also strongly required for the next generation radio surveys such as SKA and FFTT.

First, we studied the signals due to the hyperfine transition of not only hydrogen but also isotope helium-3 from filamentary structures in the IGM at low-redshifts with a view to probe the missing baryon problem. After the EoR, the Universe has been fully ionized and most of hydrogen remains to be ionized. Therefore the expected signal of the 21cm line from the IGM also becomes so weak drastically. On the other hand, the signal from ^{3}He is due to the hyperfine transition from ^{3}He II to ^{3}He III, and the spontaneous decay rate of ^{3}He II is ~ 800 times larger than that of H I. We have our sights set on the filamentary structures which is the high-density cloud and must contains a number of baryons and investigate the signals from a filamentary structure.

We found that, contrary to our expectation, the signal of H I is enough high to detect with on-going radio survey such as GMRT. On the other hand, the signal of ^{3}He II is around a few μK at present time. If we observe a filament which is parallel to the line-of-sight at $z \sim 4$, the signal can be detected with some present instruments. However the next generation radio telescope such as SKA can detect the ^{3}He II signal from a filament at present time. The detection of signal of H I or ^{3}He II from IGM at low-redshifts is challenging but only it can definitely probe the baryons hidden in the IGM.

Secondly, We studied the 21cm line from MHs at high-redshifts and the effects of non-vanishing initial isocurvature fluctuations to the structure formation. Such a small halo can not drive the star formation, so it must contain a number of neutral hydrogen. Furthermore there are a lot of such MHs in the Universe at high-redshifts and it should be the dominant sources of the 21cm line.

We calculate the observed 21cm line from MHs and investigate how non-vanishing initial isocurvature fluctuations can affect such signal. We found that the blue-tilted isocurvature spectrum enhance the signal form MHs because such a blue-tilted spectrum generate the density fluctuations in small-scales and it leads to the increase of the number of MHs. However, by contraries, too much contribution of isocurvature fluctuations suppress the signal. Although the density fluctuations in small-scales are still enhanced, the abundance of MHs decrease because of the incorporation processes of MHs into a larger halo.

Furthermore we investigated how well the isocurvature modes can be constrained from the observation the 21cm line from MHs by using the Fisher matrix analysis. The constraint from such a survey alone is not so much tight due to the parameter degeneracies, but by combining with the CMB observation, we could get the significant improvement. The constraints from the observation of MHs via the 21cm line has potential to put a tighter constraint on the blue-tilted isocurvature fluctuations than that from CMB and to distinguish CDM and baryon isocurvature modes, which can not be realized by CMB. If we differentiate these two isocurvature modes, it leads to the probe for the matter generation mechanism and to the deep understanding of the physics in the early Universe.

We hope the studies in this thesis can provide fruitful insight for the application of upcoming data from various radio surveys and the survey strategy for the next generation radio surveys.

Appendix A

Recombination/Ionization Rates and Cooling/Heating Coefficients

We here summarize the recombination and collisional ionization rates, and the cooling function we adopt in this work. We take these values from (Fukugita and Kawasaki, 1994; Mo et al., 2010) and the similar expressions also can be found in (Menzel and Pekeris, 1935; Matsuda et al., 1971; Spitzer, 1978; Black, 1981; Cen, 1992; Verner and Ferland, 1996).

A.1 Recombination and Collisional ionization rates

A.1.1 Collisional ionization

H I $\rightarrow$ H II :

$$\beta_{\rm HI} = 5.85 \times 10^{-11} T^{1/2} \left(1 + T_5^{1/2}\right)^{-1} \exp(-1.578/T_5) \ {\rm cm}^3 \cdot {\rm sec}^{-1} \, . \tag{A.1}$$

He I $\rightarrow$ He II :

$$\beta_{\rm HeI} = 2.38 \times 10^{-11} T^{1/2} \left(1 + T_5^{1/2}\right)^{-1} \exp(-2.853/T_5) \ {\rm cm}^3 \cdot {\rm sec}^{-1} \, . \tag{A.2}$$

He II $\rightarrow$ He III :

$$\beta_{\rm HeII} = 5.68 \times 10^{-12} T^{1/2} \left(1 + T_5^{1/2}\right)^{-1} \exp(-6.315/T_5) \ {\rm cm}^3 \cdot {\rm sec}^{-1} \, . \tag{A.3}$$

A.1.2 Recombination

H II $\rightarrow$ H I : (free $\rightarrow n \geq 1$)

$$\alpha_{\rm HII} = 3.96 \times 10^{-13} T_4^{-0.7} \left(1 + T_6^{0.7}\right)^{-1} \ {\rm cm}^3 \cdot {\rm sec}^{-1} \, . \tag{A.4}$$

He II→ He I : (free → $n \geq 1$)

$$\alpha_{\rm HeII} = 4.31 \times 10^{-10} T_4^{-0.6353}\ {\rm cm}^3 \cdot {\rm sec}^{-1}\,. \tag{A.5}$$

He III→ He II : (free → $n \geq 1$)

$$\alpha_{\rm HeIII} = 2.12 \times 10^{-12} T_4^{-0.7} \left(1 + 0.379 T_6^{0.7}\right)^{-1}\ {\rm cm}^3 \cdot {\rm sec}^{-1}\,. \tag{A.6}$$

A.1.3 Dielectric recombination

He II → He I : (dielectric recombination) (Nussbaumer and Storey, 1983; Osterbrock, 1989)

$$\xi_{\rm HeII} = 6.0 \times 10^{-10} T_5^{-1.5} \exp(-4.7/T_5) \left[1 + 0.3 \exp(-0.94/T_5)\right]\ {\rm cm}^3 \cdot {\rm sec}^{-1}\,. \tag{A.7}$$

A.2 Photoionization rate

Photoionization is the process in which an atom is ionized by the absorption of a photon. The photoionization rate is proportional to the number density of ionizing photons and to the photoionization cross-section $\sigma_{\rm pi}$, and it can be written by

$$\Gamma = \int_{\nu_t}^{\infty} c\, \sigma_{\rm pi}(\nu) \mathcal{N}_\gamma(\nu) d\nu\,, \tag{A.8}$$

where ν_t is the threshold frequency of ionization and $\mathcal{N}_\gamma(\nu)d\nu$ is the number density of photons with frequencies in the rage ν to $\nu + d\nu$, which is related to the energy flux of the radiation field $J(\nu)$ by

$$\mathcal{N}_\gamma(\nu) = \frac{4\imath J(\nu)}{c h_{\rm p} \nu}\,. \tag{A.9}$$

Thus, the photoionization rate depends on the energy flux of the radiation field we need a model of radiation field. We here adopt the model of Haardt and Madau (2012), which takes into account quasars and galaxies, and show the photo-ionization rates of H I, He I and He II in the IGM as a function of redshift in Figure A.1.

A.3 Cooling function

We define the cooling function Λ as;

$$\begin{aligned}\Lambda = \sum_{i={\rm HI,HeI,HeII}} \zeta_i n_e n_i \;+\; \sum_{i={\rm HI,HeI,HeII}} \psi_i n_e n_i \;+\; \sum_{i={\rm HII,HeII,HeIII}} \eta_i n_e n_i \\ +\;\; \omega_{\rm HeII}\, n_e\, n_{\rm HeIII} \;+\; \lambda_{\rm c} \;+\; \theta_{\rm ff}\left(n_{\rm HII} + n_{\rm HeII} + 4 n_{\rm HeIII}\right) n_e\,,\end{aligned} \tag{A.10}$$

where the first term represents the collisional-ionization cooling, the second term represents the collisional excitation cooling, the third term represents the recombination cooling, the fourth term

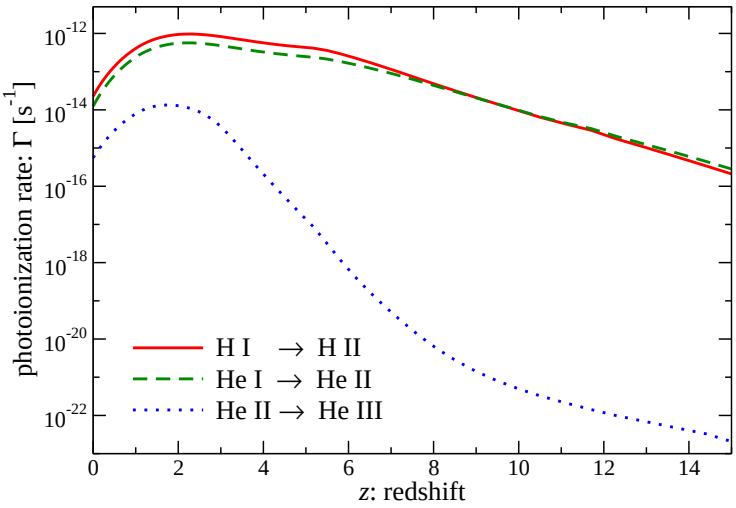

Figure A.1: Photoionization rates of H I, He I and He II in the IGM for the quasars + galaxies model in Haardt and Madau (2012).

represents the dielectron recombination cooling, the fifth term represents the Compton cooling and the last term represents the free-free cooling. The symbols, ζ_i, ψ_i, η_i, and ω_i, represent the each cooling coefficient due to atomic state i, λ_c is the Compton cooling rate, and θ_{ff} is the free-free cooling coefficient. We summarize the detail expressions of these values below.

A.3.1 Collisional ionization cooling

H I :

$$\zeta_{\rm HI} = 1.27 \times 10^{-21} T^{1/2} \left(1 + T_5^{1/2}\right)^{-1} \exp(-1.58/T_5)\ {\rm erg \cdot cm^3 \cdot sec^{-1}}\,. \tag{A.11}$$

He I :

$$\zeta_{\rm HeI} = 9.38 \times 10^{-22} T^{1/2} \left(1 + T_5^{1/2}\right)^{-1} \exp(-2.85/T_5)\ {\rm erg \cdot cm^3 \cdot sec^{-1}}\,. \tag{A.12}$$

He I (2^3S) :

$$\zeta_{\rm HeI,2^3S} = 5.01 \times 10^{-27} T^{-0.1687} \left(1 + T_5^{1/2}\right)^{-1} \exp(-5.53/T_4) n_e n_{\rm HeII}/n_{\rm HeI}\ {\rm erg \cdot cm^3 \cdot sec^{-1}}\,. \tag{A.13}$$

He II :

$$\zeta_{\rm HeII} = 4.95 \times 10^{-22} T^{1/2} \left(1 + T_5^{1/2}\right)^{-1} \exp(-6.31/T_5)\ {\rm erg \cdot cm^3 \cdot sec^{-1}}\,. \tag{A.14}$$

A.3.2 Collisional excitation cooling

H I :

$$\psi_{\rm HI} = 7.5 \times 10^{-19} \left(1 + T_5^{1/2}\right)^{-1} \exp(-1.18/T_5)\ {\rm erg \cdot cm^3 \cdot sec^{-1}}\,. \tag{A.15}$$

He I :

$$\psi_{\rm HeI} = 9.10 \times 10^{-27} T^{-0.1687} \left(1 + T_5^{1/2}\right)^{-1} \exp(-1.31/T_4) n_e n_{\rm HeII}/n_{\rm HeI} \ {\rm erg \cdot cm^3 \cdot sec^{-1}} \,. \tag{A.16}$$

He II :

$$\psi_{\rm HeII} = 5.54 \times 10^{-17} T^{-0.397} \left(1 + T_5^{1/2}\right)^{-1} \exp(-4.73/T_5) \ {\rm erg \cdot cm^3 \cdot sec^{-1}} \,. \tag{A.17}$$

A.3.3 Recombination cooling

H II :

$$\eta_{\rm HII} = 2.82 \times 10^{-26} T_3^{0.3} \left(1 + 3.54 T_6\right)^{-1} \ {\rm erg \cdot cm^3 \cdot sec^{-1}} \,. \tag{A.18}$$

He II :

$$\eta_{\rm HeII} = 1.55 \times 10^{-26} T^{0.3647} \ {\rm erg \cdot cm^3 \cdot sec^{-1}} \,. \tag{A.19}$$

He III :

$$\eta_{\rm HeIII} = 1.49 \times 10^{-25} T^{0.3} \left(1 + 0.885 T_6\right)^{-1} \ {\rm erg \cdot cm^3 \cdot sec^{-1}} \,. \tag{A.20}$$

A.3.4 Dielectronic recombination cooling

He II :

$$\omega_{\rm HeII} = 1.24 \times 10^{-13} T^{-1.5} \left(1 + 0.3 \exp(-9.4/T_4)\right)^{-1} \exp(-4.7/T_5) \ {\rm erg \cdot cm^3 \cdot sec^{-1}} \,. \tag{A.21}$$

A.3.5 Free-free cooling

$$\theta_{\rm ff} = 1.42 \times 10^{-27} g_{\rm ff} \, T^{1/2} \,, \tag{A.22}$$

where $g_{\rm ff}$ is the mean Gaunt factor and the values of $g_{\rm ff}$ are between 1.1 and 1.5 for $T = 10^4$-10^8 K (Spitzer, 1978) and we adopt the value of $g_{\rm ff} = 1.1$ in this paper.

A.3.6 Compton cooling

$$\lambda_{\rm c} = 4 k_{\rm B} (T - T_\gamma) \frac{\pi^2}{15} \left(\frac{k_{\rm B} T_\gamma}{\hbar_{\rm p} c}\right)^3 \left(\frac{k_{\rm B} T_\gamma}{m_e \, c^2}\right) n_e \, \sigma_{\rm T} \, c \,, \tag{A.23}$$

where $\sigma_{\rm T}$ denotes the cross-section for the Thomson scattering.

A.4 Heating function

The photoelectric absorption process creates a photoelectron with kinetic energy K:

$$X^{+(i)} + h_{\rm p}\nu \rightarrow X^{+(i+1)} + e^- + K \,. \tag{A.24}$$

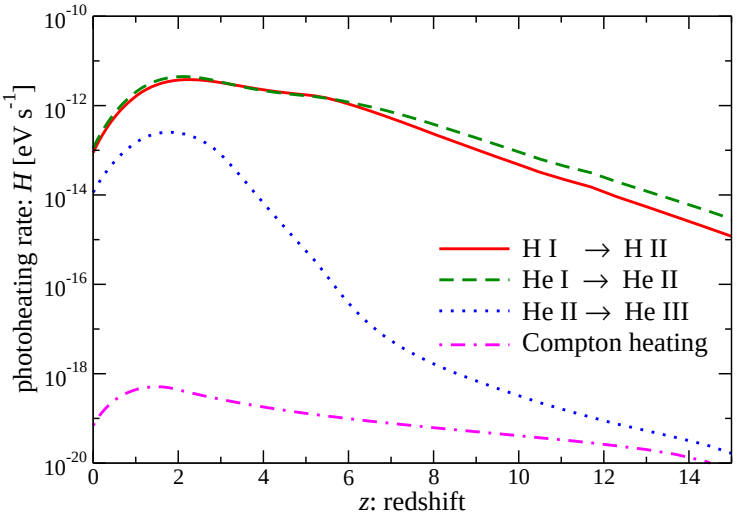

Figure A.2: Photo-heating rates per ion of H I, He I, He II and the Compton heating rates for the quasars and galaxies model of Haardt and Madau (2012).

The probability per unit time for photoionization is given by Eq. A.8. each photoionization event injects a photoelectron with kinetic energy, $h_{\rm p}\nu - h_{\rm p}\nu_t$, in to the plasma. Hence, the heating rate per unit volume from the photoionization process is given by

$$\mathcal{H} = n(X^{+(i)}) \int_{\nu_t}^{\infty} c\,\sigma_{\rm ph}(\nu)\mathcal{N}(h_{\rm p}\nu - h_{\rm p}\nu_t)d\nu\,. \tag{A.25}$$

Therefore, the photoionization process also depends on the energy flux of radiation field through $\mathcal{N}_\gamma(\nu)$.

On the other hand, the photons and the gas couple through Compton heating. The Compton scattering between an electron and a photon transfers energy from the photon to the electron if the gas is ionized and has a temperature lower than the effective Compton temperature of the radiation field. As a result, the gas gets heated through Compton scattering and such a heating process is a non-negligible process of heating for very underdense, highly ionized regions.

More detail treatment for the photoionization and the Compton heating processes can be found in e.g. Draine (2011); Rybicki and Lightman (1986); Spitzer (1998). We show the photo-heating rates per ion of H I, He I, He II for the quasars and galaxies model of Haardt and Madau (2012) as a function of redshift in Figure A.2. The Compton heating rate is also plotted in the same panel.

Appendix B

Truncated Isothermal Sphere (TIS)

In Chapter 5, we have assumed each minihalo is in virial and hydrostatic equilibrium and adopt a non-singular, truncated isothermal sphere (TIS) (Shapiro et al., 1999; Iliev and Shapiro, 2001; Iliev et al., 2002) as a model for the halo profiles.

We here review the TIS halo model following Shapiro et al. (1999) and show the convenient analytic formulae provide by Iliev and Shapiro (2001) in Sec. B.5.

B.1 The Top-Hat Model

B.1.1 Before collapse: the exact nonlinear solution

The spherical top-hat model is an uncompensated spherical perturbation of uniform overdensity within a finite radius (Gunn and Gott, 1972). We here consider top-hat perturbations in the Einstein de Sitter (EdS) model.

We can describe the evolution of the density inside the top-hat solely in terms of its overdensity δ with respect to the background, because the density inside the top-hat stays uniform during collapse. The solution for the linear evolution of the density perturbation $\delta_L(t)$ is described by the following parametric form (e.g., (Padmanabhan, 1993))

$$\delta = \frac{9}{2}\frac{(\theta - \sin\theta)^2}{1-\cos\theta)^3} - 1\,, \tag{B.1}$$

and

$$\delta_L = \frac{3}{5}\left(\frac{3}{4}\right)^{2/3}(\theta - \sin\theta)^{2/3}\,. \tag{B.2}$$

The critical density contrast $\delta_{\rm c}$ is defined as the linear solution extrapolated to the epoch at which the nonlinear solution predicts an infinite density. We here define $z_{\rm coll}$ as the redshift which corresponds to the epoch of infinite collapse, at which $\delta = \infty$, at time $t_{\rm coll}$.

B.1.2 After collapse: uniform sphere in virial equilibrium

A perfectly symmetric top-hat collapse results does not lead to the formation of virialized structures. To overcome such a problem, the processes like violent relaxation is usually assumed, and which leads to form a static, virialized structure. Assuming that the total energy is conserved during the collapse, we can connect the initial top-hat to the final state.

We solve for the final radius $r_{\rm vir}$ of the virialized sphere by applying the virial theorem to the final state. The conserved total energy E of the sphere is described in terms of the radius r_m at maximum expansion. When the sphere expands maximumly, the sphere is cold and at rest and its energy is entirely gravitational potential energy. Therefore, the energy for a uniform sphere with mass M_0 and radius r_m at this point is given by

$$E = W_m = \frac{3}{5} G M_0^2 r_m \,. \tag{B.3}$$

After collapse, when the system settles down to a virial equilibrium, the total potential energy is given by

$$W_{\rm vir} = \frac{3}{5} G M_0^2 r_{\rm vir} \,. \tag{B.4}$$

According to the virial theorem, the kinetic and gravitational potential energies are related by

$$3(\gamma - 1)K + W = 0 \,, \tag{B.5}$$

where $K = U_{\rm th} + T_{\rm kin}$, $U_{\rm th}$ and $T_{\rm kin}$ are the thermal and kinetic energy, respectively, and γ is the ratio of specific heats and we take $\gamma = 5/3$. The conservation of energy, $E = K + W$, leads to $E = -W/2$ and the total energy is related to the virial radius according to

$$E = -\frac{3}{10} \frac{G M_0^2}{r_{\rm vir}} \,, \tag{B.6}$$

Then, equating the total energy E in Eqs. (B.3) and (B.6) yields $r_{\rm vir} = r_m/2$. The kinetic energy in the virialized state and the thermal energy are expressed by

$$K_{\rm vir} = E - W_{\rm vir} = \frac{3}{10} \frac{G M_0^2}{r_{\rm vir}} \,, \tag{B.7}$$

$$U_{\rm th} = \frac{3}{2} \frac{k_{\rm B} T}{m} M_0 \,, \tag{B.8}$$

where m is the mean mass per gas particle. If $m_{\rm H}$ is the mass of a hydrogen atom, then $m = \mu m_{\rm H}$ where μ is the mean molecular weight. Since the kinetic energy is the energy of internal motions only, which leads to $T_{\rm kin} = 0$, the equivalent virial temperature for the standard uniform sphere (SUS) model is

$$T_{\rm SUS} = \frac{1}{5} \frac{G M_0 m}{k_{\rm B} r_{\rm vir}} = \frac{2}{5} \frac{G M_0 m}{k_{\rm B} r_m} \,. \tag{B.9}$$

For the case of a collisionless gas, the virial temperature $T_{\rm vir}$ can be replaced by the virial velocity

dispersion,

$$\sigma_V^2 = \frac{\langle v^2 \rangle}{3} = \frac{k_{\rm B} T_{\rm vir}}{m} \,. \tag{B.10}$$

This approach is commonly used to estimate the virial temperature and radius, but it is not a realistic model. A more realistic approach is to assume a final state of hydrostatic equilibrium, which corresponds to the state with an isotropic Maxwellian velocity distribution in the case of collisionless particles, instead of the isothermality and the uniform density.

B.2 Isothermal Spheres

When we describe the virialized object as an isothermal sphere in hydrostatic equilibrium, we treat is in the usual non-cosmological way (Binney and Tremaine, 1987). Because the final virialized object is decoupled from the expanding cosmological background from which which it condensed.

The Poisson equation, $\nabla^2 \Phi = 4\pi G \rho$, for the gravitational potential in the case of spherical symmetry is

$$\frac{1}{r^2} \frac{d}{dr} \left(r^2 \frac{d\Phi}{dr} \right) = 4\pi G \rho \,. \tag{B.11}$$

Then, the hydrostatic equilibrium equation, $\nabla = \rho \boldsymbol{g}$, where $g = -\nabla \Phi$, becomes

$$\frac{k_{\rm B} T}{m} \frac{d\rho}{dr} = -\rho \frac{GM(r)}{r^2} \,, \tag{B.12}$$

where $M(r)$ is the mass inside radius r. Multiplying above equation by r^2/ρ, and taking the derivative with respect to r, we obtain

$$\frac{d}{dr} \left(r^2 \frac{d(\ln \rho)}{dr} \right) = -4\pi \frac{Gm}{k_{\rm B} T} r^2 \rho \,. \tag{B.13}$$

In the case of collisionless particles, the the equilibrium velocity distribution of the particles is given by a Maxwellian distribution,

$$f(v) = \frac{\rho_0}{(2\pi\sigma_V^2)^{3/2}} \exp \left(\frac{\Phi - v^2/2}{\sigma_V^2} \right) \,, \tag{B.14}$$

where ρ_0 is the central density, if we take $\Phi(r = 0) = 0$, and σ_V is the one-dimensional velocity dispersion. After integrating over velocity, we obtain

$$\rho = \int f(v) d\boldsymbol{v} = \rho_0 \exp \left(\frac{\Phi}{\sigma_v^2} \right) \,, \tag{B.15}$$

and by substituting into Eq. (B.11), we get

$$\frac{d}{dr} \left(r^2 \frac{d(\ln \rho)}{dr} \right) = -\frac{4\pi}{\sigma_V^2} G \rho r^2 \,. \tag{B.16}$$

Then, we obtain the mean squared velocity,

$$\langle v^2 \rangle = 3\sigma_V^2 \,, \tag{B.17}$$

and the equivalent temperature can be calculated from

$$\frac{\langle v^2 \rangle}{2} = \frac{3}{2}\frac{k_{\rm B}T}{m} \,. \tag{B.18}$$

To make the non-dimensional equation, we introduce new dimensionless variables

$$\tilde{\rho} = \tilde{\rho}\rho_0 \,, \quad \zeta = \frac{r}{r_0} \,, \tag{B.19}$$

where ρ_0 is the central density and r_0 is defined as

$$r_0 = \sigma_V / \sqrt{4\pi G \rho_0} \,. \tag{B.20}$$

Then, Eq. (B.16) becomes

$$\frac{d}{d\zeta}\left(\zeta^2 \frac{d(\ln\tilde{\rho})}{d\zeta}\right) = -\tilde{\rho}\zeta^2 \,. \tag{B.21}$$

A simple solution which satisfies above equation is that of a singular isothermal sphere (SIS), which is often used in models due to to its simplicity;

$$\rho(r) = \frac{\sigma_V^2}{2\pi G r^2} \,, \tag{B.22}$$

$$\sigma_V^2 = \frac{1}{2}\frac{GM(r)}{r} = \text{const.} \,. \tag{B.23}$$

For more realistic model, which have a core, i.e., $r_0 \neq 0$, we must solve above equation with boundary conditions as follows;

$$\tilde{\rho}(0) = 1 \,, \quad \frac{d\tilde{\rho}}{d\zeta}(0) = 0 \,. \tag{B.24}$$

To describe some realistic finite structure in terms of this model, we must truncate the sphere at some radius, r_t, because the isothermal sphere has infinite mass. The total mass of the isothermal sphere M_0 is given by

$$M_0 = M(r_t) = \int_0^{r_t} 4\pi\rho(r) r^2 dr = 4\pi\rho_0 r_0^3 \tilde{M}(\zeta_t) \,, \tag{B.25}$$

where $\zeta_t = r_t/r_0$ and $\tilde{M}(\zeta_t)$ is the dimensionless mass, which is defined by

$$\tilde{M}(\zeta_t) \equiv \frac{M(r_t)}{4\pi r_0^3 \rho_0} = \int_0^{\zeta_t} \tilde{\rho}(\zeta)\zeta^2 d\zeta \,. \tag{B.26}$$

Finally, we obtain

$$\sigma_V^2 = G(4\pi\rho_0)^{1/3}\left(\frac{M_0}{\tilde{M}_t}\right)^{2/3}, \tag{B.27}$$

$$T = \frac{Gm}{k_{\rm B}}(4\pi\rho_0)^{1/3}\left(\frac{M_0}{\tilde{M}_t}\right)^{2/3}, \tag{B.28}$$

where we newly define $\tilde{M}_t \equiv \tilde{M}(\tilde{\zeta}_t)$. However, the requirement of a truncation radius leads to the necessity of an external pressure to keep the system in equilibrium. Therefore a significant correction to the form of the virial theorem stated here is required.

B.3 The Virial Theorem for TIS

We here consider the general isothermal sphere density profile and add a correction by including an external pressure to keep the system in equilibrium. From the ideal gas low, the pressure inside as a function of the radius is given by

$$p(r) = \frac{k_{\rm B}T}{m}\rho(r) = \sigma^2\rho(r)\,, \tag{B.29}$$

and at the outer edge, $r = r_t$, $p_t = p(r_t) = \sigma^2\rho(r_t)$. The mean pressure inside the sphere is given by

$$\bar{\rho} = \frac{\int pdV}{\int dV} = \frac{3\int_0^{\zeta_t}\tilde{\rho}(\zeta)\zeta^2 d\zeta}{\zeta_t^3\tilde{\rho}(\zeta_t)}p_t = \frac{3\tilde{M}(\zeta_t)}{\zeta_t^3\tilde{\rho}(\zeta_t)}p_t \equiv \alpha(\zeta_t)p_t \tag{B.30}$$

where $\zeta_t \equiv r_t/r_0$. The limit $\zeta_t = \infty$. Hereafter we puts α as $\alpha = \alpha(\zeta_t)$, c.f., $\alpha = 3$ leads to the case of a singular isothermal sphere (SIS).

The virial theorem for a static sphere in the presence of a surface pressure p_t reads

$$3(\gamma-1)K + W + S_p = 0\,, \tag{B.31}$$

where W is the gravitational potential energy, K is just $U_{\rm th}$, thermal energy, and S_p is the surface pressure term. The thermal energy for a gas with a ratio of specific heats $\gamma = 5/3$ is given by

$$U_{\rm th} = \frac{1}{\gamma-1}\int pdV = \frac{3}{2}\alpha(\zeta_t)p_tV\,, \tag{B.32}$$

where V is the total volume. The surface term is given by

$$S_p = -\int p\,\boldsymbol{r}\cdot d\boldsymbol{S}\,. \tag{B.33}$$

Hence, according to the virial theorem, the gravitational potential energy term is given by

$$W = -2U_{\rm th} - S_p = -2\frac{\alpha-1}{\alpha}U_{\rm th}\,, \tag{B.34}$$

and the total energy is

$$E = \frac{2-\alpha}{\alpha} U_{\rm th} \,. \tag{B.35}$$

In order for the halo to be bound, the condition that $E < 0$ (and $U_{\rm th} > 0$) leads to $\alpha > 2$. Then, the virial temperature of the isothermal sphere is

$$T_{\rm TIS} = \frac{2\alpha}{5(\alpha-2)} \frac{GM_0 m}{k_{\rm B} r_m} \,. \tag{B.36}$$

Since $\alpha/(\alpha-1) > 1$ for any α, the temperature $T_{\rm TIS}$ is always higher than the standard value for a uniform sphere $T_{\rm SUS}$. The virial radius $v_{\rm vir}$ in this case is thus the size of the truncated isothermal sphere, $r_{\rm vir} = r_t$.

For comparison with the non-singular TIS model, we calculate the virial temperature for a truncated singular isothermal sphere (SIS), which is algebraically simpler and whose results can be obtained analytically. According to the ideal gas low and $\rho(r) = \sigma^2/2\pi G r^2$, the pressure at radius r is given by

$$p(r) = p_t \left(\frac{r}{r_t} \right)^{-2} \,, \tag{B.37}$$

where the boundary pressure at $r = r_t$ is given by $p_t = \sigma^2 \rho_t = \sigma^4/2\pi G r_t^2$. The average pressure inside the truncated isothermal sphere is then, $\bar{p} = 3p_t$, i.e., with $\alpha = 3$. The thermal energy and the potential energy in this case are given by

$$U_{\rm th} = \frac{3}{2} \int p dV = \frac{3}{4} \frac{GM_0^2}{r_t} \tag{B.38}$$

$$W = -2U_{\rm th} - S_p = -\frac{GM_0^2}{r_t} \tag{B.39}$$

with the surface pressure term in the virial theorem equation given by

$$S_p = -\int p \boldsymbol{r} \cdot d\boldsymbol{S} = -4\pi r_t^3 p_t = -\frac{1}{2} \frac{GM_0^2}{r_t} \,. \tag{B.40}$$

Then, the total energy becomes

$$E = U_{\rm th} + W = -\frac{1}{4} \frac{GM_0^2}{r_t} \,. \tag{B.41}$$

The SIS virial temperature is given by

$$T_{\rm SIS} = \frac{6}{5} \frac{GM_0 m}{k_{\rm B} r_m}. \tag{B.42}$$

Figure B.1 shows the comparisons of the postcollapse equilibrium density profiles and their logarithmic slopes for TIS, SIS and SUS models. A plot of $\rho/\rho_{\rm SUS}$ as a function of normalized radius r/r_m demonstrates the the significant differences of density profiles from that of SUS

model.

B.4 The Minimum-Energy Solution

Although the mass and total energy of the top-hat are conserved through collapse and virialization, the solution is not uniquely determined. Even for any truncated isothermal sphere of mass M_0 which confined by a given external pressure p_t, we can uniquely identify a special value of the truncated radius ζ_t or equivalently of the total energy E. In order to find a unique solution, following Ansatz is adopted; such a "minimum-energy solution" is the unique TIS solution preferred in nature as the outcome of the virialization of the sphere in the presence of a fixed external pressure.

The result so far is for the EdS universe ($\Omega_0 = 1$, $\Omega_{\Lambda 0} = 0$). Iliev and Shapiro (2001) generalized the results of Shapiro et al. (1999) to the case of a low-density universe, either open and matter dominated ($\Omega_0 < 1$, $\Omega_{\Lambda 0} = 0$), or flat with a cosmological constant ($\Omega_0 = 1 - \Omega_{\Lambda 0}$). In the presence of the cosmological constant or dark energy, the final virialized objects also decouples from the expanding cosmological background from which is condensed, but it continues to be affected by the cosmological constant or dark energy because of the modification that component causes to the gravity force.

For the case with a cosmological constant, the differences with respect to the EdS solution for the TIS model is the necessarily to take proper account of non-zero Λ for the solution in the spherical top-hat problem, the virial theorem, the conservation of energy, and the isothermal Lane-Emden equation. Figure B.2 shows the effects of a cosmological constant for the modified isothermal Lane-Emden spheres. According to (Iliev and Shapiro, 2001), we summarize the minimum-energy solution for the TIS model as follows.

The dimensional parameters for the dimensionless TIS solution are specified for a given mass M_0 and collapse redshift $z_{\rm coll}$). For a given θ, the mean overdensity of the virialized object in the TIS model with respect to the critical density of the universe at $z_{\rm coll}$ is given by

$$\Delta_{\rm c,TIS} \equiv \frac{\bar{\rho}}{\rho_{\rm crit}(z_{\rm coll})} = \frac{\Omega_0\, a_0^3}{\theta\, \eta_{\rm TIS}^3(\theta)} \left[\frac{\rho_{\rm crit}(z_{\rm coll})}{\rho_{\rm crit,0}}\right]^{-1} , \tag{B.43}$$

where $\Omega_0\, a^3 = \Omega_{\Lambda 0}$ for $\Omega_0 + \Omega_{\Lambda 0} = 1$ and the corresponding overdensity for the standard uniform sphere $\Delta_{\rm c,SUS}$ are related as $\Delta_{\rm c,TIS} = (\eta_{\rm SUS}/\eta_{\rm TIS})^3 \Delta_{\rm c,SUS}$. The dependence of θ on collapse redshift $z_{\rm coll}$ for a given background cosmology is expressed by θ is given by

$$\theta = \frac{\Omega_0\, a_0^3}{\Delta_{\rm c,SUS}\, \eta_{\rm SUS}^3} \left[\frac{h(z_{\rm coll})}{h}\right]^{-2} . \tag{B.44}$$

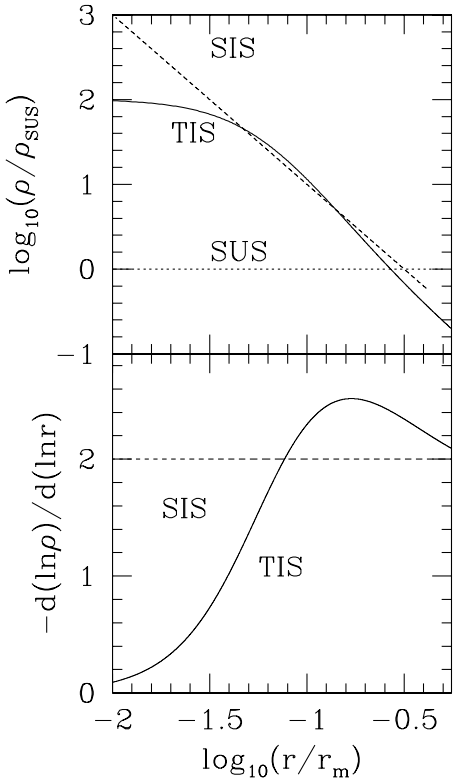

Dimensionless Parameters

	SUS	SIS	TIS
			$\theta = 1 - 0.5$
$\eta/\eta_{\rm SUS}$	1	0.833	1.11-1.04
$T/T_{\rm SUS}$	1	3	2.16-2.26
ρ_0/ρ_t	1	∞	514-575
$\langle\rho\rangle/\rho_t$	1	3	3.73-3.59
r_t/r_0	-NA-	∞	29.4-31.7
$\Delta_{\rm c}/\Delta_{\rm c,SUS}$	1	$\left(\frac{6}{5}\right)^3 = 1.728$	1.36-1.12
$K/\lvert W\rvert$	0.5	0.75	0.683-0.707

Figure B.1: The comparisons of the postcollapse equilibrium density profiles for TIS (solid line), SIS (dashed line) and SUS (dotted line); this figure is taken from Shapiro et al. (1999). The radius is in units of the radius of the tophat at maximum expansion for each model and all densities are plotted in units of the postcollapse density of the SUS approximation, i.e., $18\pi^2\rho(t_{\rm coll})$. The right table summarizes the dimensionless parameters for each model.

For a given mass M_0 and $\Delta_{\rm c,TIS}$ can be expressed as follows:

$$r_t = \left(\frac{3M_0}{4\pi\Delta_{\rm c,TIS}\rho_{\rm crit}(z_{\rm coll})}\right)^{1/3}, \tag{B.45}$$

$$= 187.2 \times \left(\frac{M}{10^{12}M_\odot}\right)^{1/3} F(z_{\rm coll})^{-1} h^{-2/3}{\rm kpc}\ ,$$

$$r_{\rm m} = \frac{r_t}{\eta_{\rm TIS}} = \frac{\zeta_t}{\eta_{\rm TIS}} r_0\,, \tag{B.46}$$

$$= 337.7 \times \left(\frac{M}{10^{12}M_\odot}\right)^{1/3} F(z_{\rm coll})^{-1} h^{-2/3}{\rm kpc}\ ,$$

$$r_0 = 6.367 \times \left(\frac{M}{10^{12}M_\odot}\right)^{1/3} F(z_{\rm coll})^{-1} h^{-2/3}{\rm kpc}\ . \tag{B.47}$$

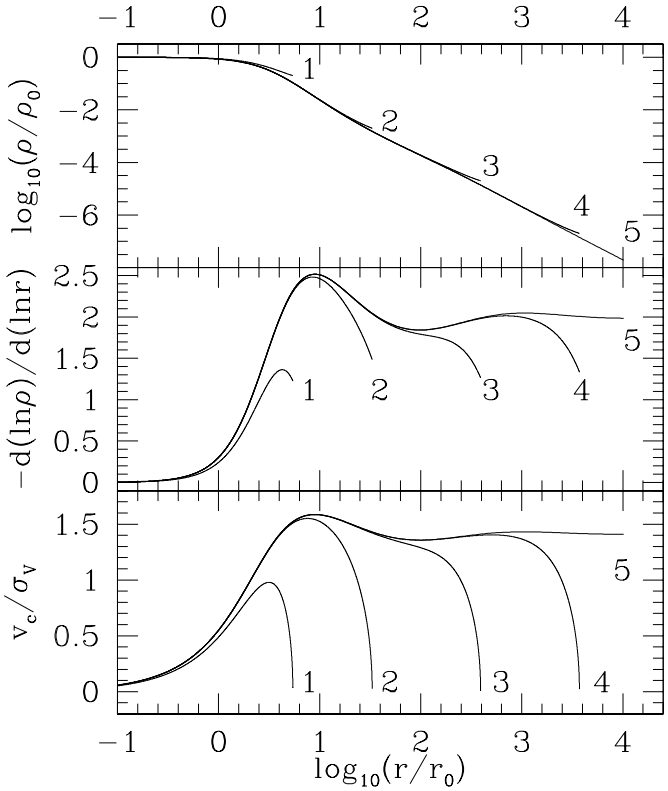

Figure B.2: The effects of a cosmological constant for the modified isothermal Lane-Emden spheres; this figure is taken from Iliev and Shapiro (2001). Each panel shows the density profile in units of the central density ρ_0, the logarithmic slopes of these density profiles and the circular velocity profiles $v_{\rm c}$ normalized by the velocity dispersion of the halo $\sigma_{\rm V}$ versus dimensionless radius normalized by the core radius r_0, from top to bottom. Each label represents the abundance of a cosmological constant; $\tilde{\rho}_\Lambda = 0.1$ (label 1), $\tilde{\rho}_\Lambda = 10^{-3}$ (label 2), $\tilde{\rho}_\Lambda = 10^{-5}$ (label 3), $\tilde{\rho}_\Lambda = 10^{-7}$ (label 4), and $\tilde{\rho}_\Lambda = 0$ (label 5), respectively. Each plot extends out to its natural cut-off at $\rho = 2\rho_\Lambda$, except the matter-dominated one (curve 5).

$$\rho_0 = \frac{\zeta_t^3}{3\tilde{M}_t}\bar{\rho} = \frac{\zeta_t^3}{3\tilde{M}_t}\Delta_{\rm c,TIS}\,\rho_{\rm crit}(z_{\rm coll})\,, \tag{B.48}$$

$$= 3.382\times10^{-25}F(z_{\rm coll})^3\,h^2\,{\rm g\,cm^{-3}}\,,$$

$$\sigma_{\rm V}^2 = 4\pi G\rho_0\,r_0^2 = \left[\frac{4\pi}{3}\Delta_{\rm c,TIS}\,\rho_{\rm crit}(z_{\rm coll})\right]^{1/3}\frac{\zeta}{\tilde{M}_t}GM_0^{2/3}\,, \tag{B.49}$$

$$= 1.098\times10^4\left(\frac{M}{10^{12}M_\odot}\right)^{2/3}F(z_{\rm coll})\,h^{2/3}\,{\rm km^2 s^{-2}}\,,$$

$$T = \frac{m}{k_{\rm B}}\sigma_{\rm V}^2 \tag{B.50}$$

$$= 7.843\times10^5\left(\frac{\mu}{0.59}\right)\left(\frac{M}{10^{12}M_\odot}\right)^{2/3}F(z_{\rm coll})\,h^{2/3}\,{\rm K}\,,$$

$$v_{\rm c}(r) = \left[\frac{GM(r)}{r}\left(1-2\frac{\rho_\Lambda}{\rho(r)}\right)\right]^{1/2}\,, \tag{B.51}$$

where

$$F(z_{\rm coll}) \equiv \left[\frac{h(z_{\rm coll})}{h}\right]^2 \frac{\Delta_{\rm c,TIS}(z_{\rm coll},\Omega_{\Lambda 0})}{\Delta_{\rm c,TIS}(\Omega_{\Lambda 0}=0)} = \left[\frac{\Omega_0}{\Omega(z_{\rm coll})}\frac{\Delta_{\rm c,SUS}}{18\pi^2}\right]^{1/3}(1+z_{\rm coll})\ . \tag{B.52}$$

Here μ is the mean molecular weight, where $\mu = 0.59(1.22)$ for an ionized(neutral gas of H and He with [He]/[H]=0.08 by number.

B.5 Analytic Fitting Formulae

A convenient set of analytic fitting formulae for the dimensionless TIS parameters, such as ζ_t and $\eta_{\rm TIS}$, are given for two overlapping intervals of θ, with different fractional errors.

In the range, $0 \le \theta \le 0.123$, the fits are given by

$$\zeta_t = 29.40031 + 11.4652\,\theta - 13.8428\,\theta^2 - 12.8453\,\theta^3\ , \tag{B.53}$$

$$\alpha = 3.7296 - 0.866069\,\theta + 1.92742\,\theta^2 - 1.70326\,\theta^3\ , \tag{B.54}$$

$$\eta_{\rm TIS} = 0.554384 - 0.45529\,\theta + 0.21258\,\theta^2 + 0.02128\,\theta^3\ , \tag{B.55}$$

$$\tilde{M}_t = 61.485 + 23.8887\theta - 32.9854\theta^2 - 14.0272\theta^3\,. \tag{B.56}$$

The relative errors of these fits are < 0.01 per cent.

The fits in the full allowed range, $0 \le \theta \le 0.5$, are given by

$$\zeta_t = 29.38931 + 12.0474\theta - 20.752\theta^2 + 11.732\theta^3\ , \tag{B.57}$$

$$\alpha = 3.72913 - 0.843068\,\theta + 1.71017\,\theta^2 - 1.20963\,\theta^3\ , \tag{B.58}$$

$$\eta_{\rm TIS} = 0.554437 - 0.45804\theta + 0.23999\theta^2 - 0.04279\theta^3\ , \tag{B.59}$$

$$\tilde{M}_t = 61.4683 + 24.782\theta - 43.8578\theta^2 + 25.8869\theta^3\,. \tag{B.60}$$

The relative errors of these fits are < 0.1 per cent.

The analytic fit to the TIS density profile is obtained by

$$\rho(\zeta) + \frac{A}{a^2+\zeta^2} - \frac{B}{b^2+\zeta^2}\,, \tag{B.61}$$

where $\zeta = r/r_0$ for $\zeta \le \zeta_t$ with $(A,\, a^2, B,\, b^2)_{\rm TIS} = (21.38, 9.08, 19.81, 14.62)$. The fit has an accuracy of better than 3 per cent.

The corresponding fit to the TIS halo circular velocity profile, i.e., the rotation curve, is obtained by

$$v_{\rm c}(r) = \sigma_{\rm V}\left[A - B + \frac{r_0}{r}\left\{bB\arctan\left(\frac{r}{br_0}\right) - aA\arctan\left(\frac{r}{ar_0}\right)\right\}\right]^{1/2}\ . \tag{B.62}$$

This fit to $\sigma_{\rm c}/\sigma_{\rm V}$ is good to < 1 per cent for $r < 2r_t/3$, while at larger radii the error could be larger but that is ≤ 6 per cent at r_t.

Appendix C

Fisher matrix analysis

For a given data, estimating how well model parameters can be determined is often required not only in cosmology but also in various fields. Following (Tegmark et al., 1997), we here summarize the Fisher matrix analysis (Fisher, 1935), which is often utilized in the cosmological field.

C.1 Fisher Information Matrix

In cosmological field, the Fisher matrix analysis is often used to investigate how well model parameters can be determined from the assumed observation. The Fisher matrix analysis is one of the parameter estimation methods based on the maximum likelihood estimation method. The accuracy of determination of parameters are estimated by defining the quantity corresponding to the curvature of the maximum likelihood function in the parameter space, which is called the Fisher Information Matrix.

We define the vectors for M model parameters and N data as follows;

$$\text{parameter vector (theory)} \quad : \quad \boldsymbol{\theta} = (\theta_1, \theta_2, \cdots, \theta_M). \tag{C.1}$$

$$\text{data vector (observation)} \quad : \quad \boldsymbol{d} = (d_1, d_2, \cdots, d_N). \tag{C.2}$$

where $\boldsymbol{\theta}$ and $\boldsymbol{d}$ are the theoretical value the observed value, respectively. When we assume a future observation, the data vector is given by $\boldsymbol{d} = \boldsymbol{S}_{\rm th} + \boldsymbol{N}_{\rm ex}$, with theoretical signal $\boldsymbol{S}_{\rm th}$ and noise assumed from a observation $\boldsymbol{N}_{\rm ex}$, which include the information of the future observation.

Then, we consider the probability of obtaining the theoretical value which corresponds to the model parameters $\boldsymbol{\theta}$ when a data set $\boldsymbol{d}$ is given. If we assume that the distributions of parameters follow the Gaussian distribution, the probability can be given by

$$P[\boldsymbol{d}\,|\,\boldsymbol{\theta}] \equiv L(\boldsymbol{d};\,\boldsymbol{\theta}) = \frac{1}{\sqrt{2\pi\,(\det \boldsymbol{C})}} \exp\left[-\frac{1}{2}(\boldsymbol{d}-\boldsymbol{\mu})C^{-1}(\boldsymbol{d}-\boldsymbol{\mu})^T\right], \tag{C.3}$$

where L is the likelihood function and the logarithmic likelihood function is defined by $\mathcal{L} \equiv -\ln L$. $\boldsymbol{\mu}$ and $\boldsymbol{C}$ are respectively the mean value (theoretical value) and its covariance matrix for the

given $\boldsymbol{\theta}$;

$$\boldsymbol{C} = \langle (\boldsymbol{d} - \boldsymbol{\mu})(\boldsymbol{d} - \boldsymbol{\mu})^T \rangle \,. \tag{C.4}$$

In the same manner, the data vector $\boldsymbol{D}$ is defined by

$$\boldsymbol{D} \equiv (\boldsymbol{d} - \boldsymbol{\mu})(\boldsymbol{d} - \boldsymbol{\mu})^T \,. \tag{C.5}$$

Finally, we define the quantity which corresponds to the curvature of logarithmic likelihood $\mathcal{L}$ in the parameter space as follow;

$$\boldsymbol{F}_{ij} \equiv \left\langle \frac{\partial^2 \mathcal{L}}{\partial \theta_i \partial \theta_j} \right\rangle \,, \tag{C.6}$$

where $\boldsymbol{F}_{ij}$ is called the Fisher Information Matrix.

From Eq. (C.3), the logarithmic likelihood $\mathcal{L}$ can be rewritten as

$$2\mathcal{L} = \ln(2\pi) + \ln(\det \boldsymbol{C}) + (\boldsymbol{d} - \boldsymbol{\mu})\boldsymbol{C}^{-1}(\boldsymbol{d} - \boldsymbol{\mu})^T \tag{C.7}$$

Furthermore, $\ln \det \boldsymbol{C} = \mathrm{Tr} \ln \boldsymbol{C}$ leads to

$$2\mathcal{L} = \ln(2\pi) + \mathrm{Tr}[\ln \boldsymbol{C} + \boldsymbol{C}^{-1}\boldsymbol{D}] \,. \tag{C.8}$$

To drive the r.h.s in Eq. (C.6), we differentiate partially $\mathcal{L}$ with a parameter θ_i and define the differential operation as follow;

$$\boldsymbol{C}_{,i} \equiv \frac{\partial \boldsymbol{C}}{\partial \theta_{,i}} \,. \tag{C.9}$$

In the same manner, we describe the same notations for $\boldsymbol{D}$ and $\mathcal{L}$. Adopting the following relations for the differential operation of matrix;

$$(\boldsymbol{C}^{-1})_{,i} = -\boldsymbol{C}^{-1}\boldsymbol{C}_{,i}\boldsymbol{C}^{-1} \,, \tag{C.10}$$

$$(\ln \boldsymbol{C})_{,i} = \boldsymbol{C}^{-1}\boldsymbol{C}_{,i} \tag{C.11}$$

the differential operation of the likelihood function can be written by

$$2\mathcal{L}_{,i} = \mathrm{Tr}[\boldsymbol{C}^{-1}\boldsymbol{C}_{,i} - \boldsymbol{C}^{-1}\boldsymbol{C}_{,i}\boldsymbol{C}^{-1}\boldsymbol{D} + \boldsymbol{C}^{-1}\boldsymbol{D}_{,i}], \tag{C.12}$$

and

$$\begin{aligned} 2\mathcal{L}_{,ij} = \mathrm{Tr}[&-\boldsymbol{C}^{-1}\boldsymbol{C}_{,i}\boldsymbol{C}^{-1}\boldsymbol{C}_{,j} + \boldsymbol{C}^{-1}\boldsymbol{C}_{,ij} + \boldsymbol{C}^{-1}(\boldsymbol{C}_{,i}\boldsymbol{C}^{-1}\boldsymbol{C}_{,j} + \boldsymbol{C}_{,j}\boldsymbol{C}^{-1}\boldsymbol{C}_{,i})\boldsymbol{C}^{-1}\boldsymbol{D} \\ &-\boldsymbol{C}^{-1}(\boldsymbol{C}_{,i}\boldsymbol{C}^{-1}\boldsymbol{D}_{,j} + \boldsymbol{C}_{,j}\boldsymbol{C}^{-1}\boldsymbol{D}_{,i}) - \boldsymbol{C}^{-1}\boldsymbol{C}_{,ij}\boldsymbol{C}^{-1}\boldsymbol{D} + \boldsymbol{C}^{-1}\boldsymbol{D}_{,ij} \,. \end{aligned} \tag{C.13}$$

If the true parameter $\boldsymbol{\theta} = \boldsymbol{\Theta}$ is given, the theoretical value $\boldsymbol{\mu}$ and the covariance matrix $\boldsymbol{C}$ are written as $\langle \boldsymbol{d} \rangle = \boldsymbol{\mu}$ and $\langle \boldsymbol{d}\boldsymbol{d}^T \rangle = \boldsymbol{C} + \boldsymbol{\mu}\boldsymbol{\mu}^T$, respectively, and which can drive the following

equations;

$$\langle \boldsymbol{D} \rangle = \boldsymbol{C}, \tag{C.14}$$

$$\langle \boldsymbol{D}_{,i} \rangle = 0, \tag{C.15}$$

$$\langle \boldsymbol{D}_{,ij} \rangle = \boldsymbol{\mu}_{,i}\boldsymbol{\mu}_{,j}^T + \boldsymbol{\mu}_{,j}\boldsymbol{\mu}_{,i}^T, \tag{C.16}$$

Taking the ensemble average of Eq. (C.12) leads $\langle \mathcal{L}_{,i} \rangle = 0$, and the likelihood function has a extremal value at the point where $\boldsymbol{\theta} = \boldsymbol{\Theta}$. Adopting the relation, $\mathrm{Tr}(\boldsymbol{AB}) = \mathrm{Tr}(\boldsymbol{BA})$, for Eq. (C.13) and taking the ensemble average, the Fisher information matrix can be rewritten as

$$\boldsymbol{F}_{ij} = \langle \mathcal{L}_{,ij} \rangle = \frac{1}{2}\mathrm{Tr}\left[\boldsymbol{C}^{-1}\boldsymbol{C}_{,i}\boldsymbol{C}^{-1}\boldsymbol{C}_{,j} + \boldsymbol{C}^{-1}\langle \boldsymbol{D}_{,ij} \rangle\right] . \tag{C.17}$$

On the other hand, when the expectation value $\langle \hat{\theta} \rangle$ of estimator $\hat{\theta}$ corresponds to the true value of parameters, $\hat{\theta}$ is called the unbiased estimator of parameter θ. The scatter of estimated parameter from this unbiased estimator has the minimum value, which is led from the Cramér-Rao's inequalityBy using the Cramér-Rao's inequality, the relationship between the Fisher information matrix and the scatter of each parameter is given by

$$\mathrm{var}(\hat{\theta})_{ij} = F_{ij}^{-1}(\theta). \tag{C.18}$$

C.2 Cramér-Rao Inequality

We here briefly summarize the Cramér-Rao inequality, which is adopted to put the minimum value on the scatter of estimated parameter from the unbiased estimator.

We introduce the random sample from $f(x;\theta)$ as $X_1, X_2, \cdots, X_n$ and define the joint probability density function as

$$L = \prod_{i=1}^{n} f(x_i)\,, \tag{C.19}$$

where θ is a scalar value. To simplify the expression, we describe the n-multiple integration as $\underbrace{\int \cdots \int}_{n} \to \int^{(n)}$, then Eq. (C.19) can be rewritten as

$$\int^{(n)} L\, dx_1 \cdots dx_n = 1\,. \tag{C.20}$$

By differentiating both sides with θ, we can get the following equation;

$$\int^{(n)} \frac{\partial L}{\partial \theta}\, dx_1 \cdots dx_n = 0\,. \tag{C.21}$$

Therefore the expectation value of $\dfrac{\partial \log L}{\partial \theta}$ can be given by

$$E\left(\frac{\partial \log L}{\partial \theta}\right) = \int^{(n)} \left(\frac{1}{L}\frac{\partial L}{\partial \theta}\right) L\, dx_1 \cdots dx_n = 0\,. \tag{C.22}$$

Furthermore, differentiating Eq. (C.22) with θ again leads to the following result

$$\int^{(n)} \left\{ \left(\frac{1}{L}\frac{\partial L}{\partial \theta}\right) \frac{\partial L}{\partial \theta} + L\frac{\partial}{\partial \theta}\left(\frac{1}{L}\frac{\partial L}{\partial \theta}\right) \right\} dx_1 \cdots dx_n = 0\,. \tag{C.23}$$

Then, by using the following equations;

$$\left(\frac{1}{L}\frac{\partial L}{\partial \theta}\right) \frac{\partial L}{\partial \theta} = \left(\frac{1}{L}\frac{\partial L}{\partial \theta}\right)^2 L = \left(\frac{\partial \log L}{\partial \theta}\right)^2 L\,, \tag{C.24}$$

and

$$\frac{\partial}{\partial \theta}\left(\frac{1}{L}\frac{\partial L}{\partial \theta}\right) = \frac{\partial}{\partial \theta}\left(\frac{\partial \log L}{\partial \theta}\right) = \frac{\partial^2 \log L}{\partial \theta^2}\,, \tag{C.25}$$

Eq. (C.23) cab be rewritten as

$$\int^{(n)} \left\{ \left(\frac{\partial \log L}{\partial \theta}\right)^2 + \left(\frac{\partial^2 \log L}{\partial \theta^2}\right) \right\} L\, dx_1, \cdots dx_n = 0\,. \tag{C.26}$$

More specifically, following equation can be obtained;

$$E\left[\left(\frac{\partial \log L}{\partial \theta}\right)^2\right] = -E\left(\frac{\partial^2 \log L}{\partial \theta^2}\right)\,. \tag{C.27}$$

We here define $\bar{\theta}$ as an arbitrary unbiased estimator of θ.

$$E(\bar{\theta}) = \int^{(n)} \bar{\theta}\, L\, dx_1 \cdots dx_n\,, \tag{C.28}$$

leads to

$$\int^{(n)} \bar{\theta}\, L\, dx_1 \cdots dx_n = \theta\,. \tag{C.29}$$

By differentiating both sides of above equation with θ, we obtain the following equation;

$$\int^{(n)} \bar{\theta} \left(\frac{\partial \log L}{\partial \theta}\right) L\, dx_1 \cdots dx_n = 1\,. \tag{C.30}$$

From Eq. (C.22),

$$\int^{(n)} \theta \left(\frac{\partial \log L}{\partial \theta}\right) L\, dx_1 \cdots dx_n = 0\,, \tag{C.31}$$

and combining above equation and Eq. (C.30) leads to the following result;

$$\int^{(n)} (\bar{\theta} - \theta) \left(\frac{\partial \log L}{\partial \theta} \right) L \, dx_1 \cdots dx_n = 1 \,. \tag{C.32}$$

We next introduce variables as follows;

$$g(x_1, \cdots, x_n) = g_n \,, \tag{C.33}$$

$$h(x_1, \cdots, x_n) = h_n \,, \tag{C.34}$$

then, the Cauchy-Schwarz inequality can be given by

$$\left[\int^{(n)} g_n \, h_n \, L \, dx_1 \cdots dx_n \right]^2 \leq \left[\int^{(n)} g_n^2 \, L \, dx_1 \cdots dx_n \right]^2 \left[\int^{(n)} h_n^2 \, L \, dx_1 \cdots dx_n \right]^2 . \tag{C.35}$$

When we adopt

$$g_n = \bar{\theta} - \theta \,, \tag{C.36}$$

$$h_n = \frac{\partial \log L}{\partial \theta} \,, \tag{C.37}$$

it leads following equations;

$$\int^{(n)} g_n^2 \, L \, dx_1 \cdots dx_n = E(\bar{\theta} - \theta)^2 = \mathrm{var}(\bar{\theta}) \,, \tag{C.38}$$

$$\int^{(n)} h_n^2 \, L \, dx_1 \cdots dx_n = E \left(\frac{\partial \log L}{\partial \theta} \right)^2 , \tag{C.39}$$

$$\int^{(n)} g_n \, h_n \, L \, dx_1 \cdots dx_n = \int^{(n)} (\bar{\theta} - \theta) \left(\frac{\partial \log L}{\partial \theta} \right) L \, dx_1 \cdots dx_n = 1 \,. \tag{C.40}$$

Inserting these equations into the Cauchy-Schwarz inequality, we get the following result;

$$1 \leq \mathrm{var}(\bar{\theta}) \, E \left(\frac{\partial \log L}{\partial \theta} \right)^2 . \tag{C.41}$$

As a result, we can obtain the following inequality;

$$\mathrm{var}(\bar{\theta}) \geq \frac{1}{E \left(\dfrac{\partial \log L}{\partial \theta} \right)^2} \,. \tag{C.42}$$

On the other hand, Eq. (C.42) can be rewritten with Eq. (C.27) as follow;

$$\mathrm{var}(\bar{\theta}) \geq - \frac{1}{E \left(\dfrac{\partial^2 \log L}{\partial \theta^2} \right)} \,. \tag{C.43}$$

Eq. (C.42) or Eq. (C.43) is called the Cramér-Rao inequality. The variance for the unbiased estimator of θ ($\bar{\theta}$) has boundary and the minimum variance can be given by

$$\frac{1}{E\left(\frac{\partial \log L}{\partial \theta}\right)^2} = -\frac{1}{E\left(\frac{\partial^2 \log L}{\partial \theta^2}\right)} . \tag{C.44}$$

Above minimum variance is called *Cramér-Rao bound*.

We introduce the following quantity;

$$S(\theta; x) = \frac{\partial \log L}{\partial \theta} , \tag{C.45}$$

which is called Score and Eq. (C.21) leads to

$$\begin{aligned} E(S) &= 0 , \\ \mathrm{var}(S) &= \text{Cramér} - \text{Rao bound} . \end{aligned}$$

The variance of the Cramér-Rao bound is often expressed by

$$E\left(\frac{\partial \log L}{\partial \theta}\right)^2 = -E\left(\frac{\partial^2 \log L}{\partial \theta^2}\right) = F(\theta) , \tag{C.46}$$

where $F(\theta)$ corresponds to the Fisher information matrix and $F(\theta)$ leads to the relation between an arbitrary unbiased estimator of θ ($(\tilde{\theta})$);

$$\mathrm{var}(\tilde{\theta}) \leq [F(\theta)]^{-1} . \tag{C.47}$$

When θ is the vector with k unknown parameters, not scholar,

$$\boldsymbol{\theta} = \begin{bmatrix} \theta_1 \\ \theta_2 \\ \vdots \\ \theta_k \end{bmatrix} , \tag{C.48}$$

we define the vector of an arbitrary unbiased estimator for θ and the covariance matrix as $\tilde{\boldsymbol{\theta}}$ and $\mathrm{var}(\tilde{\boldsymbol{\theta}})$, respectively. Then the Fisher information matrix can be given by

$$F(\boldsymbol{\theta}) = -E\left[\frac{\partial^2 \log L(\boldsymbol{\theta})}{\partial \theta \partial \theta'}\right] = -\begin{bmatrix} E\left(\frac{\partial^2 \log L(\theta)}{\partial \theta_1^2}\right) & \cdots & E\left(\frac{\partial^2 \log L(\theta)}{\partial \theta_1 \partial \theta_k}\right) \\ \vdots & & \vdots \\ E\left(\frac{\partial^2 \log L(\theta)}{\partial \theta_k \partial \theta_1}\right) & \cdots & E\left(\frac{\partial^2 \log L(\theta)}{\partial \theta_k^2}\right) \end{bmatrix} , \tag{C.49}$$

and the Cramér-Rao Inequality can be generalized for the vector as

$$\mathrm{var}(\tilde{\boldsymbol{\theta}}) - F(\boldsymbol{\theta})^{-1} \quad : \text{positive definite}\,. \tag{C.50}$$

C.3 Application for the CMB experiment

We here estimate the noise spectrum and derive the likelihood function and the Fisher information matrix for the the CMB observation, assuming to utilize the temperature anisotropies and the polarization data.

C.3.1 Beam pattern and Noise spectrum

We here estimate the noise for the CMB observation. We detect the light coming into multiple pixels as signals and the signal has finite extent in each pixel. Therefore the signal detected in the i-th pixel s_i is given with the beak pattern of the i-th detector B_i and the observed temperature fluctuations Θ as

$$s_i = \int d\hat{n}\Theta(\hat{n})B_i(\hat{n})\,. \tag{C.51}$$

In the same manner, the polarization component can also given with the same manner as the temperature fluctuations Θ. The beam pattern B_i reflect the specification of the detector and we here assume the Gaussian beam pattern;

$$B_i(\vec{x}) = \frac{1}{2\pi\sigma^2}\exp\left(-\frac{(\vec{x}-\vec{x}_i)^2}{2\sigma^2}\right). \tag{C.52}$$

This assumption is known as the good approximation for most of the CMB experiments. The Fourier transformation of this also has the Gaussian form and given by

$$\begin{aligned}\tilde{B}_i(\vec{l}) &= \frac{1}{2\pi\sigma^2}\int d^2x e^{-i\vec{l}\cdot\vec{x}}\exp\left(-\frac{x^2}{2\sigma^2}\right),\\ &= e^{-l^2\sigma^2/2}\,,\end{aligned} \tag{C.53}$$

where σ represents the angular resolution of the detector and this equation implies that the information in the smaller scales than the beam size is smoothed out and can not be observed. Under such assumption, $\tilde{B}$ is independent of the direction of $\vec{l}$ and. The angular resolution σ can be associated with the full width at half-maximum (FWHM), which corresponds to the double value of x making $B(\vec{x})$ half of the maximum value (Knox, 1995; Tegmark and Efstathiou, 1996);

$$\sigma \equiv \theta_{\mathrm{FWHM}}/\sqrt{8\ln 2} = 0.4245\ \theta_{\mathrm{FWHM}}\,, \tag{C.54}$$

where θ_{FWHM} represents the angular size corresponding to the FWHM.

Next, we here estimate the noise spectrum. The actually observed power spectrum $\hat{C}_l^{XY}$ contains the primary signal power spectrum C_l^{XY} and the homogeneously distributed noise spectrum

N_l^{XY}. Furthermore, if there are no correlations between the signal and the noise, the observed power spectrum is given by

$$\hat{C}_l^{XY} = e^{-l^2\theta^2_{\rm FWHM}/8\ln 2}(C_l^{XY} + N_l^{XY}) \,, \tag{C.55}$$

with

$$N_l^{XY}\delta_{ll'}\delta_{mm'} \equiv \langle n_{lm}^X n_{l'm'}^{Y\,*}\rangle e^{l^2\theta^2_{\rm FWHM}/8\ln 2} \,, \tag{C.56}$$

where X, Y are represent the label for the temperature anisotropies and the polarization components. If there are no correlations between the temperature anisotropies and polarization, the cross-correlation noise spectrum reads to be zero; $N_l^{XY} = 0$ $(X \neq Y)$.

In Eq. (C.55), $e^{l^2\theta^2_{\rm FWHM}/8\ln 2}$ represents the resolution of a detector, $\langle n_{lm}^X n_{l'm'}^{Y\,*}\rangle$ represents the sensitivity of a detector. The sensitivity of a detector σ_X is given with the homogeneous CMB temperature $T_{\rm CMB}$ by

$$\frac{\sigma_X}{T_{\rm CMB}} \equiv n^X \,. \tag{C.57}$$

Then the noise spectrum N_l^{XX} is given by

$$N_l^{XX}\delta_{ll'} \equiv \left(\frac{\sigma_X}{T_{\rm CMB}}\right)^2 e^{l^2\theta^2_{\rm FWHM}/8\ln 2} \,. \tag{C.58}$$

In addition, the observation is often performed with multi-frequency bands. In such a case, by combining the observed CMB maps in each frequency band, it can scale back the influence of noise contamination. The frequency band corresponds to a frequency of ν_i is called a channel, the total noise N_l after combining the noise at each channel $N_{l,\,i}$ can be given by

$$N_l^{-1} = \sum_i (N_{l,\,i})^{-1} = \sqrt{\sum_{i\leq j} \frac{2}{N_i N_j (1+\delta_{ij})}}. \tag{C.59}$$

C.3.2 Likelihood function and Fisher information matrix

We here define the likelihood function for the CMB observation and derive the Fisher information matrix, following Perotto et al. (2006). As a fundamental case, we consider only two components for the CMB data, such as the temperature anisotropies T and E-mode polarization E.

We first define the data vector $\boldsymbol{d}$ as

$$\boldsymbol{d} = \{a_{lm}^T,\ a_{lm}^E\} \,. \tag{C.60}$$

For Eq. (C.4), the average value is defined as $\mu = 0$ for the CMB observables, then the covariance

matrix can be given by

$$\boldsymbol{C}(\boldsymbol{\theta}) = \delta_{ll'} \left\langle \begin{pmatrix} a_{lm}^T \\ a_{lm}^E \end{pmatrix} \begin{pmatrix} a_{lm}^{T\,*} & a_{lm}^{E\,*} \end{pmatrix} \right\rangle = \begin{pmatrix} C_l^{TT} & C_l^{TE} \\ C_l^{TE} & C_l^{EE} \end{pmatrix} , \tag{C.61}$$

where $\boldsymbol{\theta}$ denotes the parameter vector.

In such a case that the likelihood function follows the Gaussian distribution, it is given by

$$L(\boldsymbol{d};\boldsymbol{\theta}) = \frac{1}{\sqrt{2\pi \mathrm{det} \boldsymbol{C}(\boldsymbol{\theta})}} \exp\left(-\frac{1}{2} \boldsymbol{d}^* \boldsymbol{C}(\boldsymbol{\theta})^{-1} \boldsymbol{d} \right) . \tag{C.62}$$

Following the definition in Eq. (C.17), its second term reads to be $\boldsymbol{D}_{,ij} = 0$ from the definition of the average value and only the first term remains. Then the Fisher information matrix can be given by

$$F_{ij} = \sum_{l_{\mathrm{min}}}^{l_{\mathrm{max}}} \frac{2l+1}{2} \mathrm{Tr} \left(\boldsymbol{C}_l^{-1} \frac{\partial \boldsymbol{C}_l}{\partial \theta_i} \boldsymbol{C}_l^{-1} \frac{\partial \boldsymbol{C}_l}{\partial \theta_j} \right) , \tag{C.63}$$

where $\boldsymbol{C}_l$ is the matrix consisting of power spectrum of each component C_l^{XY} and defined by

$$\boldsymbol{C}_l \equiv \begin{pmatrix} C_l^{TT} & C_l^{TE} \\ C_l^{TE} & C_l^{EE} \end{pmatrix} . \tag{C.64}$$

The information obtained from the observation is limited by the resolution of a detector and. Therefore the available value of maximum multipole ℓ_{max} is finite and it is reflected to the fact $\ell_{\mathrm{max}} \to \infty$ is not realized. On the other hand, the observed area is also finite. Although the ideal observation can get $2l+1$ modes for each ℓ, actually the number is proportional to the fraction of observable area f_{sky}. Then the Fisher information matrix can be approximately as

$$F_{ij} = \sum_{l_{\mathrm{min}}}^{l_{\mathrm{max}}} \frac{(2l+1) f_{\mathrm{sky}}}{2} \mathrm{Tr} \left(\boldsymbol{C}_l^{-1} \frac{\partial \boldsymbol{C}_l}{\partial \theta_i} \boldsymbol{C}_l^{-1} \frac{\partial \boldsymbol{C}_l}{\partial \theta_j} \right) . \tag{C.65}$$

References

Bagla, J. S., and A. Loeb (2009). ArXiv e-prints. *"The hyperfine transition of 3He+ as a probe of the intergalactic medium"*. [arXiv:0905.1698].

Balser, D. S., R. T. Rood, and T. M. Bania (2007). Science, **317**, 1171. *"Comment on "Deep Mixing of ^{3}He: Reconciling Big Bang and Stellar Nucleosynthesis""*.

Bardeen, J. M. (1980). Phys. Rev. D, **22**, 1882–1905. *"Gauge-invariant cosmological perturbations"*.

Barkana, R., and A. Loeb (2005). Mon. Not. R. Astron. Soc., **363**, L36–L40. *"Probing the epoch of early baryonic infall through 21-cm fluctuations"*. [arXiv:astro-ph/0502083].

Baumann, D., M. G. Jackson, P. Adshead, A. Amblard, A. Ashoorioon, *et al.* , *American Institute of Physics Conference Series*, **1141** 10–120. "Probing Inflation with CMB Polarization".

Bell, M. B. (2000). Astrophys. J, **531**, 820–825. *"The Search for Primordial ^{3}He Using the 8.665 GHZ Hyperfine Spin-Flip Transition of $^3He^+$"*.

Beltran, M. (2008). Phys.Rev., **D78**, 023530. *"Isocurvature, non-gaussianity and the curvaton model"*. [arXiv:0804.1097].

Bennett, C. L., D. Larson, J. L. Weiland, N. Jarosik, G. Hinshaw, *et al.* (2013). Astrophys. J. Supp., **208**, 20. *"Nine-year Wilkinson Microwave Anisotropy Probe (WMAP) Observations: Final Maps and Results"*. [arXiv:1212.5225].

Binney, J., and S. Tremaine (1987). *Galactic dynamics*.

Black, J. H. (1981). Mon. Not. R. Astron. Soc., **197**, 553–563. *"The physical state of primordial intergalactic clouds"*.

Bond, J. R., L. Kofman, and D. Pogosyan (1996). Nature, **380**, 603–606. *"How filaments of galaxies are woven into the cosmic web"*. [arXiv:astro-ph/9512141].

Brandenburg, A., and F. D. Steffen (2004). JCAP, **0408**, 008. *"Axino dark matter from thermal production"*. [hep-ph/0405158].

Bucher, M., K. Moodley, and N. Turok (2000). Phys. Rev. D, **62** 8, 083508. *"General primordial cosmic perturbation"*. [astro-ph/9904231].

Cen, R. (1992). Astrophys.J.Suppl., **78**, 341–364. *"A Hydrodynamic approach to cosmology - Methodology"*.

Cen, R., and J. P. Ostriker (1999). Astrophys. J, **514**, 1–6. *"Where Are the Baryons?"*. [arXiv:astro-ph/9806281].

Chang, T.-C., U.-L. Pen, K. Bandura, and J. B. Peterson (2010). ArXiv e-prints. *"Hydrogen 21-cm Intensity Mapping at redshift 0.8"*. [arXiv:1007.3709].

Chang, T.-C., U.-L. Pen, J. B. Peterson, and P. McDonald (2008). Physical Review Letters, **100** 9, 091303. *"Baryon Acoustic Oscillation Intensity Mapping of Dark Energy"*. [arXiv:0709.3672].

Choi, E., N. A. Bond, M. A. Strauss, A. L. Coil, M. Davis, *et al.* (2010). Mon. Not. R. Astron. Soc., **406**, 320–328. *"Tracing the filamentary structure of the galaxy distribution at z ˜ 0.8"*. [arXiv:1003.3239].

Chongchitnan, S., and J. Silk (2012). Mon. Not. R. Astron. Soc., **426**, L21–L25. *"The 21-cm radiation from minihaloes as a probe of small primordial non-Gaussianity"*. [arXiv:1205.6799].

Chuzhoy, L., and P. R. Shapiro (2006). Astrophys. J, **651**, 1–7. *"Ultraviolet Pumping of Hyperfine Transitions in the Light Elements, with Application to 21 cm Hydrogen and 92 cm Deuterium Lines from the Early Universe"*. [arXiv:astro-ph/0512206].

Cole, S., and N. Kaiser (1989). Mon. Not. R. Astron. Soc., **237**, 1127–1146. *"Biased clustering in the cold dark matter cosmogony"*.

Colless, M., G. Dalton, S. Maddox, W. Sutherland, P. Norberg, *et al.* (2001). Mon. Not. R. Astron. Soc., **328**, 1039–1063. *"The 2dF Galaxy Redshift Survey: spectra and redshifts"*. [arXiv:astro-ph/0106498].

Covi, L., H.-B. Kim, J. E. Kim, and L. Roszkowski (2001). JHEP, **0105**, 033. *"Axinos as dark matter"*. [hep-ph/0101009].

Covi, L., L. Roszkowski, and M. Small (2002). JHEP, **0207**, 023. *"Effects of squark processes on the axino CDM abundance"*. [hep-ph/0206119].

Davis, M., J. A. Newman, S. M. Faber, and A. C. Phillips , *Deep Fields* 241. "The DEEP2 Redshift Survey".

Deguchi, S., and W. D. Watson (1985). Astrophys. J, **290**, 578–586. *"Excitation of the hyperfine transitions of atomic hydrogen, deuterium, and ionized helium 3 by Lyman-alpha radiation"*.

Dijkstra, M., A. Lidz, J. R. Pritchard, L. J. Greenhill, D. A. Mitchell, *et al.* (2008). Mon. Not. R. Astron. Soc., **390**, 1430–1436. *"On the detectability of the hydrogen 3-cm fine-structure line from the epoch of reionization"*. [arXiv:0809.4279].

Dillon, J. S., A. Liu, C. L. Williams, J. N. Hewitt, M. Tegmark, *et al.* (2013). ArXiv e-prints. *"Overcoming real-world obstacles in 21 cm power spectrum estimation: A method demonstration and results from early Murchison Widefield Array data"*. [arXiv:1304.4229].

Djorgovski, S. G., D. A. Frail, S. R. Kulkarni, J. S. Bloom, S. C. Odewahn, *et al.* (2001). Astrophys. J, **562**, 654–663. *"The Afterglow and the Host Galaxy of the Dark Burst GRB 970828"*. [astro-ph/0107539].

Dodelson, S. (2003). *Modern Cosmology*. Academic Press, 2 edition.

Draine, B. T. (2011). *Physics of the Interstellar and Intergalactic Medium*.

Drinkwater, M. J., R. J. Jurek, and C. Blake (2010). Mon. Not. R. Astron. Soc., **401**, 1429–1452. *"The WiggleZ Dark Energy Survey: survey design and first data release"*. [arXiv:0911.4246].

Dunkley, J., E. Calabrese, J. Sievers, G. E. Addison, N. Battaglia, *et al.* (2013). JCAP, **7**, 25. *"The Atacama Cosmology Telescope: likelihood for small-scale CMB data"*. [arXiv:1301.0776].

Dvali, G., A. Gruzinov, and M. Zaldarriaga (2004). Phys. Rev. D, **69** 2, 023505. *"New mechanism for generating density perturbations from inflation"*. [arXiv:astro-ph/0303591].

Eggleton, P. P., D. S. P. Dearborn, and J. C. Lattanzio (2008). Astrophys. J, **677**, 581–592. *"Compulsory Deep Mixing of ^{3}He and CNO Isotopes in the Envelopes of Low-Mass Red Giants"*. [arXiv:0706.2710].

Erdoğdu, P., O. Lahav, S. Zaroubi, G. Efstathiou, S. Moody, *et al.* (2004). Mon. Not. R. Astron. Soc., **352**, 939–960. *"The 2dF Galaxy Redshift Survey: Wiener reconstruction of the cosmic web"*. [arXiv:astro-ph/0312546].

Ewen, H. I., and E. M. Purcell (1951). Nature, **168**, 356. *"Observation of a Line in the Galactic Radio Spectrum: Radiation from Galactic Hydrogen at 1,420 Mc./sec."*.

Fan, X., C. L. Carilli, and B. Keating (2006). Ann. Rev. Astron. Astrophys., **44**, 415–462. *"Observational Constraints on Cosmic Reionization"*. [astro-ph/0602375].

Field, G. B. (1958). Proceedings of the IRE, **46**, 240–250. *"Excitation of the Hydrogen 21-CM Line"*.

Field, G. B. (1959). Astrophys. J, **129**, 536. *"The Spin Temperature of Intergalactic Neutral Hydrogen."*.

Fisher, R. A. (1935). Annals Eugen., **6**, 391–398. *"The Fiducial Argument in Statistical Inference"*.

Freudling, W., L. Staveley-Smith, B. Catinella, R. Minchin, M. Calabretta, *et al.* (2011). Astrophys. J, **727**, 40. *"Deep 21 cm H I Observations at $z \simeq 0.1$: The Precursor to the Arecibo Ultra Deep Survey"*. [arXiv:1011.0877].

Fukugita, M., and M. Kawasaki (1994). Mon. Not. R. Astron. Soc., **269**, 563. *"Reionization during Hierarchical Clustering in a Universe Dominated by Cold Dark Matter"*. [arXiv:astro-ph/9309036].

Fukugita, M., and P. J. E. Peebles (2004). Astrophys. J, **616**, 643–668. *"The Cosmic Energy Inventory"*. [arXiv:astro-ph/0406095].

Furlanetto, S., and M. Furlanetto (2007b). Mon.Not.Roy.Astron.Soc., **379**, 130–134. *"Spin Exchange Rates in Proton-Hydrogen Collisions"*. [astro-ph/0702487].

Furlanetto, S., S. P. Oh, and F. Briggs (2006a). Phys.Rept., **433**, 181–301. *"Cosmology at Low Frequencies: The 21 cm Transition and the High-Redshift Universe"*. [astro-ph/0608032].

Furlanetto, S. R., and M. R. Furlanetto (2007a). Mon. Not. R. Astron. Soc., **374**, 547–555. *"Spin-exchange rates in electron-hydrogen collisions"*. [arXiv:astro-ph/0608067].

Furlanetto, S. R., and A. Loeb (2002). Astrophys. J, **579**, 1–9. *"The 21 Centimeter Forest: Radio Absorption Spectra as Probes of Minihalos before Reionization"*. [arXiv:astro-ph/0206308].

Furlanetto, S. R., S. P. Oh, and E. Pierpaoli (2006b). Phys.Rev., **D74**, 103502. *"The Effects of Dark Matter Decay and Annihilation on the High-Redshift 21 cm Background"*. [astro-ph/0608385].

Furlanetto, S. R., and J. R. Pritchard (2006). Mon. Not. R. Astron. Soc., **372**, 1093–1103. *"The scattering of Lyman-series photons in the intergalactic medium"*. [arXiv:astro-ph/0605680].

Goldwire, H. C., Jr., and W. M. Goss (1967). Astrophys. J, **149**, 15. *"Microwave Radiation of Singly Charged Helium 3 from H II Regions"*.

Gordon, C., and J. R. Pritchard (2009). Phys. Rev. D, **80** 6, 063535. *"Forecasted 21cm constraints on compensated isocurvature perturbations"*. [arXiv:0907.5400].

Gould, R. J. (1994). Astrophys. J, **423**, 522–528. *"Radiative hyperfine transitions"*.

Gunn, J. E., and J. R. Gott, III (1972). Astrophys. J, **176**, 1. *"On the Infall of Matter Into Clusters of Galaxies and Some Effects on Their Evolution"*.

Gunn, J. E., and B. A. Peterson (1965). Astrophys. J, **142**, 1633–1641. *"On the Density of Neutral Hydrogen in Intergalactic Space."*.

Haardt, F., and P. Madau (2012). Astrophys. J, **746**, 125. *"Radiative Transfer in a Clumpy Universe. IV. New Synthesis Models of the Cosmic UV/X-Ray Background"*. [arXiv:1105.2039].

Hey, J. S. (1946). Nature, **157**, 47–48. *"Solar Radiations in the 4-6 Metre Radio Wave-Length Band"*.

Hinshaw, G., D. Larson, E. Komatsu, D. N. Spergel, C. L. Bennett, *et al.* (2013). Astrophys. J. Supp., **208**, 19. *"Nine-year Wilkinson Microwave Anisotropy Probe (WMAP) Observations: Cosmological Parameter Results"*. [arXiv:1212.5226].

Hirata, C. M. (2006). Mon. Not. R. Astron. Soc., **367**, 259–274. *"Wouthuysen-Field coupling strength and application to high-redshift 21-cm radiation"*. [arXiv:astro-ph/0507102].

Hu, W., and T. Okamoto (2002). Astrophys. J, **574**, 566–574. *"Mass Reconstruction with Cosmic Microwave Background Polarization"*. [arXiv:astro-ph/0111606].

Ichikawa, K., T. Suyama, T. Takahashi, and M. Yamaguchi (2008a). Phys.Rev., **D78**, 023513. *"Non-Gaussianity, Spectral Index and Tensor Modes in Mixed Inflaton and Curvaton Models"*. [arXiv:0802.4138].

Ichikawa, K., T. Suyama, T. Takahashi, and M. Yamaguchi (2008b). Phys.Rev., **D78**, 063545. *"Primordial Curvature Fluctuation and Its Non-Gaussianity in Models with Modulated Reheating"*. [arXiv:0807.3988].

Iliev, I. T., and P. R. Shapiro (2001). Mon. Not. R. Astron. Soc., **325**, 468–482. *"The post-collapse equilibrium structure of cosmological haloes in a low-density universe"*. [arXiv:astro-ph/0101067].

Iliev, I. T., P. R. Shapiro, A. Ferrara, and H. Martel (2002). Astrophys. J. Lett., **572**, L123–L126. *"On the Direct Detectability of the Cosmic Dark Ages: 21 Centimeter Emission from Minihalos"*. [arXiv:astro-ph/0202410].

Kaiser, N. (1987). Mon. Not. R. Astron. Soc., **227**, 1–21. *"Clustering in real space and in redshift space"*.

Kasuya, S., and M. Kawasaki (2009). Phys. Rev. D, **80** 2, 023516. *"Axion isocurvature fluctuations with extremely blue spectrum"*. [arXiv:0904.3800].

Kawasaki, M., T. Sekiguchi, and T. Takahashi (2011). JCAP, **10**, 28. *"Differentiating CDM and baryon isocurvature models with 21 cm fluctuations"*. [arXiv:1104.5591].

Knox, L. (1995). Phys. Rev. D, **52**, 4307–4318. *"Determination of inflationary observables by cosmic microwave background anisotropy experiments"*. [arXiv:astro-ph/9504054].

Kodama, H., and M. Sasaki (1984). Progress of Theoretical Physics Supplement, **78**, 1. *"Cosmological Perturbation Theory"*.

Kofman, L. (2003). ArXiv Astrophysics e-prints. *"Probing String Theory with Modulated Cosmological Fluctuations"*. [astro-ph/0303614].

Komatsu, E., K. M. Smith, J. Dunkley, C. L. Bennett, B. Gold, *et al.* (2011). Astrophys. J. Supp., **192**, 18–+. *"Seven-year Wilkinson Microwave Anisotropy Probe (WMAP) Observations: Cosmological Interpretation"*. [arXiv:1001.4538].

Langlois, D., and F. Vernizzi (2004). Phys.Rev., **D70**, 063522. *"Mixed inflaton and curvaton perturbations"*. [astro-ph/0403258].

Langlois, D., F. Vernizzi, and D. Wands (2008). JCAP, **0812**, 004. *"Non-linear isocurvature perturbations and non-Gaussianities"*. [arXiv:0809.4646].

Lazarides, G., R. R. de Austri, and R. Trotta (2004). Phys.Rev., **D70**, 123527. *"Constraints on a mixed inflaton and curvaton scenario for the generation of the curvature perturbation"*. [hep-ph/0409335].

Lewis, A., and A. Challinor (2007). Phys. Rev. D, **76** 8, 083005. *"21cm angular-power spectrum from the dark ages"*. [arXiv:astro-ph/0702600].

Lewis, A., A. Challinor, and D. Hanson (2011). JCAP, **3**, 18. *"The shape of the CMB lensing bispectrum"*. [arXiv:1101.2234].

Lewis, A., A. Challinor, and A. Lasenby (2000). Astrophys. J, **538**, 473–476. *"Efficient Computation of Cosmic Microwave Background Anisotropies in Closed Friedmann-Robertson-Walker Models"*. [arXiv:astro-ph/9911177].

Lyth, D. H., C. Ungarelli, and D. Wands (2003). Phys.Rev., **D67**, 023503. *"The Primordial density perturbation in the curvaton scenario"*. [astro-ph/0208055].

Lyth, D. H., and D. Wands (2003). Phys.Rev., **D68**, 103515. *"Conserved cosmological perturbations"*. [astro-ph/0306498].

Madau, P., A. Meiksin, and M. J. Rees (1997). Astrophys. J, **475**, 429. *"21 Centimeter Tomography of the Intergalactic Medium at High Redshift"*. [arXiv:astro-ph/9608010].

Masui, K., E. Switzer, N. Banavar, K. Bandura, C. Blake, *et al.* (2012). arXiv:1208.0331. *"Measurement of 21 cm brightness fluctuations at z 0.8 in cross-correlation"*. [arXiv:1208.0331].

Matsuda, T., H. Sato, and H. Takeda (1971). Prog.Theor.Phys., **46**, 416–432. *"Dissipation of primordial turbulence and thermal history of the universe"*.

McQuinn, M., and E. R. Switzer (2009). Phys.Rev., **D80**, 063010. *"Redshifted intergalactic 3He+ 8.7 GHz hyperfine absorption"*. [arXiv:0905.1715].

Menzel, D. H., and C. L. Pekeris (1935). Mon. Not. R. Astron. Soc., **96**, 77. *"Absorption coefficients and hydrogen line intensities"*.

Mesinger, A., S. Furlanetto, and R. Cen (2011). Mon. Not. R. Astron. Soc., **411**, 955–972. *"21CMFAST: a fast, seminumerical simulation of the high-redshift 21-cm signal"*. [arXiv:1003.3878].

Mo, H., F. van den Bosch, and S. White (2010). *Galaxy Formation and Evolution*. Cambridge University Press, 1 edition.

Moroi, T., and T. Takahashi (2002). Phys.Rev., **D66**, 063501. *"Cosmic density perturbations from late decaying scalar condensations"*. [hep-ph/0206026].

Moroi, T., and T. Takahashi (2005). Phys.Rev., **D72**, 023505. *"Implications of the curvaton on inflationary cosmology"*. [astro-ph/0505339].

Moroi, T., and T. Takahashi (2009). Phys.Lett., **B671**, 339–344. *"Non-Gaussianity and Baryonic Isocurvature Fluctuations in the Curvaton Scenario"*. [arXiv:0810.0189].

Moroi, T., T. Takahashi, and Y. Toyoda (2005). Phys.Rev., **D72**, 023502. *"Relaxing constraints on inflation models with curvaton"*. [hep-ph/0501007].

Muller, C. A., and J. H. Oort (1951). Nature, **168**, 357–358. *"Observation of a Line in the Galactic Radio Spectrum: The Interstellar Hydrogen Line at 1,420 Mc./sec., and an Estimate of Galactic Rotation"*.

Nan, R., D. Li, C. Jin, Q. Wang, L. Zhu, *et al.* (2011). International Journal of Modern Physics D, **20**, 989–1024. *"The Five-Hundred Aperture Spherical Radio Telescope (fast) Project"*. [arXiv:1105.3794].

Nussbaumer, H., and P. J. Storey (1983). Astron. & Astrophys., **126**, 75–79. *"Dielectronic recombination at low temperatures"*.

Oh, S. P., and K. J. Mack (2003). Mon. Not. R. Astron. Soc., **346**, 871–877. *"Foregrounds for 21-cm observations of neutral gas at high redshift"*. [arXiv:astro-ph/0302099].

Okamoto, T., and W. Hu (2003). Phys. Rev. D, **67** 8, 083002–+. *"Cosmic microwave background lensing reconstruction on the full sky"*. [arXiv:astro-ph/0301031].

Olive, K. A., R. T. Rood, D. N. Schramm, J. W. Truran, and E. Vangioni-Flam (1995). Astrophys.J., **444**, 680–685. *"What's the problem with He-3?"*. [astro-ph/9410058].

Osterbrock, D. E. (1989). *Astrophysics of gaseous nebulae and active galactic nuclei.*

Paciga, G., J. G. Albert, K. Bandura, T.-C. Chang, Y. Gupta, *et al.* (2013). Mon. Not. R. Astron. Soc., **433**, 639–647. *"A simulation-calibrated limit on the H I power spectrum from the GMRT Epoch of Reionization experiment"*. [arXiv:1301.5906].

Padmanabhan, T. (1993). *Structure Formation in the Universe.*

Pandey, B., G. Kulkarni, S. Bharadwaj, and T. Souradeep (2011). Mon. Not. R. Astron. Soc., **411**, 332–336. *"The size of the longest filament in the luminous red galaxy distribution"*. [arXiv:1009.2223].

Parsons, A. R., A. Liu, J. E. Aguirre, Z. S. Ali, R. F. Bradley, *et al.* (2013). ArXiv e-prints. *"New Limits on 21cm EoR From PAPER-32 Consistent with an X-Ray Heated IGM at z=7.7"*. [arXiv:1304.4991].

Pawsey, J. L. (1951). Nature, **168**, 358. *"Observation of a Line in the Galactic Radio Spectrum: The Interstellar Hydrogen Line at 1,420 Mc./sec., and an Estimate of Galactic Rotation"*.

Perotto, L., J. Lesgourgues, S. Hannestad, H. Tu, and Y. Y Y Wong (2006). JCAP, **10**, 13. *"Probing cosmological parameters with the CMB: forecasts from Monte Carlo simulations"*. [arXiv:astro-ph/0606227].

Planck Collaboration, P. A. R. Ade, N. Aghanim, C. Armitage-Caplan, M. Arnaud, *et al.* (2013a). ArXiv e-prints. *"Planck 2013 results. I. Overview of products and scientific results"*. [arXiv:1303.5062].

Planck Collaboration, P. A. R. Ade, N. Aghanim, C. Armitage-Caplan, M. Arnaud, *et al.* (2013b). ArXiv e-prints. *"Planck 2013 results. XVI. Cosmological parameters"*. [arXiv:1303.5076].

Planck Collaboration, P. A. R. Ade, N. Aghanim, C. Armitage-Caplan, M. Arnaud, *et al.* (2013c). ArXiv e-prints. *"Planck 2013 results. XXII. Constraints on inflation"*. [arXiv:1303.5082].

Popping, A., and R. Braun (2011). Astron. & Astrophys., **527**, A90. *"The WSRT Virgo H i filament survey. I. Total power data"*. [arXiv:1012.3236].

Popping, A., R. Davé, R. Braun, and B. D. Oppenheimer (2009). Astron. & Astrophys., **504**, 15–32. *"The simulated H I sky at low redshift"*. [arXiv:0906.3067].

Press, W. H., and P. Schechter (1974). Astrophys. J, **187**, 425–438. *"Formation of Galaxies and Clusters of Galaxies by Self-Similar Gravitational Condensation"*.

Pritchard, J. R., and S. R. Furlanetto (2006). Mon. Not. R. Astron. Soc., **367**, 1057–1066. *"Descending from on high: Lyman-series cascades and spin-kinetic temperature coupling in the 21-cm line"*. [arXiv:astro-ph/0508381].

Pritchard, J. R., and A. Loeb (2012). Reports on Progress in Physics, **75** 8, 086901. *"21 cm cosmology in the 21st century"*. [arXiv:1109.6012].

Rajagopal, K., M. S. Turner, and F. Wilczek (1991). Nucl.Phys., **B358**, 447–470. *"Cosmological implications of axinos"*.

Robertson, B. E., S. R. Furlanetto, E. Schneider, S. Charlot, R. S. Ellis, *et al.* (2013). Astrophys. J, **768**, 71. *"New Constraints on Cosmic Reionization from the 2012 Hubble Ultra Deep Field Campaign"*. [arXiv:1301.1228].

Rood, R. T., T. M. Bania, D. S. Balser, and T. L. Wilson (1998). Space Science Reviews , **84**, 185–198. *"Helium-3: Status and Prospects"*.

Rood, R. T., T. L. Wilson, and G. Steigman (1979). Astrophys. J. Lett., **227**, L97–L101. *"The probable detection of interstellar He-3/+/ and its significance"*.

Rybicki, G. B., and A. P. Lightman (1986). *Radiative Processes in Astrophysics*.

Seager, S., D. D. Sasselov, and D. Scott (1999). Astrophys.J., **523**, L1–L5. *"A new calculation of the recombination epoch"*. [astro-ph/9909275].

Seager, S., D. D. Sasselov, and D. Scott (2000). Astrophys.J.Suppl., **128**, 407–430. *"How exactly did the universe become neutral?"*. [astro-ph/9912182].

Sekiguchi, T., H. Tashiro, J. Silk, and N. Sugiyama (2013). ArXiv e-prints. *"Cosmological signatures of tilted isocurvature perturbations: reionization and 21cm fluctuations"*. [arXiv:1311.3294].

Shapiro, P. R., I. T. Iliev, and A. C. Raga (1999). Mon. Not. R. Astron. Soc., **307**, 203–224. *"A model for the post-collapse equilibrium of cosmological structure: truncated isothermal spheres from top-hat density perturbations"*. [arXiv:astro-ph/9810164].

Shaver, P. A. (1975). Astron. & Astrophys., **43**, 465–468. *"Characteristics of the interstellar medium as deduced from low-frequency recombination line observations"*.

Shaver, P. A., R. A. Windhorst, P. Madau, and A. G. de Bruyn (1999). Astron. & Astrophys., **345**, 380–390. *"Can the reionization epoch be detected as a global signature in the cosmic background?"*. [arXiv:astro-ph/9901320].

Shchekinov, Y. A., and E. Vasiliev (2007). Mon.Not.Roy.Astron.Soc., **379**, 1003–1010. *"Particle decay in the early universe: predictions for 21 cm"*. [astro-ph/0604231].

Sheth, R. K., H. J. Mo, and G. Tormen (2001). Mon. Not. R. Astron. Soc., **323**, 1–12. *"Ellipsoidal collapse and an improved model for the number and spatial distribution of dark matter haloes"*. [arXiv:astro-ph/9907024].

Sheth, R. K., and G. Tormen (1999). Mon. Not. R. Astron. Soc., **308**, 119–126. *"Large-scale bias and the peak background split"*. [arXiv:astro-ph/9901122].

Sigurdson, K., and S. R. Furlanetto (2006). Physical Review Letters, **97** 9, 091301. *"Measuring the Primordial Deuterium Abundance during the Cosmic Dark Ages"*. [arXiv:astro-ph/0505173].

Skrutskie, M. F., R. M. Cutri, R. Stiening, M. D. Weinberg, S. Schneider, *et al.* (2006). Astron. J., **131**, 1163–1183. *"The Two Micron All Sky Survey (2MASS)"*.

Smoot, G. F., C. L. Bennett, A. Kogut, E. L. Wright, J. Aymon, *et al.* (1992). Astrophys. J. Lett., **396**, L1–L5. *"Structure in the COBE differential microwave radiometer first-year maps"*.

Spergel, D. N., L. Verde, H. V. Peiris, E. Komatsu, M. R. Nolta, *et al.* (2003). Astrophys. J. Supp., **148**, 175–194. *"First-Year Wilkinson Microwave Anisotropy Probe (WMAP) Observations: Determination of Cosmological Parameters"*. [arXiv:astro-ph/0302209].

Spitzer, L. (1978). *Physical Processes In The Interstellar Medium*. Wiley classics library. Wiley & Son.

Spitzer, L. (1998). *Physical Processes in the Interstellar Medium.*

Springel, V. (2005). Mon. Not. R. Astron. Soc., **364**, 1105–1134. *"The cosmological simulation code GADGET-2"*. [arXiv:astro-ph/0505010].

Sunyaev, R. A. (1966). Astronomicheskii Zhurnal, **43**, 1237. *"Sources of Helium 3 and Possibilities for Observing It."*.

Switzer, E. R., K. W. Masui, K. Bandura, L.-M. Calin, T.-C. Chang, *et al.* (2013). ArXiv e-prints. *"Determination of z˜0.8 neutral hydrogen fluctuations using the 21 cm intensity mapping auto-correlation"*. [arXiv:1304.3712].

Syunyaev, R. A. (1966). Astronomicheskii Zhurnal, **43**, 1237. *"Sources of Helium 3 and Possibilities for Observing It."*.

Syunyaev, R. A., and E. M. Churazov (1984). Soviet Astronomy Letters, **10**, 201–205. *"Millimeter Wavelength Lines of Heavy Elements Predicted from the Hot Gas in Supernova Remnants and Galaxy Clusters"*.

Takahashi, T., M. Yamaguchi, J. Yokoyama, and S. Yokoyama (2009). Phys.Lett., **B678**, 15–19. *"Gravitino Dark Matter and Non-Gaussianity"*. [arXiv:0905.0240].

Takahashi, T., M. Yamaguchi, and S. Yokoyama (2009). Phys. Rev. D, **80** 6, 063524. *"Primordial non-Gaussianity in models with dark matter isocurvature fluctuations"*. [arXiv:0907.3052].

Takeuchi, Y., and S. Chongchitnan (2014). Mon. Not. R. Astron. Soc., , Advance Access. 11 pp. *"Constraining isocurvature perturbations with the 21 cm emission from minihaloes"*. [arXiv:1311.2585].

Takeuchi, Y., S. Zaroubi, and N. Sugiyama (2014). submitted to Mon. Not. R. Astron. Soc.. *"Probing large scale filaments wit H* I *and* ^{3}*He* II*"*.

Tashiro, H., T. Sekiguchi, and J. Silk (2013). ArXiv e-prints. *"High redshift signatures in the 21 cm forest due to cosmic string wakes"*. [arXiv:1310.4176].

Tegmark, M., and G. Efstathiou (1996). Mon. Not. R. Astron. Soc., **281**, 1297–1314. *"A method for subtracting foregrounds from multifrequency CMB sky maps**"*. [astro-ph/9507009].

Tegmark, M., A. N. Taylor, and A. F. Heavens (1997). Astrophys. J, **480**, 22–+. *"Karhunen-Loeve Eigenvalue Problems in Cosmology: How Should We Tackle Large Data Sets?"*. [arXiv:astro-ph/9603021].

Tegmark, M., and M. Zaldarriaga (2009). Phys. Rev. D, **79** 8, 083530. *"Fast Fourier transform telescope"*. [arXiv:0805.4414].

Tinker, J., A. V. Kravtsov, A. Klypin, K. Abazajian, M. Warren, *et al.* (2008). Astrophys. J, **688**, 709–728. *"Toward a Halo Mass Function for Precision Cosmology: The Limits of Universality"*. [arXiv:0803.2706].

Townes, C. H. , *Radio astronomy*, **4** 92. "Microwave and radio-frequency resonance lines of interest to radio astronomy".

Tseliakhovich, D., R. Barkana, and C. M. Hirata (2011). Mon. Not. R. Astron. Soc., **418**, 906–915. *"Suppression and spatial variation of early galaxies and minihaloes"*. [arXiv:1012.2574].

van de Hulst, H. (1945). Nederlands Tijdschrift voor Natuuurkunde, **11**, 210–221. *""*. [Radio Waves from Space: Origin of Radiowaves].

van Haarlem, M. P., M. W. Wise, Gunst, and et al. (2013a). Astron. & Astrophys., **556**, A2. *"LOFAR: The LOw-Frequency ARray"*. [arXiv:1305.3550].

van Haarlem, M. P., M. W. Wise, A. W. Gunst, G. Heald, J. P. McKean, *et al.* (2013b). Astron. & Astrophys., **556**, A2. *"LOFAR: The LOw-Frequency ARray"*. [arXiv:1305.3550].

Verner, D. A., and G. J. Ferland (1996). Astrophys. J. Supp., **103**, 467. *"Atomic Data for Astrophysics. I. Radiative Recombination Rates for H-like, He-like, Li-like, and Na-like Ions over a Broad Range of Temperature"*. [arXiv:astro-ph/9509083].

Warren, M. S., K. Abazajian, D. E. Holz, and L. Teodoro (2006). Astrophys. J, **646**, 881–885. *"Precision Determination of the Mass Function of Dark Matter Halos"*. [arXiv:astro-ph/0506395].

Weinberg, S. (2008). *Cosmology*. Oxford Univ Pr (Txt).

Wilson, R. W., and A. A. Penzias (1967). Science, **156**, 1100–1101. *"Isotropy of Cosmic Background Radiation at 4080 Megahertz"*.

Wouthuysen, S. A. (1952). Astron. J., **57**, 31–32. *"On the excitation mechanism of the 21-cm (radio-frequency) interstellar hydrogen emission line."*.

York, D. G., J. Adelman, J. E. Anderson, Jr., and SDSS Collaboration (2000). Astron. J., **120**, 1579–1587. *"The Sloan Digital Sky Survey: Technical Summary"*. [arXiv:astro-ph/0006396].

Zahn, O., C. L. Reichardt, L. Shaw, A. Lidz, K. A. Aird, *et al.* (2012). Astrophys. J, **756**, 65. *"Cosmic Microwave Background Constraints on the Duration and Timing of Reionization from the South Pole Telescope"*. [arXiv:1111.6386].

Zaroubi, S. , *Astrophysics and Space Science Library*, **396** 45. "The Epoch of Reionization".

Zygelman, B. (2005). Astrophys. J, **622**, 1356–1362. *"Hyperfine Level-changing Collisions of Hydrogen Atoms and Tomography of the Dark Age Universe"*.